Cell

A generative deep learning approach to *de novo* antibiotic design

Graphical abstract

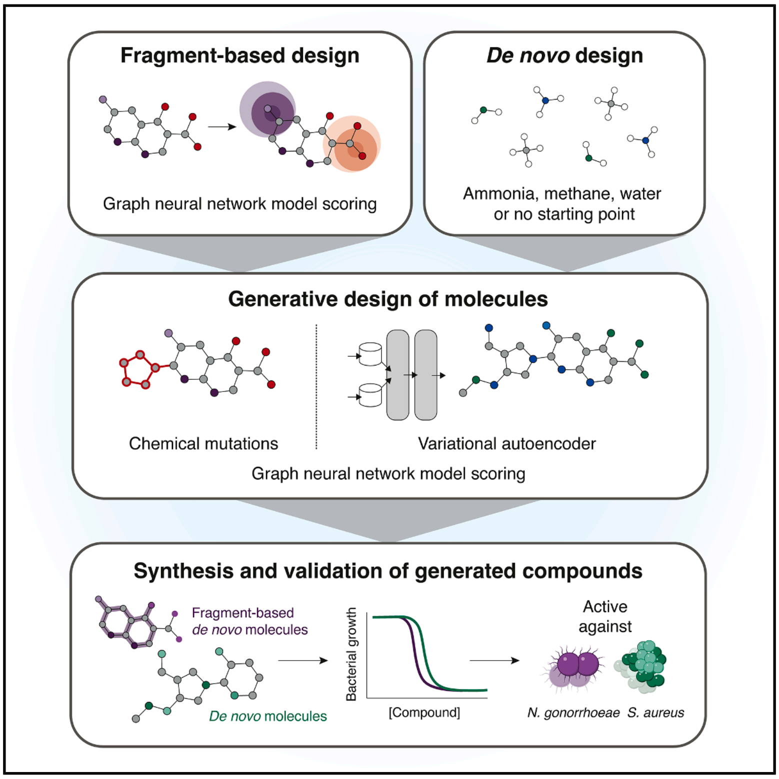

Highlights

- Genetic algorithms and variational autoencoders enable fragment-based and *de novo* design
- Seven of 24 custom-synthesized compounds show selective antibacterial activity
- Two lead compounds display unique modes of action against *N. gonorrhoeae* and *S. aureus*
- Two lead compounds show efficacy against multidrug-resistant strains and in mouse models

Authors

Aarti Krishnan, Melis N. Anahtar, Jacqueline A. Valeri, ..., Connor W. Coley, Felix Wong, James J. Collins

Correspondence

jimjc@mit.edu

In brief

A generative AI platform is developed for *de novo* antibiotic design, yielding lead compounds with selective antibacterial activity, distinct mechanisms of action, and *in vivo* efficacy against multidrug-resistant *N. gonorrhoeae* and *S. aureus*.

Krishnan et al., 2025, Cell *188*, 1–18
October 16, 2025
https://doi.org/10.1016/j.cell.2025.07.033

CellPress

Please cite this article in press as: Krishnan et al., A generative deep learning approach to *de novo* antibiotic design, Cell (2025), https://doi.org/10.1016/j.cell.2025.07.033

Cell

CellPress

Article

A generative deep learning approach to *de novo* antibiotic design

Aarti Krishnan,[1,2,3,4,25] **Melis N. Anahtar,**[1,2,4,5,25] **Jacqueline A. Valeri,**[1,2,4,25] **Wengong Jin,**[6,7] **Nina M. Donghia,**[4] **Leif Sieben,**[1,2,4,8] **Andreas Luttens,**[1,2] **Yu Zhang,**[1,2,4] **Seyed Majed Modaresi,**[1,2,4] **Andrew Hennes,**[1,4] **Jenna Fromer,**[9] **Parijat Bandyopadhyay,**[1,2] **Jonathan C. Chen,**[1,2] **Danyal Rehman,**[10] **Ronak Desai,**[1,11,12] **Paige Edwards,**[1,2] **Ryan S. Lach,**[13] **Marie-Stéphanie Aschtgen,**[14] **Margaux Gaborieau,**[14] **Massimiliano Gaetani,**[15,16] **Samantha G. Palace,**[17] **Satotaka Omori,**[13] **Lutete Khonde,**[18] **Yurii S. Moroz,**[19,20,21] **Bruce Blough,**[22] **Chunyang Jin,**[22] **Edmund Loh,**[14,23] **Yonatan H. Grad,**[17] **Amir Ata Saei,**[14] **Connor W. Coley,**[9,24] **Felix Wong,**[1,2,13] **and James J. Collins**[1,2,4,26,*]

[1]Infectious Disease and Microbiome Program, Broad Institute of MIT and Harvard, Cambridge, MA 02142, USA
[2]Institute for Medical Engineering & Science and Department of Biological Engineering, Massachusetts Institute of Technology, Cambridge, MA 02139, USA
[3]Whitehead Institute for Biomedical Research, Cambridge, MA 02142, USA
[4]Wyss Institute for Biologically Inspired Engineering, Harvard University, Boston, MA 02115, USA
[5]Departments of Pathology and Medicine, Massachusetts General Hospital, Boston, MA 02114, USA
[6]Eric and Wendy Schmidt Center, Broad Institute of MIT and Harvard, Cambridge, MA 02142, USA
[7]Khoury College of Computer Sciences, Northeastern University, Boston, MA 02115, USA
[8]Department of Chemistry and Applied Biosciences, ETH Zürich, 8093 Zürich, Switzerland
[9]Department of Chemical Engineering, Massachusetts Institute of Technology, Cambridge, MA 02139, USA
[10]Mila-Quebec AI Institute, Montréal, QC H2S 3H1, Canada
[11]Department of Chemistry, Massachusetts Institute of Technology, Cambridge, MA 02139, USA
[12]Harvard Medical School, Boston, MA 02115, USA
[13]Integrated Biosciences, Inc., Redwood City, CA 94065, USA
[14]Department of Microbiology, Tumor and Cell Biology, Karolinska Institute, 171 77 Stockholm, Sweden
[15]Division of Chemistry I, Department of Medical Biochemistry and Biophysics, Karolinska Institute, 17 177 Stockholm, Sweden
[16]Chemical Proteomics Unit, Science for Life Laboratory (SciLifeLab), 171 77Stockholm, Sweden
[17]Department of Immunology and Infectious Diseases, Harvard T. H. Chan School of Public Health, Boston, MA 02115, USA
[18]Center for the Development of Therapeutics, Broad Institute of MIT and Harvard, Cambridge, MA 02142, USA
[19]Enamine Ltd., 67 Winston Churchill Street, Kyiv 02094, Ukraine
[20]Chemspace LLC, 85 Winston Churchill Street, Kyiv 02094, Ukraine
[21]Department of Chemistry, Taras Shevchenko National University of Kyiv, 60 Volodymyrska Street, Kyiv 01601, Ukraine
[22]Center for Drug Discovery, RTI International, Research Triangle Park, Durham, NC 27713, USA
[23]Clinical Microbiology, Karolinska University Hospital, 171 76 Stockholm, Sweden
[24]Department of Electrical Engineering and Computer Science, Massachusetts Institute of Technology, Cambridge, MA 02139, USA
[25]These authors contributed equally
[26]Lead contact
*Correspondence: jimjc@mit.edu

https://doi.org/10.1016/j.cell.2025.07.033

SUMMARY

The antimicrobial resistance crisis necessitates structurally distinct antibiotics. While deep learning approaches can identify antibacterial compounds from existing libraries, structural novelty remains limited. Here, we developed a generative artificial intelligence framework for designing *de novo* antibiotics through two approaches: a fragment-based method to comprehensively screen $>10^7$ chemical fragments *in silico* against *Neisseria gonorrhoeae* or *Staphylococcus aureus*, subsequently expanding promising fragments, and an unconstrained *de novo* compound generation, each using genetic algorithms and variational autoencoders. Of 24 synthesized compounds, seven demonstrated selective antibacterial activity. Two lead compounds exhibited bactericidal efficacy against multidrug-resistant isolates with distinct mechanisms of action and reduced bacterial burden *in vivo* in mouse models of *N. gonorrhoeae* vaginal infection and methicillin-resistant *S. aureus* skin infection. We further validated structural analogs for both compound classes as antibacterial. Our approach enables the generative deep-learning-guided design of *de novo* antibiotics, providing a platform for mapping uncharted regions of chemical space.

Please cite this article in press as: Krishnan et al., A generative deep learning approach to *de novo* antibiotic design, Cell (2025), https://doi.org/10.1016/j.cell.2025.07.033

INTRODUCTION

Antibiotic-resistant bacterial infections underlie an urgent public health crisis and are associated with approximately five million annual deaths globally.[1] Bacterial pathogens such as *Neisseria gonorrhoeae* and *Staphylococcus aureus* are categorized as "urgent" and "serious" threats, respectively, by the U.S. Centers for Disease Control and Prevention (CDC) due to the widespread incidence of resistance to existing antibiotics and dearth of new, effective antibiotic treatments.[2] Between 1980 and 2003, only five antibacterial agents were developed by the top 15 pharmaceutical companies.[3] There is a dire and growing need for structurally novel compounds, especially those with unique mechanisms of action, to overcome antibiotic-resistant infections.

Given the extensive time and resources needed for antibiotic discovery, computational approaches to facilitate the identification of new candidates have emerged. Recently, deep learning approaches have been used to screen millions of compounds *in silico* for activity against diverse pathogens.[4–10] A graph neural network (GNN), for example, is a type of deep learning model that has successfully been used to predict antibacterial activity. GNNs represent chemical structures as mathematical graphs and iteratively update graph node and edge values using "message passing" operations.[11] Ultimately, for a given molecule, a GNN produces a single output value between 0 and 1, representing the predicted probability that the molecule possesses a specific property of interest (e.g., antibacterial activity or cytotoxicity).

Although deep learning approaches have substantially increased discovery rates[4–8] and facilitated the discovery of a new structural class of antibiotics,[7] they have largely been applied to existing *in silico* small molecule libraries, limiting the structural diversity that can be explored. Drug-like chemical space has been theoretically estimated to contain $\sim10^{60}$ compounds,[12] but the largest *in silico* libraries currently contain only $\sim10^{11}$ compounds.[13,14] Generative artificial intelligence (AI) approaches can expand beyond these known chemical spaces[15–22] and have recently been applied to both antimicrobial peptide design[23–25] and to the design and optimization of small molecules.[26–31] A recent study explored a large chemical space using a Monte Carlo tree search coupled to a GNN and found compounds with antibacterial activity against *Acinetobacter baumannii* when used in the presence of an outer membrane permeabilizerwhen used in the presence of an outer membrane permeabilizer.[32] Developing and experimentally validating generative AI methods that can design structurally novel antibacterial molecules, beyond those enumerated in commercial chemical spaces, would substantially augment the capability to search chemical space for antibiotic candidates.

In recent years, fragment-based drug discovery (FBDD) has emerged as a powerful tool for drug design, offering an efficient framework to screen large fragment libraries against a specific protein target.[33–36] By contrast, target-agnostic approaches prioritize phenotypic measurements from the start. By screening against whole-cell activity rather than specific molecular targets, phenotypic approaches can integrate useful structural information across diverse chemotypes, can yield molecules with diverse mechanisms of action, and could reduce the downstream attrition rates commonly associated with target-centric methods.[37] Despite their potential, phenotypic-guided approaches to both fragment-based and *de novo* molecule generation remain underexplored, representing a significant opportunity to develop novel chemical entities informed by biological outcomes rather than predefined structural constraints.

Here, we present a deep learning-based approach to the generative design of antibiotic compounds using fragments as starting points or generating these compounds *de novo*. In our fragment-based approach, we used GNNs to comprehensively screen >45 million chemical fragments *in silico* and identified fragments predicted to have selective antibacterial activity against *N. gonorrhoeae* and *S. aureus*. To expand the fragments into molecules, we provided them as inputs to two types of generative algorithms—a genetic algorithm based on chemically reasonable mutations (CReM) and a variational autoencoder (VAE). In our *de novo* approach, we removed the need for a fragment input and allowed the CReM and VAE models to design molecules based on knowledge learned during training. Together, these models generated >36 million previously unenumerated compounds with predicted antibacterial activity. After down selection, we synthesized 24 compounds and empirically validated 7 compounds to be antibacterial. Two of these compounds, **NG1** and **DN1**, displayed high potency and selectivity, with mechanisms of action distinct from those of clinically used antibiotics and efficacy in mouse models of infection. Our approach provides a platform for the generative deep-learning-guided design of antibiotic candidates, facilitating the discovery of antibacterial compounds and enabling the efficient exploration of vast, uncharted regions of chemical space.

RESULTS

Applying GNN models to large fragment spaces

As chemical fragments underlie the biological activity of structural classes of compounds and graph search algorithms can accurately identify substructures associated with selective antibacterial molecules,[7,12] we reasoned that fragments offer starting points for designing structurally unique antibacterial molecules using generative models. We found that the antibacterial prediction scores of commonly used antibiotics in three major classes are indeed associated with the prediction scores of their corresponding fragments (STAR Methods; Figure S1A). Accordingly, we comprehensively screened large, enumerated chemical fragment spaces using Chemprop models[11] based on GNNs that predict the antibacterial activity of a given fragment or molecule against *N. gonorrhoeae* or *S. aureus* (Figure 1A). These models were previously trained and benchmarked on empirical, binarized growth inhibition data for 38,765 compounds screened against *N. gonorrhoeae* American Type Culture Collection (ATCC) 49226 and 39,312 compounds screened against *S. aureus* RN4220, a methicillin-susceptible strain, at a final concentration of 50 μM[7,8] (Table S1). To further assess our models' predictive capabilities, we performed additional analyses and observed that the prediction scores for *N. gonorrhoeae* and *S. aureus* (1) significantly differed between compounds that were experimentally active and inactive (Figure S1B), (2) were influenced by

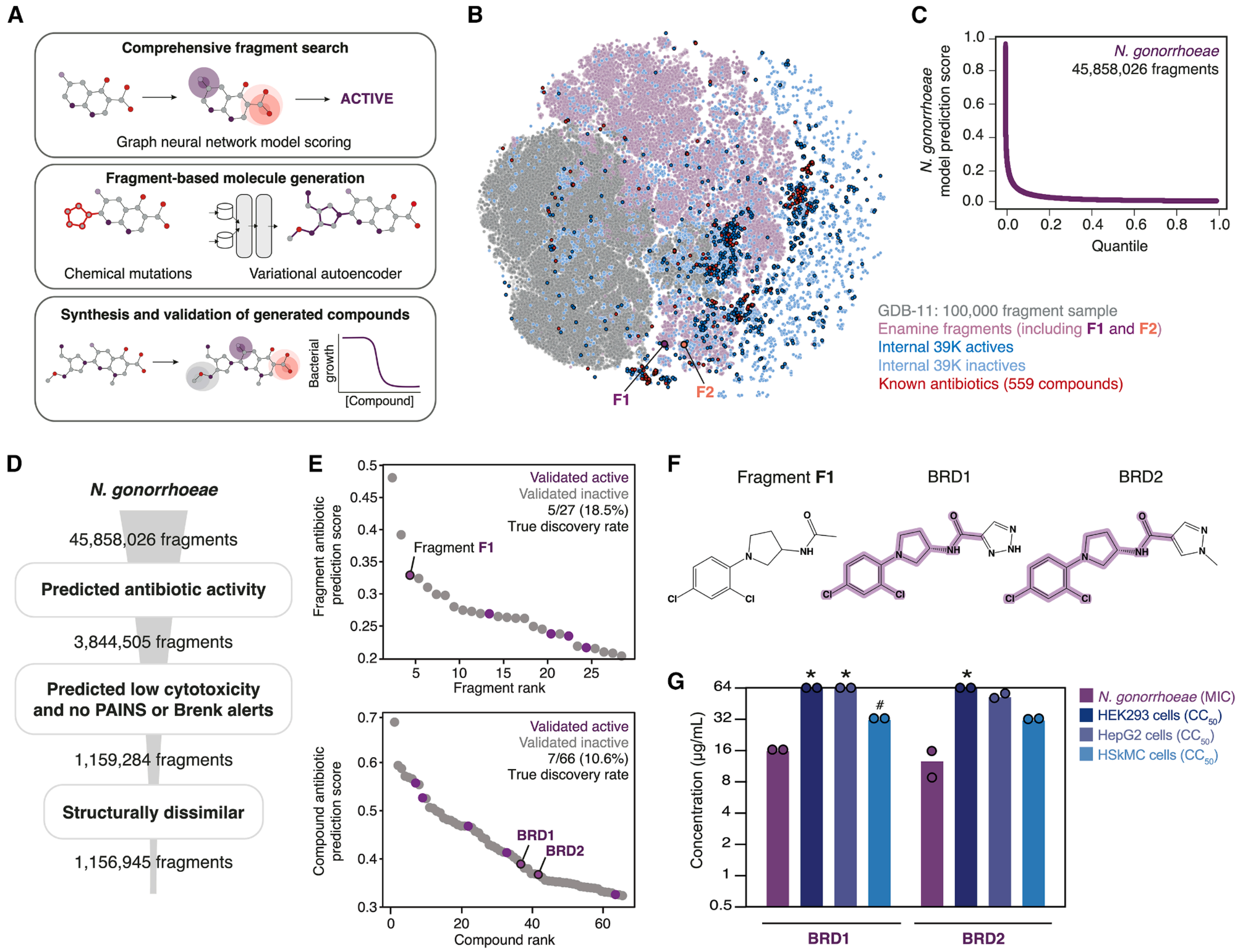

Figure 1. GNNs predict chemical fragments and compounds with antibacterial activity against *N. gonorrhoeae*

(A) Schematic of the fragment-based generation approach.

(B) t-SNE representation of chemical space, showing that fragment libraries represent chemical space diverse from known antibiotics.

(C) Rank-ordered fragment prediction scores from the *N. gonorrhoeae* antibacterial activity model.

(D) Computational filters applied to sets of fragments, resulting in final sets of fragments for *N. gonorrhoeae*.

(E) Rank-ordered plot of fragment (above) and compound (below) prediction scores for available compounds procured for empirical testing at 50 μM.

(F) Chemical structures of fragment F1 and associated active compounds from (E). The fragment is highlighted in the compounds.

(G) MIC and CC_{50} values for the compounds in (F). $n = 2$, * indicates values >64 μg/mL, and # indicates values >32 μg/mL.

See also Figure S1.

certain functional groups (Figure S1C), and (3) demonstrated species specificity (Figure S1D). These analyses indicated that our models could reliably identify antibacterial compounds and fragments as starting points for generative AI algorithms. To avoid selecting human cytotoxic compounds, we counter-screened fragments using human cytotoxicity models for hepatocellular carcinoma (HepG2), human skeletal muscle cells (HSkMCs), and human lung fibroblasts (IMR-90) that we had previously trained and benchmarked (Table S1).[7]

To comprehensively search fragment space, we assembled a database of >45 million chemical fragments with chemically meaningful structures (“possible fragments”). The database combines three large libraries: (1) all possible (chemically stable) fragments containing up to 11 atoms of C, N, O, and F from the Generated DataBase-11 (GDB-11) (26,434,571 fragments); (2) all additional possible fragments containing up to 11 atoms of C, N, O, Cl, and S from GDB-13 (1,089,000 fragments); and (3) all fragments in the Enamine readily accessible (REAL) database, which have improved synthetic accessibility and can vary in the number of atoms per fragment[38–42] (18,338,026 fragments). We then examined the structural novelty spanned by these fragment libraries by visualizing the chemical space they occupied relative to our training library and our manually compiled set of 559 known antibacterial compounds (Data S1). We used a t-distributed stochastic neighbor embedding (t-SNE) plot based on Tanimoto similarity using RDKit fingerprints as a distance metric, a commonly used measure of chemical similarity (Figure 1B). This two-dimensional projection of chemical space, in which structurally similar fragments or compounds cluster, showed that the fragment libraries substantially expand on the chemical diversity beyond that of known antibiotics (Data S1). Thus, our curation resulted in a consolidated, exhaustive database of 45,858,026 unique fragments spanning a diverse subset of chemical space.

Fragment-based generative design of antibacterial compounds

We virtually screened our fragment library using Chemprop models predicting antibacterial activity against *N. gonorrhoeae* (Figure 1C) and shortlisted those with prediction scores > 0.05 in the GDB databases and, due to better synthetic accessibility, > 0.1 in the Enamine REAL database (Figure S1E). This resulted in 3,844,505 fragments (8.4%) predicted to be active against *N. gonorrhoeae* (Figure 1D). To prioritize structurally novel and selective fragments with no obvious chemical liabilities, we implemented a series of filters on the fragments (Figures 1D and S1E). First, we removed fragments that were predicted to be cytotoxic (cytotoxicity prediction score > 0.5) by any of the three human cell cytotoxicity models (HepG2, HSkMC, and IMR-90). Second, we removed fragments containing pan-assay interference substructures (PAINS) or Brenk substructures, which are associated with unfavorable properties such as promiscuous binding, toxicity, chemical reactivity, and metabolic instability.[43,44] Third, we required that all remaining fragments be structurally distinct from those in known antibiotics, which we enforced by requiring the Tanimoto similarity to be <0.5 with respect to any compound in our curated set of 559 known antibacterial compounds (STAR Methods; Data S1; Figure S1E). The number of unique fragments passing these filters was 1,156,945 (Figure 1D).

To validate that our screening approach successfully identifies fragments with antibacterial activity, we searched for full compounds that contained any of our filtered fragments and selected those predicted to be antibacterial (compound prediction score > 0.1) and non-cytotoxic (cytotoxicity prediction score < 0.5), without PAINS or Brenk substructures, and structurally distinct from known antibiotics (Tanimoto similarity < 0.5). Applying these filters to 799,149 compounds from the Broad Institute,[6–8,45] we obtained 66 molecules representing 27 fragments for testing against *N. gonorrhoeae* ATCC 49226 (Figure 1E). We found that 7 of them inhibited the growth of *N. gonorrhoeae* at 50 μM, resulting in a working true discovery rate of 10.6% (Figure 1E; Table S2; Data S2). Notably, a single fragment, F1, was represented in two active Broad (BRD) compounds, BRD1 and BRD2 (Figure 1F), and their minimum inhibitory concentrations (MICs) ranged from 8 to 16 μg/mL. The compounds also exhibited a range of selectivity values, with half-maximal cytotoxic concentration (CC_{50}) of 32 to >128 μg/mL when tested against HEK293, HepG2, and HSkMC cells, respectively (Figure 1G). The therapeutic indices (TIs; ratio of human cell CC_{50} to MIC) were thus between 2 and 8 for the two compounds associated with F1. To identify molecules associated with F1 exhibiting higher TIs, we searched for analogs containing F1 and found a paucity of compounds in a purchasable compound library comprising >6 million molecules (STAR Methods). Therefore, we reasoned that a generative approach to the design of compounds based on F1 could enable the exploration of much larger chemical spaces and produce compounds with higher potency and selectivity.

We leveraged two generative machine learning algorithms: a genetic algorithm based on CReM and a fragment-based VAE (F-VAE)[17,20,46] (Figures 2A and 2C). CReM is a computational framework that starts with a compound of interest and generates new molecules by adding, replacing, or deleting atoms and functional groups. When additions are made, they are sampled from up to 1,557,992 distinct structures containing only common atoms (C, N, O, S, P, F, Cl, Br, I, and B) from ChEMBL.[47] In our pipeline, we coupled CReM to Chemprop models for antibacterial activity prediction (hereafter referred to as F-CReM), such that only high-scoring compounds containing F1 (prediction score > 0.7) were successively provided as inputs for the next round of molecule generation. After five rounds of selection, where each round resulted in progressively higher-scoring compounds (Figure 2B), we generated 518,203 F1-containing compounds. To obtain an experimentally tractable list of promising molecules, we filtered these compounds based on their predicted antibiotic activity and cytotoxicity, Tanimoto similarity to known antibiotics, and calculated synthetic complexity (based on either the synthetic accessibility score [SAscore],[48] retrosynthetic accessibility score [RAscore],[49] or R-score from Spaya Iktos[50]) (STAR Methods). We further ensured that the compounds of interest did not display PAINS or Brenk alerts. This resulted in 285 F-CReM-generated compounds with predicted activity against *N. gonorrhoeae* (Figure 2D).

In addition to F-CReM, which relies on computational sampling of chemical modifications, we employed a deep learning-based VAE for generative design. Specifically, we developed an F-VAE trained on all 1,686,695 compounds from ChEMBL (v2019).[47] The F-VAE architecture (Figure 2C) consists of a graph convolutional network encoder module, in which molecular graphs are encoded as latent vectors, as well as a recurrent graph decoder module, in which latent vectors are converted back to molecular graphs. The decoding procedure starts from a fragment and expands it atom-by-atom until the assembled structure converges into a compound. Compounds are designed by the F-VAE by sampling the latent space generated from an input fragment (e.g., by creating random latent vectors and passing them to the decoder). By applying the F-VAE, we generated 6,937,677 molecules containing fragment F1. We then used our Chemprop models to predict antibacterial activity for all of these molecules. Filtering the molecules similarly to above (STAR Methods; Figure S1F), we obtained 678 F-VAE-generated compounds with predicted activity against *N. gonorrhoeae* (Figure 2D).

To better understand and comparatively assess the chemical matter produced by the two generative models, we evaluated their physicochemical properties and synthesizability (Figure 2E). We found that F-CReM-generated compounds typically possessed lower molecular weights, lower calculated partition coefficients (calculated log *P*; clog*P*),[51] and lower calculated topological polar surface area (TPSA) values, compared to F-VAE-generated compounds. Both models

Please cite this article in press as: Krishnan et al., A generative deep learning approach to *de novo* antibiotic design, Cell (2025), https://doi.org/10.1016/j.cell.2025.07.033

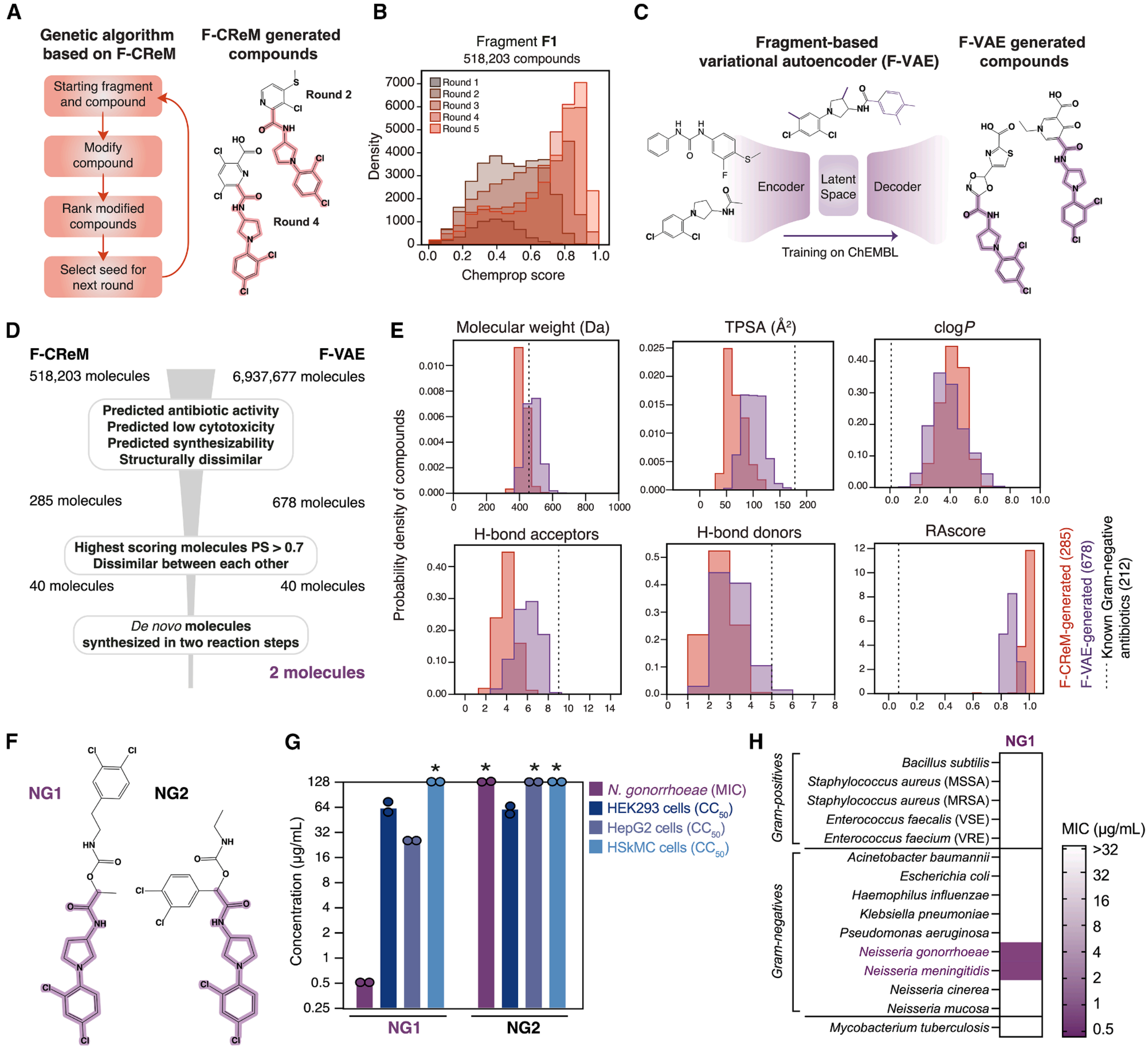

Figure 2. Generative deep-learning-guided design of compounds containing fragment F1 with predicted antibacterial activity
(A) Schematic of the genetic algorithm based on F-CReM and examples of filtered generated compounds, with fragment F1 highlighted.
(B) Distributions of antibacterial activity prediction scores from five rounds of compound generation using F-CReM.
(C) Schematic of the F-VAE algorithm and examples of filtered generated compounds, with fragment F1 highlighted.
(D) Computational filters applied to fragment-based designed compounds, resulting in two final sets of compounds shortlisted for chemical synthesis.
(E) Molecular weights, TPSA, calculated log *P* (clog*P*), hydrogen bond acceptors, hydrogen bond donors, and retrosynthetic accessibility score (RAscore) values for all filtered compounds generated by F-CReM and F-VAE, compared with the median of known Gram-negative antibiotics.
(F) Structures of two designed and synthesized compounds, **NG1** and **NG2**.
(G) MICs against *N. gonorrhoeae* ATCC 49226 and CC_{50} values of the compounds for three different human cell types. *n* = 2, * indicates values >128 µg/mL.
(H) MICs of compound **NG1** against various bacterial species. Results are representative of two biological replicates.
See also Figure S2.

generated synthesizable molecules, with comparable RAscores as computed by a machine learning (ML)-based synthetic feasibility estimator.[49] In general, all compounds generated based on F1 exhibited lower molecular weights, lower numbers of H-bond acceptors and donors, higher clog*P* values, and lower TPSA values compared to known Gram-negative antibiotics (Figure 2E). Taken together, our analyses suggest that our generative approach can produce realistic and synthesizable compounds with promising Chemprop prediction scores. We therefore aimed to synthesize and test several of these compounds.

Please cite this article in press as: Krishnan et al., A generative deep learning approach to *de novo* antibiotic design, Cell (2025), https://doi.org/10.1016/j.cell.2025.07.033

Synthesis and experimental validation of fragment-based designed compounds

Synthesizing deep learning-generated compounds can be challenging due to the possibility of formidable or undefined synthesis routes. Therefore, to obtain a diverse and reasonably sized set of compounds for synthesis, we prioritized compounds that were structurally dissimilar from each other and had the highest predicted antibacterial scores (>0.7) (Figure 2D; STAR Methods). This resulted in 80 compounds, which were evaluated by commercial chemical synthesis providers. After attempting to synthesize 27 compounds (9 from CReM and 18 from F-VAE), we successfully synthesized two (**NG1** and **NG2**) with high (>95%) purity (Figure 2F). Both molecules were generated by the F-VAE model. We empirically tested the compounds and found that **NG1**, but not **NG2**, inhibited the growth of *N. gonorrhoeae* ATCC 49226 with an MIC of 0.5 μg/mL (Figure 2G). Determining selectivity as before, we found that **NG1** had CC_{50} values of 25–128 μg/mL against HEK293, HepG2, and HSkMC cells, resulting in TIs of 50–256 (Figure 2G). **NG1** is structurally dissimilar to active compounds in the training dataset and possesses favorable physicochemical properties (Table S5). Interestingly, **NG1** exhibited narrow-spectrum activity against *N. gonorrhoeae* and *Neisseria meningitidis*—the only other pathogenic *Neisseria* species—but not against *Neisseria cinerea* and *Neisseria mucosa* (two human commensal species) or any other Gram-positive or Gram-negative species tested (Figure 2H). **NG1** also exhibited potent activity against highly drug-resistant *N. gonorrhoeae* strains, including the first strain found in the United States that had lost susceptibility not just to ceftriaxone but to all other drugs previously recommended for first-line treatment (Figure 3A; Table S4). These data consistently indicate that **NG1** is antibacterial against multidrug-resistant and pathogenic strains of *N. gonorrhoeae*, suggesting that it might act through a mechanism of action to which resistance has not yet evolved.

Mechanism of action, toxicology, and *in vivo* efficacy of NG1

We investigated the mechanism of action of **NG1** by first examining whether the compound was bactericidal. In a time-kill experiment using *N. gonorrhoeae* ATCC 49226, **NG1** exhibited concentration-dependent killing, with efficacy similar to that of azithromycin (Figure 3B), and a minimum bactericidal concentration (MBC) of 1 μg/mL (Figure 3C). In suppressor mutant generation experiments on solid agar, the frequency of resistance against **NG1** was 4.3×10^{-8} at 8× MIC. The spontaneously arising **NG1**-resistant isolates retained susceptibility to ceftriaxone, azithromycin, and ciprofloxacin, with unchanged MICs relative to those of the parental susceptible strain (Figure S2A). The lack of cross-resistance was supported by checkerboard assays demonstrating that **NG1** acted indifferently (neither synergistically nor antagonistically) to ceftriaxone, fosfomycin, and CCCP, indicating that **NG1** does not act similarly to other cell-wall- and membrane proton motive force (PMF)-targeting antibiotics (Figure S2B). Indeed, **NG1** did not alter the PMF, as measured by the potentiometric fluorophore 3,3-dipropylthiadicarbocyanine iodide ($DiSC_3$-[5]),[4,7,52] which displays an increase in fluorescence when the membrane potential, $\Delta\Psi$, is disrupted and a decrease in fluorescence when the pH gradient, ΔpH, is dissipated[52] (Figure S2C).

To investigate the mechanism of action further, we tested whether **NG1** treatment alters membrane fluidity using a Laurdan dye assay,[6] where cells with decreased membrane fluidity exhibit increases in Laurdan fluorescence. Treatment of *N. gonorrhoeae* cells with **NG1** resulted in a modest increase in Laurdan fluorescence, suggesting that **NG1** may act, in part, by decreasing membrane fluidity (Figure 3D). We hypothesized that this would compromise membrane integrity and tested this hypothesis by measuring the uptake of a hydrophobic fluorescent probe, 1-N-phenylnaphthylamine (NPN), which fails to penetrate intact outer membranes. **NG1** treatment resulted in a significant increase in NPN fluorescence, suggesting that the outer membranes of cells were indeed compromised (Figure 3E). **NG1**-treated *N. gonorrhoeae* cells also exhibited increased fluorescence of SYTOX green (a DNA-intercalating dye) that only penetrates cells with compromised membranes (Figure 3F), supporting the suggestion that membrane damage leads to cell death. We then directly examined the morphological changes induced by **NG1** treatment by performing cryogenic transmission electron microscopy (cryo-TEM) on *N. gonorrhoeae* ATCC 49226 cells. We found pronounced changes, where the **NG1**-treated cells showed reduced area and roundness and increased elongation (Figures S2D and S2E).

As **NG1** might compromise bacterial membranes by acting on membrane-related proteins, we performed a proteome integral solubility alteration (PISA) assay to study possible protein targets on a proteome-wide scale.[53] The assay revealed a striking destabilization of the lipooligosaccharide (LOS) export system protein, LptA (p value = 1.9×10^{-7}, $\log_2$ fold change = −2.4), upon treatment of *N. gonorrhoeae* lysate with **NG1** (Figure 3G). Time-resolved RNA sequencing experiments revealed a dose-dependent up-regulation of *lptA* in response to **NG1** treatment, in addition to changes in either upstream or downstream proteins of the LOS biosynthesis pathway (Figures 3H and S2F). Given **NG1**'s potential effect on LOS, we hypothesized that **NG1** would synergize with polymyxin B, an antibiotic that extracellularly binds lipid A,[54] and indeed observed a potent synergistic interaction (fractional inhibitory concentration index < 0.5) (Figure 3I). Taken together, these experimental results strongly suggest that LptA is the main target of **NG1**. This mechanism of action is notable, as LptA has been a proposed,[55] but as yet undrugged, antibiotic target in the LOS biosynthesis pathway.

Given that **NG1** appears to inhibit LptA, a protein absent in eukaryotic cells,[56] we aimed to further study its translational potential. We first carried out *in vitro* toxicology studies measuring human red blood cell (RBC) hemolysis and bacterial mutagenesis. We found that **NG1** was neither hemolytic nor mutagenic up to concentrations of 64 μg/mL, the highest tested (Figures S2G and S2H). Building on these observations, we tested the efficacy of **NG1** in a mouse model of *N. gonorrhoeae* vaginal infection. Here, ovariectomized and estradiol-treated mice were intravaginally inoculated with *N. gonorrhoeae* ATCC 49226. Two h later, mice were given their first dose of intravaginal **NG1** (1%), ceftriaxone (0.1%), or vehicle control, followed by four additional doses within a 24 h period (Figure 3J). We found that mice treated with **NG1** exhibited a significant decrease in vaginal bacterial load (two-sided Mann-Whitney U test, p = 0.0120) of ~3 logs in colony-forming units (CFUs) relative to vehicle-treated

Please cite this article in press as: Krishnan et al., A generative deep learning approach to *de novo* antibiotic design, Cell (2025), https://doi.org/10.1016/j.cell.2025.07.033

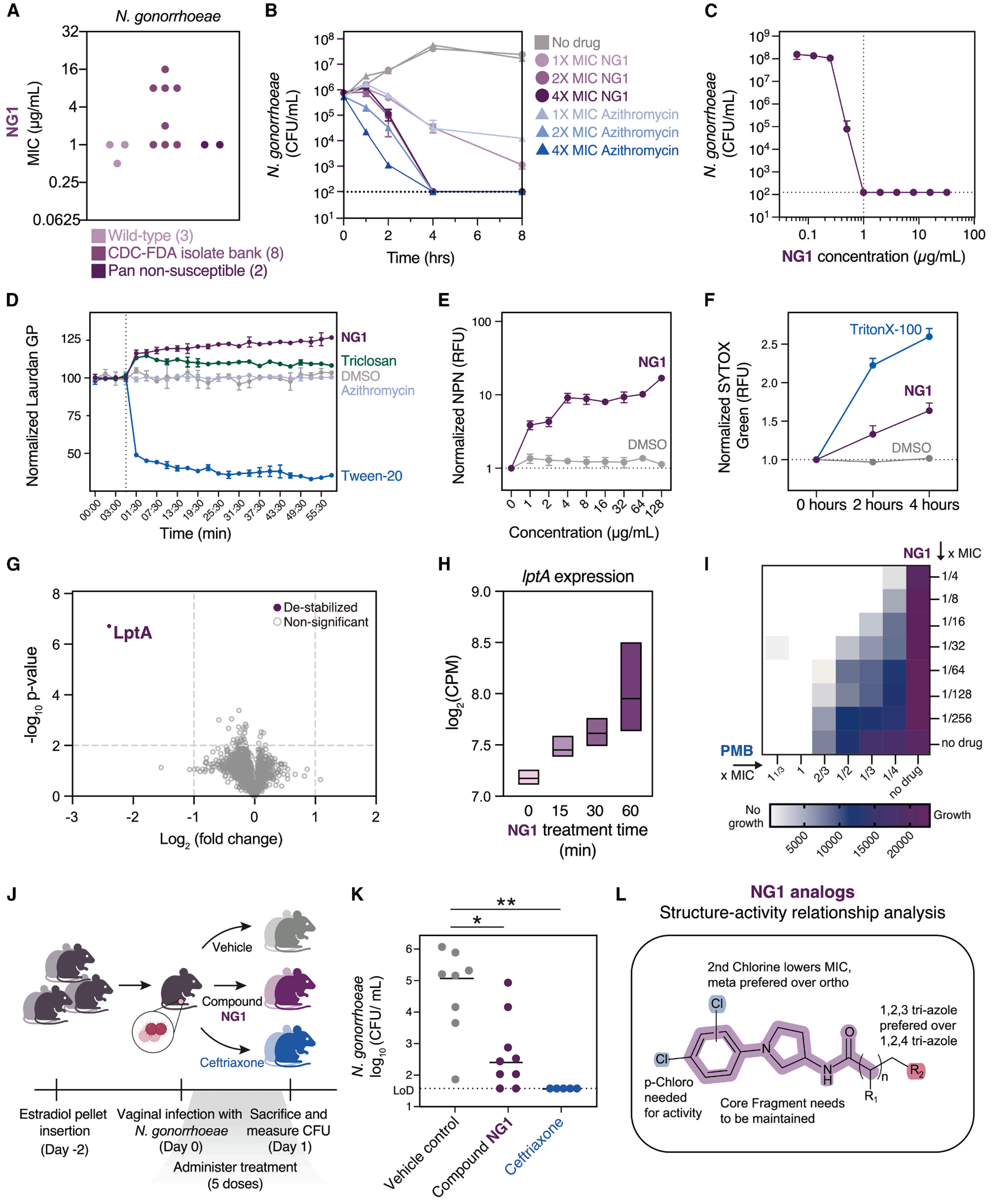

Figure 3. Mechanistic study and *in vivo* efficacy of compound NG1

(A) MICs against wild-type and antibiotic-resistant strains of *N. gonorrhoeae* (listed in Table S4). Each data point represents a strain tested in biological duplicates.
(B) Time-kill curves for ATCC 49226 treated with **NG1** or azithromycin. Mean ± SD; *n* = 2.

(legend continued on next page)

mice (Figure 3K). Furthermore, treatment with **NG1** was well-tolerated by all mice. Overall, these results support the translational potential of **NG1** with topical *in vivo* efficacy in treating a model of *N. gonorrhoeae* infection.

Synthesis and analysis of structural analogs of NG1

Building on the high selectivity of **NG1**, as well as to further test the functional significance of fragment F1, we investigated its structure-activity landscape by synthesizing and testing structural analogs. We synthesized 74 analogs primarily by altering two functional groups, R1 and R2, connected to the pyrrolidine ring and the amine, respectively (Figure S3A). Testing all analogs, we found eight active molecules against *N. gonorrhoeae* ATCC 49226, with MIC values between 16 and 32 μg/mL (Figures S3B and S3C). We also procured four analogs in the Enamine REAL Space library, and one of the four compounds, named **NG1 analog**, was active against *N. gonorrhoeae* ATCC 49226 with an MIC of 4 μg/mL. Additionally, its CC_{50} values against HEK293, HepG2, and HSkMC cells were higher than those of NG1 (Figure S3D). Given its promise for further development, we investigated the **NG1 analog**'s mechanism of action as above and found that it acted similarly to **NG1** (Figures S3E–S3G). From this analysis, we observed that compounds with an R1 group containing a 2,3-dichlorophenyl group were more effective at inhibiting *N. gonorrhoeae* than those with a 2,4-dichlorophenyl group, and compounds containing either group were more efficacious than those with a 2-chlorophenyl or phenyl group alone (Figure 3L). Together, these findings support the antibacterial activity of fragment F1 and its associated molecules, suggesting the possibility that additional optimization will improve the potency and selectivity of this structural class of antibacterial compounds.

Design of compounds with activity against *S. aureus*

Having taken a fragment-based approach to designing compounds active against *N. gonorrhoeae*, we asked whether the same approach could produce compounds active against a Gram-positive pathogen, *S. aureus*. To start, we predicted antibacterial activity against *S. aureus* using an ensemble of 20 GNN-based Chemprop models.[11,45,57] We used this ensemble of *S. aureus* models to screen our original set of 45,858,026 fragments using the same prediction score thresholds as before. Of these fragments, 432,919 (0.94%) were predicted to be active against *S. aureus* (Figure 4A), and 259,807 unique fragments remained after filtering for low predicted human cytotoxicity scores, no obvious chemical liabilities, and structural novelty. To validate that the identified fragments were associated with compounds with antibacterial activity against *S. aureus*, we searched our set of 799,149 compounds from the Broad Institute as well as the Enamine purchasable space to identify compounds containing these fragments. Applying similar filters as above to these compounds, we found 130 compounds representing 68 unique fragments that we procured for empirical testing against *S. aureus* RN4220 (Figure 4B). We found that 19 compounds inhibited the growth of *S. aureus* at 50 μM or below, resulting in a working true discovery rate of 14.6% (Figure 4B; Table S2; Data S2). Notably, the active fragment with the highest model prediction score, F2, was represented in the second-highest scoring compound, **EN1** (Figure 4C), with an MIC of 8 μg/mL against methicillin-susceptible *S. aureus* (MSSA) RN4220 and methicillin-resistant *S. aureus* (MRSA) BAA1556. **EN1** also exhibited half-maximal inhibitory concentration (CC_{50}) values ranging from 32 to >64 μg/mL when tested against HEK293, HepG2, and HSkMC cells (Figure 4D), indicating favorable selectivity.

EN1 contained a unique 1,4-epoxycyclohexane moiety, and a search within Enamine's 64 billion compound space yielded only 38 structures containing F2, suggesting that it might be a rare and appropriate starting point for generative AI algorithms that expand on its associated chemical space. We applied F-CReM and F-VAE to F2, and these models generated 141,109 and 3,297,292 molecules, respectively (Figure 4E). Filtering the resulting molecules similarly as before (STAR Methods; Figure S1F), we retained the top 210 compounds predicted to be antibacterial against *S. aureus*. These remaining compounds were down-selected to five compounds by a medicinal chemist to prioritize properties such as synthesizability, stability, permeability, drug-likeness, and diversity; however, none of these compounds were synthetically accessible within typical synthesis time frames and costs. To circumvent synthesizability obstacles and determine if preserving the entire F2 fragment is essential for our approach, we truncated F2 to a more synthetically

(C) MBC of **NG1** in ATCC 49226. Mean ± SD; *n* = 2.

(D) Membrane rigidification of ATCC 49226 treated with **NG1** at 64 μg/mL and control compounds, as measured by the Laurdan generalized polarization (GP). Mean ± SD; *n* = 2.

(E) Loss of membrane integrity of ATCC 49226 treated with **NG1** and DMSO, as measured by the uptake of the hydrophobic fluorescent probe, 1-N-phenylnaphthylamine (NPN). Mean ± SD; *n* = 2.

(F) Membrane permeabilization of ATCC 49226 treated with **NG1** or Triton X-100, as seen by a time-dependent increase in SYTOX green fluorescence signal normalized to the untreated control. Mean ± SD; *n* = 2.

(G) Volcano plot of PISA results from FA 1090 lysate treated with **NG1** compared with the vehicle control. The most significantly affected protein, LptA, is shown in purple.

(H) Expression levels of *lptA* in FA 1090 treated with **NG1** at 4× MIC, expressed in $\log_2$ counts-per-million (CPM).

(I) Checkerboard study of **NG1** and polymyxin B (PMB) in ARB #0187 revealing a synergistic effect. Data are representative of biological duplicates.

(J) Schematic of the *in vivo* study of **NG1** in the *N. gonorrhoeae* vaginal infection model using strain ATCC 49226. Treatment with vehicle, **NG1**, or ceftriaxone was administered intravaginally for five doses.

(K) Bacterial titers in vaginal lavage fluid. Horizontal lines represent median $\log_{10}$ CFU/mL values. Data represent treatment with vehicle control (*n* = 8), **NG1** (*n* = 9), or ceftriaxone (*n* = 5). Two-sided Mann-Whitney U test compared with vehicle: $^*p \leq 0.05$, $^{**}p \leq 0.01$. Horizontal lines represent medians.

(L) Summary of a structure-activity relationship analysis for **NG1**.

See also Figures S2 and S3.

Please cite this article in press as: Krishnan et al., A generative deep learning approach to *de novo* antibiotic design, Cell (2025), https://doi.org/10.1016/j.cell.2025.07.033

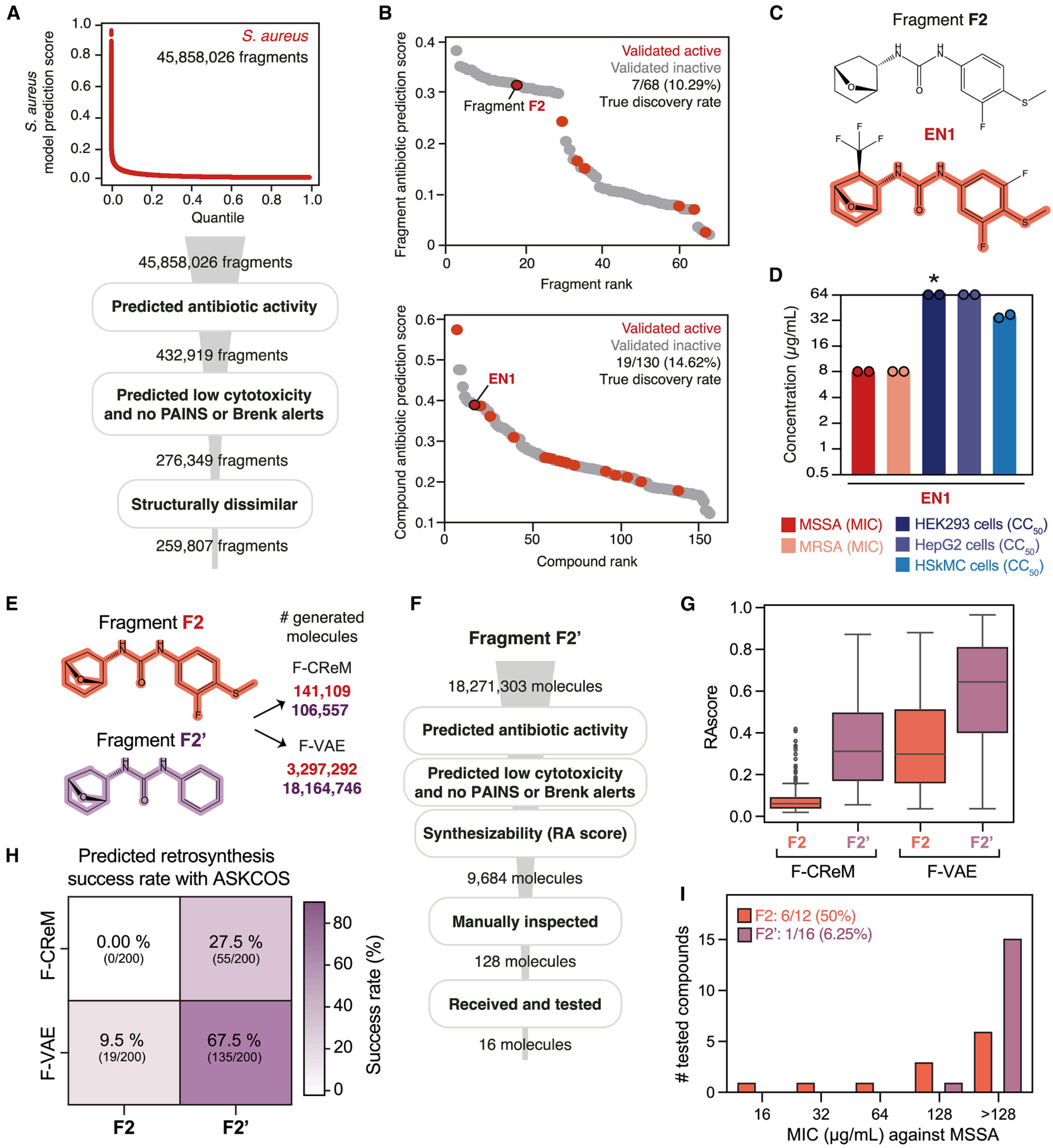

Figure 4. Effect of fragment modification on synthesizability and antibacterial activity

(A) Rank-ordered fragment prediction scores as determined by the *S. aureus* antibacterial activity model (above) and computational filters applied to the fragments (below).

(B) Rank-ordered fragment (above) and compound (below) prediction scores for available compounds procured for empirical testing at 50 μM.

(C) Structure of fragment F2 and its associated active compound from (B). The fragment is highlighted in **EN1**.

(D) MIC and CC_{50} values for **EN1**. *n* = 2, * indicates values >64 μg/mL.

(E) Structures of fragment F2 and the truncated fragment F2′, with the number of molecules generated for both fragments by the F-CReM and F-VAE models.

(F) Computational filters applied to down-selected compounds using fragment F2′.

(G) RAscore of molecules generated by F-CReM and F-VAE using fragments F2 and F2′.

(legend continued on next page)

accessible starting point, F2′ (Figure 4E). We used F-CReM and F-VAE to generate 106,557 and 18,164,746 molecules based on F2′ and down-selected 9,684 molecules as before (Figure 4F; STAR Methods). As expected, the molecules associated with F2′ were more likely to be synthesizable than those associated with F2, as measured by two metrics: RAscore (Figure 4G) and a retrosynthesis planning tool, ASKCOS (Automated System for Knowledge-based Continuous Organic Synthesis) (Figure 4H).[58] Intriguingly, F-VAE-generated molecules were consistently predicted and selected by a medicinal chemist to be more synthesizable than those from F-CReM and exhibited more drug-like properties (Figure S4A; Table S3). Confirming these predictions, we were able to synthesize 16 F-VAE-designed molecules within typical synthesis time frames and costs. We found that only one of these 16 compounds (6.25%) (Figure S4B; Data S2) demonstrated activity against *S. aureus* RN4220, with a marginal MIC of 128 μg/mL, the highest concentration tested (Figure 4I). By contrast, six of 12 additional molecules (50%) (Figure S4B; Data S2) procured from the Enamine REAL Space containing the original F2 fragment displayed activity, exhibiting MICs as low as 16 μg/mL (Figure 4I). Together, these findings indicate that preservation of F2 is important for antibacterial activity and that designing compounds based on this particular fragment appears to result in a trade-off between antibacterial activity and synthesizability.

Generation, synthesis, and experimental validation of *de novo* designed compounds

To further investigate the generality of our approach, we asked if our generative models could design antibacterial molecules without the need for specific fragments as starting points (Figure 5A). We modified our models by providing either ammonia, methane, or water as inputs to CReM (Figure 5B) and no fragment as input to a junction tree variational autoencoder (JT-VAE) (Figure 5C). Together, the models generated 29,014,974 molecules. Interestingly, the JT-VAE model produced more drug-like molecules (Figure 5D; Table S3), while compounds produced by CReM tended to have high molecular weights and many H-bond acceptors and donors (which could reduce membrane permeability) (Figure 5D; Table S3). CReM compounds were predicted to be highly unsynthesizable by both the RAscore (Figure 5D) and the ASKCOS retrosynthesis prediction tool (Figure S5A; Table S3). We therefore prioritized molecules generated by JT-VAE and filtered them for favorable properties, including high predicted antibacterial scores against *S. aureus*, low predicted cytotoxicity scores, and Tanimoto similarity to known antibiotics (Figure S5B). The down selection resulted in 4,831 molecules that were manually inspected and shortlisted to 90 compounds based on synthesizability and diversity (Figure 5E). After review by a chemical synthesis vendor, we procured 22 molecules and tested them against MSSA RN4220 and MRSA BAA1556 at a high starting concentration of 64 μg/mL. Remarkably, six molecules (27.3%; **DN1**–**DN6**) showed antibacterial activity and were structurally dissimilar to each other (Figures 5F and 5G; Data S2), suggesting that our generative models can design antibacterial molecules *de novo* without the requirement of a fragment as a starting point.

To further investigate the six active compounds, we determined their MICs against MSSA RN4220, MRSA BAA1556, and, as a starting point for assessing spectrum, *N. gonorrhoeae* ATCC 49226. **DN1** was the most potent and selective against *S. aureus*, with an MIC of 4 μg/mL for both MSSA RN4220 and MRSA BAA1556 and a TI of 32 for HEK293, HepG2, and HSkMC cells. By contrast, **DN4** was the least potent and selective, with an MIC of 64 μg/mL for *S. aureus* and a TI of 2 (Figure 6A). Four of the six compounds also exhibited MICs ≤ 8 μg/mL for *N. gonorrhoeae*, despite being selected based on their *S. aureus* model prediction scores. To further assess their spectrum of activity, we tested each compound against a panel of Gram-positive and Gram-negative species. We found that **DN1**–**DN3** exhibited broad-spectrum activity against Gram-positive bacteria, including *Bacillus subtilis* and vancomycin-susceptible *Enterococcus faecalis*. However, none of the six compounds inhibited the growth of other tested Gram-negative species or Gram-neutral *Mycobacterium tuberculosis* (Figure 6B; Data S2). Interestingly, **DN1**–**DN3** gained activity against *E. coli* when the outer membrane was permeabilized through genetic (*lptD4213*) or chemical (polymyxin B nonapeptide co-treatment) means, or when efflux pumps were genetically disrupted (Δ*tolC*). In combination with polymyxin B nonapeptide, **DN1**–**DN3** also effectively inhibited the growth of wild-type *E. coli*, *A. baumannii*, and *P. aeruginosa*, and **DN1** gained activity against *K. pneumoniae* and *M. tuberculosis* (Data S2). These findings suggest that the efficacy of **DN1**–**DN3** is hindered by outer membranes, which may act to block penetration or increase efflux of these compounds.

Although **DN1**–**DN3** exhibited similar spectra of activity to each other, performing membrane PMF assays as above for *S. aureus* cells treated with each of **DN1**–**DN6** resulted in markedly different DiSC$_3$(5) fluorescence profiles (Figure 6C), consistent with the observation that these compounds are structurally distinct. **DN1** and **DN6** treatment resulted in similar dissipation of $\Delta\Psi$; however, microscopic imaging of morphological changes in *B. subtilis* 168 revealed that treatment with **DN6** resulted in filamentation and membrane rupture after 2 h, in contrast to treatment with **DN1**–**DN5** (Figures 6D, 6E, and S6A). Given **DN1**'s potency, we investigated its potential membrane-active mechanism by testing whether **DN1** alters membrane fluidity using a Laurdan dye assay as before.[6] Treatment of *S. aureus* cells with **DN1** resulted in a modest increase in Laurdan fluorescence (Figure 6F), suggesting a decrease in membrane fluidity. Performing cryo-TEM on both MSSA RN4220 and *N. gonorrhoeae* ATCC 49226 cells treated with compound at 4× MIC, we found pronounced morphological changes in the membranes of both

(H) Predicted retrosynthesis success rates as determined by ASKCOS for molecules generated by F-CReM and F-VAE using fragments F2 and F2′.

(I) MICs of 12 compounds from the Enamine REAL space with fragment F2 and 16 *de novo* designed and synthesized compounds with the fragment F2′ against *S. aureus* RN4220.

See also Figure S4.

Please cite this article in press as: Krishnan et al., A generative deep learning approach to *de novo* antibiotic design, Cell (2025), https://doi.org/10.1016/j.cell.2025.07.033

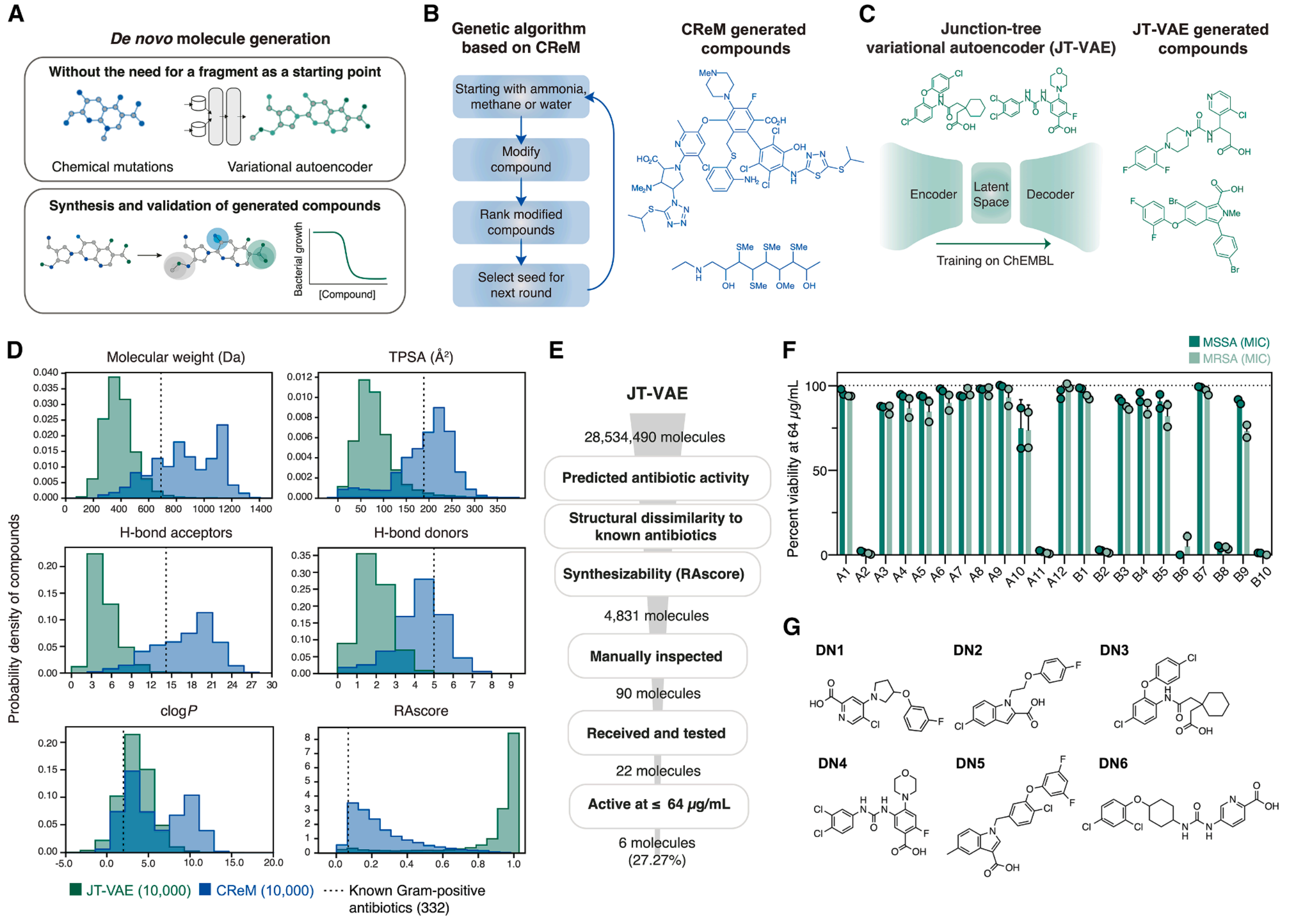

Figure 5. *De novo* generation of antibacterial compounds without a fragment starting point

(A) Schematic of the *de novo* generative approach.

(B) Schematic of the *de novo* genetic algorithm based on CReM and examples of generated compounds.

(C) Schematic of the *de novo* JT-VAE algorithm and examples of generated compounds.

(D) Molecular properties and RAscores for a random subset of 10,000 compounds generated by the *de novo* CReM and JT-VAE models, compared with the median of known Gram-positive antibiotics.

(E) Computational filtering and summary of experimental results for JT-VAE-designed compounds.

(F) Experimental validation of 22 JT-VAE-designed molecules against *S. aureus* when tested at 64 μg/mL. *n* = 2.

(G) Structures of the six *de novo* designed compounds with activity against MSSA RN4220 and MRSA BAA1556.

See also Figure S5.

bacteria. In MSSA, we observed thickening of the membrane and increased perimeter (Figures 6G, 6H, and S6B), and in *N. gonorrhoeae*, we observed dislodging of the membrane and increased cell swelling (Figure S6C), quantified further by increased cell roundness and decreased elongation (Figure S6D). Overall, these results indicate that our *de novo* design models can generate bona fide antibacterial compounds and that a subset of structurally distinct compounds exhibit different, membrane-active mechanisms of action.

Resistance and *in vivo* efficacy of DN1

Building on our previous findings, we aimed to further investigate the translational relevance of **DN1**. Time-kill experiments indicated that **DN1** substantially decreased log-phase MSSA RN4220 CFUs as early as 2 h post-treatment (Figure 7A), exhibiting faster bactericidal activity than that of vancomycin, a first-line antibiotic for treating *S. aureus* infections. Additionally, the MBC of **DN1** was 8 μg/mL for MSSA RN4220 (Figure 7B). In spontaneous mutant generation experiments on solid agar, no colonies emerged after 7 days of incubation at 4× and 8× MIC, suggesting a low frequency of resistance ($<9.6 \times 10^{-9}$ for MSSA RN4220 and $<1.0 \times 10^{-9}$ for MRSA BAA1556). Similarly, the MIC of **DN1** for MRSA BAA1556 did not meaningfully increase after 30 serial passages in LB (lysogeny broth) or LB supplemented with 0.002% Tween. **DN1** also inhibited the growth of 10 multidrug-resistant Gram-positive isolates from the CDC-FDA (Food and Drug Administration) Antimicrobial Resistance Isolate Bank (ARB), including isolates from the vancomycin-intermediate *S. aureus* (VISA), aminoglycoside/tetracycline-resistant (ATR), and tedizolid/linezolid (oxazolidinone)-resistant staphylococci (TLZD)

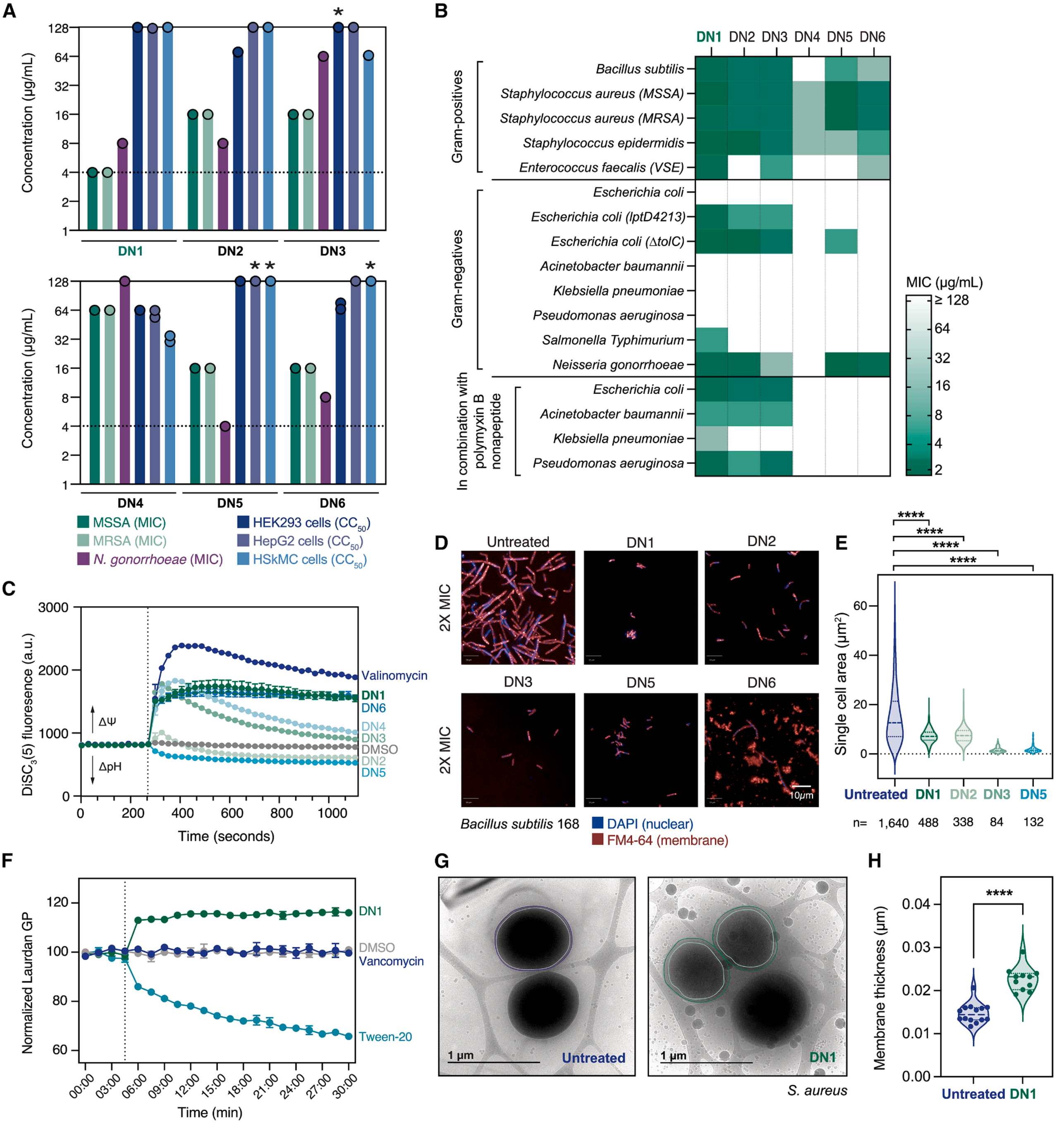

Figure 6. Characterization of *de novo* designed compounds DN1–DN6

(A) MICs against *S. aureus* RN4220, MRSA BAA1556, *N. gonorrhoeae* ATCC 49226, and CC_{50} values of the compounds in three different human cell types. *n* = 2, * indicate values >128 μg/mL.

(B) MICs against various Gram-positive species (top) and Gram-negative bacterial species (middle), or in combination with a sub-MIC concentration of polymyxin B nonapeptide (bottom). *n* = 2. See also Table S4.

(C) $DiSC_3(5)$ fluorescence of *S. aureus* RN4220 treated with **DN1–DN6**, valinomycin (positive control), and DMSO (negative control).

(D) Images of *B. subtilis* 168 cells treated with the active *de novo* designed compounds at 2× MIC for 2 h. DAPI in blue and FM4-64 in red.

(E) Area of untreated and compound-treated (2× MIC) *B. subtilis* cells, where *n* is the number of cells quantified and $****p \leq 0.0001$, evaluated using a two-sided Mann-Whitney U test.

(legend continued on next page)

Please cite this article in press as: Krishnan et al., A generative deep learning approach to *de novo* antibiotic design, Cell (2025), https://doi.org/10.1016/j.cell.2025.07.033

panels, with MICs of 8 μg/mL across all tested isolates (Figure 7C; Table S4). Consistent with its activity against *N. gonorrhoeae* ATCC 49226, **DN1** exhibited MICs at or below 16 μg/mL against a panel of drug-resistant *N. gonorrhoeae* isolates (Figure 7D).

As **DN1** exhibited a favorable resistance profile and physicochemical properties (Table S5), we aimed to evaluate its potential for therapeutic development. For this, we tested **DN1** for efficacy in treating a mouse model of MRSA BAA1556 skin infection. In this model, each mouse was rendered neutropenic and inflicted with a skin wound. After inoculation of $\sim 10^5$ CFU of MRSA, each wound was topically treated with **DN1** (1% w/v) six times before all mice were sacrificed, and the wounds were excised for CFU determination 25 h after infection (Figure 7E). We found that treatment with **DN1** significantly decreased the average bacterial load by 10-fold relative to vehicle (two-sided Mann-Whitney U test, $p = 0.0043$), with efficacy similar to that of fusidic acid, a positive control antibiotic used in the clinical treatment of *Staphylococcus* infections (Figure 7F). Together, these findings support the translational potential of **DN1**, highlighting its efficacy in treating a model of topical staphylococcal infection.

Synthesis and analysis of structural analogs of DN1

As a starting point for further developing and optimizing **DN1**, we investigated its structure-activity landscape similarly to **NG1**. We modified the position or type of halogen atom (Cl or F) on the aryl ring and replaced the central pyrrolidine with 4- or 6-membered nitrogen-containing heterocycles. Of the 19 analogs synthesized (Data S2) that include these modifications, we found that five analogs exhibited MICs ranging from 2 to 8 μg/mL when tested against MSSA RN4220, MRSA BAA1556, and a panel of 10 MRSA isolates from the ARB (Figures S7A and S7B). A more potent analog, **DN1–164**, exhibited MICs $\leq$ 4 μg/mL for all antibiotic-resistant *S. aureus* strains tested and against wild-type *N. gonorrhoeae* without increase in cytotoxicity against human cells, resulting in TIs > 32 (Figure S7C). The most potent analogs (**DN1–154**, **DN1–164**, and **DN1–173**) increased DiSC$_3$(5) fluorescence in *S. aureus* RN4220 cells, suggesting that, similar to **DN1**, these analogs dissipate the $\Delta\Psi$ component of the PMF (Figure S7D). Furthermore, the chemical structures of the active analogs suggest that substitutions of the central pyrrolidine are tolerated, the placement of a halogen in the meta position of the aryl ring might improve potency, and the carboxylic acid is needed for activity (Figure 7G). Thus, these findings highlight a broad structure-activity landscape relevant to improving the selectivity of our *de-novo*-generated compound, **DN1**, and its associated chemical series.

DISCUSSION

The unmet need for novel antibiotics is large and growing. Virtual screening of chemical compound libraries offers a way to leverage the diversity of enumerated chemical space, yet these libraries sample an infinitesimal fraction of drug-like chemical space, which is estimated to contain $\sim 10^{60}$ compounds. Here, we have presented a deep learning-enabled approach to the generative design of compounds with antibacterial activity. Using GNNs as scoring functions, we first comprehensively screened >45 million chemical fragments to identify selective antibacterial starting points against *N. gonorrhoeae* or *S. aureus*. We then developed two models—a genetic algorithm-based model (CReM) and a variational autoencoder (VAE)—to generate compounds based on these fragments. While fragments offer consistent and tractable starting points, these models can also generate molecules *de novo*, without any fragment input, as demonstrated. Of the 24 compounds that we designed using these generative approaches and subsequently synthesized, two compounds—**NG1** and **DN1**—possessed narrow-spectrum activity against pathogenic *Neisseria* and broad-spectrum activity against Gram-positive bacteria and *N. gonorrhoeae*, respectively. Both compounds exhibited mechanisms of action distinct from those of often-used antibiotics and were effective in reducing bacterial titers in different animal models of infection. Additionally, both compounds exhibited a structure-activity landscape that can be productively used for further optimization. Together, our results enable the generative design of two unique structural classes of antibacterial compounds and demonstrate the ability of our platform to explore uncharted regions of chemical space.

Here, we focused on implementing two molecular generation models: CReM and VAE. Despite CReM's reliance on rule-based features of bioactive molecules to either grow or introduce modifications and generate structurally diverse molecules, our VAE-based models consistently generated compounds that were more drug-like and synthesizable. Our platform is modular in that other generative models, such as generative adversarial networks,[15,59] molecular transformers,[60] flow-based models,[61] diffusion-based methods,[21,62–64] and fragment linkers,[65] can be readily incorporated. Combining these diverse approaches and continuing to explore fragments that lead to readily synthesizable molecules will enable new portions of chemical space to be harnessed for successful *de novo* design efforts.

Our approach also allowed for the models to have different chemical starting points, enabling either constrained (fragment-based) or unconstrained (*de novo*) design. Using fragments as starting points possesses several unique advantages. First, it allows one to comprehensively search molecular building blocks (e.g., all possible combinations of up to 11 atoms comprised of C, N, O, and F) to systematically identify and exploit underexplored areas of chemical space that would otherwise be unlikely to be sampled by generative methods. The disparity between the millions of fragments that our GNN models predicted to be antibacterial and the hundreds of fragments that could be found

(F) Membrane rigidification of RN4220 treated with **DN1** at 32 μg/mL and control compounds, as measured by the Laurdan generalized polarization (GP). Mean ± SD; $n = 2$.

(G) Cryo-TEM images of untreated and **DN1**-treated (4× MIC) *S. aureus*.

(H) Quantification of *S. aureus* membrane thickness (untreated, $n = 14$; **DN1**, $n = 11$). ****$p \leq 0.0001$, evaluated using a two-sided Mann-Whitney U test.

See also Figure S6.

Please cite this article in press as: Krishnan et al., A generative deep learning approach to *de novo* antibiotic design, Cell (2025), https://doi.org/10.1016/j.cell.2025.07.033

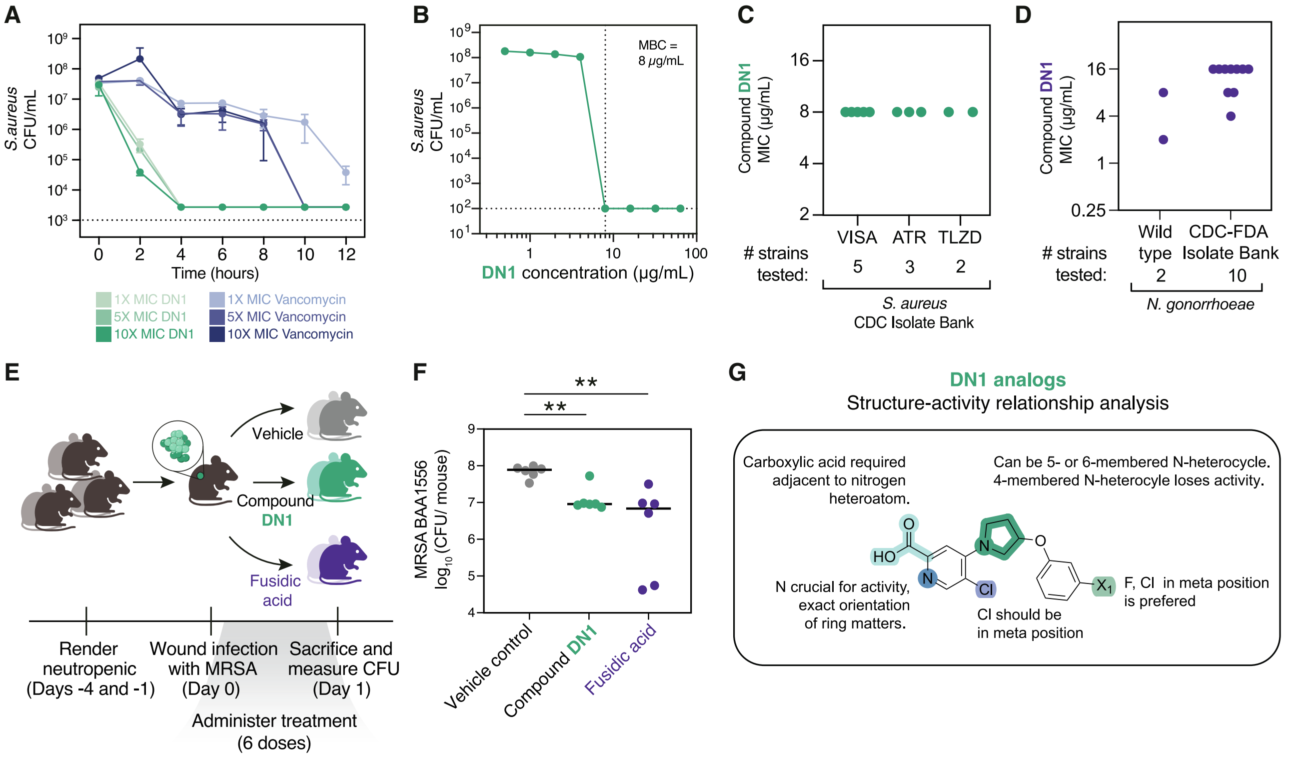

Figure 7. Mechanistic study and *in vivo* efficacy of DN1

(A) Time-kill curves for *S. aureus* RN4220 treated with **DN1** or vancomycin. Mean ± SD; *n* = 2.

(B) MBC of **DN1** in RN4220. Mean ± SD; *n* = 2.

(C) MICs against antibiotic-resistant strains of *S. aureus* (listed in Table S4). Each data point represents a strain tested in biological duplicates.

(D) MICs against wild-type and antibiotic-resistant strains of *N. gonorrhoeae* (listed in Table S4). Each data point represents a strain tested in biological duplicates.

(E) Schematic of the *in vivo* study of **DN1** in a neutropenic mouse skin infection model using MRSA strain ATCC BAA1556. Treatment with vehicle, **DN1**, or fusidic acid was administered topically in six doses.

(F) Bacterial titers in skin tissue. Horizontal lines indicate median CFU/mouse values. Data represent treatment with vehicle control (*n* = 6), **DN1** (*n* = 6), or fusidic acid (*n* = 6). Two-sided Mann-Whitney U test compared with vehicle treatment: $^*p \leq 0.05$, $^{**}p \leq 0.01$.

(G) Summary of the structure-activity relationship analysis for **DN1**.

See also Figures S6 and S7.

within commercially available libraries suggests that much of antibacterial chemical space indeed remains underexplored. Second, by screening fragments based on target-agnostic phenotypic outcomes, specifically bacterial growth inhibition, our method increases the likelihood of discovering molecules with unique mechanisms of action that potentially circumvent existing antimicrobial resistance mechanisms. Lastly, if chosen carefully, a highly synthesizable starting point can constrain the search space to realistic, drug-like molecules, reduce the risk of generating implausible structures, and facilitate a coherent structure-activity relationship analysis. In contrast to the fragment-based approach, *de novo* design without predefined chemical starting points enables unrestricted exploration of chemical space and more variability in the properties of the generated compounds. After manual inspection and stringent filtering for structural novelty, low predicted cytotoxicity, and synthesizability, the tested *de novo* designed compounds produced a high working true discovery rate of 27% and were structurally diverse with drug-like properties. Importantly, compounds from both approaches exhibited antibacterial activity against highly drug-resistant strains of *N. gonorrhoeae* and Gram-positive bacteria, highlighting the versatility of generative AI models when coupled to antibacterial scoring functions.

Overall, these findings underscore the value of multiple approaches to the generative design of antibiotics and that the choice of a chemical starting point should be guided by strategic considerations, including chemical novelty, diversity, and synthesizability. We anticipate that future studies will leverage multi-objective optimization frameworks to identify compounds that simultaneously satisfy multiple criteria, including high antibacterial activity, synthetic accessibility, low toxicity, and favorable drug-like properties such as metabolic stability, low protein binding, and optimal pharmacodynamics.

Limitations of the study

Despite our observations of high working true discovery rates and promising chemical diversity of generated molecules, it is

Please cite this article in press as: Krishnan et al., A generative deep learning approach to *de novo* antibiotic design, Cell (2025), https://doi.org/10.1016/j.cell.2025.07.033

possible for the ML models used here to produce false positive predictions or generate structurally non-diverse molecules. Model outputs should therefore be analyzed on a case-by-case basis, and when such outputs appear promising, the compounds should be empirically tested. Furthermore, the utility of our generative approach heavily relies on the ability to synthesize compounds for validation. As evidenced by the small number of generated compounds that we could synthesize, chemical synthesis remains a challenge when molecules are not designed according to prespecified synthetic routes. Improvements in synthesizability predictors and complex retrosynthesis-based algorithms should enable larger sets of *de novo* designed compounds to be experimentally tested and validated.

RESOURCE AVAILABILITY

Lead contact

Further information and requests for resources should be directed to and will be fulfilled by the lead contact, James J. Collins (jimjc@mit.edu).

Materials availability

All unique/stable reagents generated in this study are available from the lead contact with a completed materials transfer agreement.

Data and code availability

- All data reported in this paper will be shared by the lead contact upon request.
- A code platform for reproducing all analyses in this work is available via the GitHub repository: https://github.com/aartikrish/de-novo-antibiotics.
- Data generated from the computational pipeline and experimental chemical screening are available as Data S1 and S2, as well as on the Zenodo repository: https://doi.org/10.5281/zenodo.15191826.
- Data generated from chemical synthesis of the *de novo* designed compounds and RNA sequencing experiments can be accessed via the Zenodo repository: https://doi.org/10.5281/zenodo.15191826.
- Proteomics data are available at PRIDE under accession PRIDE: PXD063107.
- Any additional information required to re-analyze the data reported in this paper can be made available from the lead contact upon request.

ACKNOWLEDGMENTS

This work was supported by National Institutes of Health (NIH) grants R01 AI146194 and K25AI168451, DTRA grant HDTRA-12210032, and the Broad Institute of MIT and Harvard. This work was supported in part by Oracle Cloud credits and related resources provided by Oracle for Research. We thank MIT SuperCloud and Lincoln Laboratory Supercomputing Center for providing high-performance computing resources; Chemistry Center for Combating Antibiotic-Resistant Bacteria (CC4CARB), an National Institute of Allergy and Infectious Diseases (NIAID)-led partnership with Research Triangle Institute (RTI), for designing and synthesizing compound analogs under contract number 75N93021C00002; and the SeqCenter for assistance with RNA sequencing analysis. R-scores and chemical synthesis advice were provided by Iktos (Spaya) as part of an academic partnership. Some illustrations were adapted from BioRender.com. We thank Dr. Jean-Louis Reymond of the University of Bern for the academic license to access the Generated DataBase libraries and Dr. Dongsoo Yun, Nanotechnology Material Core Staff at the Koch Institute for Integrative Cancer Research, Cambridge, MA, USA, for performing the cryo-TEM imaging. The authors also thank Armaun Sanayei and Christopher Giuliano for their time and for providing constructive feedback on the manuscript and computational analysis and Dr. Sandy Gould, Dr. Aakanksha Gulati, Dr. Akhila Kosaraju, Dr. Leanne Minall, and Dr. Joseph Vacca for their helpful insights on the *de novo* designed molecules. Chemical synthesis was provided by Enamine Ltd. (Kyiv, Ukraine). A.K. was supported by the Swiss National Science Foundation under grant number SNSF_203071. M.N.A. was supported by the NIH under awards T32CA921641 and K08AI182474. J.A.V. was supported by a scholarship from the Siebel Scholars Foundation. W.J. was supported by the Eric and Wendy Schmidt Center at the Broad Institute of MIT and Harvard. A.L. was supported by the Knut and Alice Wallenberg Foundation under award KAW2022.0347. J.F. was supported by the National Science Foundation Graduate Research Fellowship under grant no. 2141064. R.D. was supported by NIH award number T32GM144273 from the National Institute of General Medical Sciences. A.A.S. was supported by a Swedish Research Council grant under award 2023-02692 and Karolinska Institutet Faculty Funding under award 2-188/2022. Chemical proteomics at the Karolinska Institutet (Chemistry I Division, MBB Department), Unit of SciLifeLab, and node of the Swedish National Infrastructure for Biological Mass Spectrometry (BioMS), provided full support in the experimental design, performance, and data analysis of the PISA experiments. S.G.P. and Y.H.G. were supported by the NIH under awards R01 AI132606 and R01 AI153521. F.W. was supported by the National Institute of Allergy and Infectious Diseases of the National Institutes of Health under award number K25AI168451 and the James S. McDonnell Foundation. This work is part of the Antibiotics-AI Project, which is directed by J.J.C. and supported by the Audacious Project, Flu Lab, LLC, the Sea Grape Foundation, Rosamund Zander and Hansjorg Wyss for the Wyss Foundation, and an anonymous donor.

AUTHOR CONTRIBUTIONS

Conceptualization, A.K., M.N.A., J.A.V., F.W., and J.J.C.; methodology, A.K., M.N.A., J.A.V., W.J., and F.W.; algorithm development and execution, A.K., M.N.A., J.A.V., W.J., and F.W.; computational analysis, A.K., M.N.A., J.A.V., W.J., L.S., A.H., J.F., J.C.C., D.R., P.E., M. Gaborieau, and F.W.; mechanistic characterization, A.K., M.N.A., N.M.D., L.S., Y.Z., S.M.M., A.H., P.B., R.D., R.S.L., M.-S.A., M. Gaborieau, M. Gaetani, S.G.P., S.O., and F.W.; chemistry expertise and analog design, A.L., L.K., Y.S.M., B.B., and C.J.; manuscript writing, A.K., M.N.A., J.A.V., and F.W.; manuscript review and editing, all authors; supervision, A.K., M.N.A., E.L., Y.H.G., A.A.S., C.W.C., F.W., and J.J.C.; funding acquisition, F.W. and J.J.C.

DECLARATION OF INTERESTS

J.J.C. is an academic co-founder and Scientific Advisory Board chair of Phare Bio, a non-profit venture focused on antibiotic drug development, an academic co-founder and board member of Cellarity, and the founding Scientific Advisory Board chair of Integrated Biosciences. M.N.A. is a co-founder and consultant to Day Zero Diagnostics. F.W. is a co-founder of Integrated Biosciences. R.S.L. and S.O. have equity interests in Integrated Biosciences. Y.S.M. is an employee of Enamine Ltd. and a scientific advisor of Chemspace LLC.

STAR★METHODS

Detailed methods are provided in the online version of this paper and include the following:

Please cite this article in press as: Krishnan et al., A generative deep learning approach to *de novo* antibiotic design, Cell (2025), https://doi.org/10.1016/j.cell.2025.07.033

SUPPLEMENTAL INFORMATION

Supplemental information can be found online at https://doi.org/10.1016/j.cell.2025.07.033.

Received: February 24, 2024
Revised: April 21, 2025
Accepted: July 20, 2025

REFERENCES

1. GBD 2021 Antimicrobial Resistance Collaborators (2024). Global burden of bacterial antimicrobial resistance 1990–2021: a systematic analysis with forecasts to 2050. Lancet *404*, 1199–1226. https://doi.org/10.1016/S0140-6736(24)01867-1.
2. Centers for Disease Control and Prevention (CDC). (2019). Antibiotic resistance threats in the United States, 2019. https://doi.org/10.15620/cdc:82532.
3. Spellberg, B., Powers, J.H., Brass, E.P., Miller, L.G., and Edwards, J.E. (2004). Trends in antimicrobial drug development: implications for the future. Clin. Infect. Dis. *38*, 1279–1286. https://doi.org/10.1086/420937.
4. Stokes, J.M., Yang, K., Swanson, K., Jin, W., Cubillos-Ruiz, A., Donghia, N.M., MacNair, C.R., French, S., Carfrae, L.A., Bloom-Ackermann, Z., et al. (2020). A deep learning approach to antibiotic discovery. Cell *180*, 688–702.e13. https://doi.org/10.1016/j.cell.2020.01.021.
5. Liu, G., Catacutan, D.B., Rathod, K., Swanson, K., Jin, W., Mohammed, J. C., Chiappino-Pepe, A., Syed, S.A., Fragis, M., Rachwalski, K., et al. (2023). Deep learning-guided discovery of an antibiotic targeting Acinetobacter baumannii. Nat. Chem. Biol. *19*, 1342–1350. https://doi.org/10.1038/s41589-023-01349-8.
6. Zheng, E.J., Valeri, J.A., Andrews, I.W., Krishnan, A., Bandyopadhyay, P., Anahtar, M.N., Herneisen, A., Schulte, F., Linnehan, B., Wong, F., et al. (2024). Discovery of antibiotics that selectively kill metabolically dormant bacteria. Cell Chem. Biol. *31*, 712–728.e9. https://doi.org/10.1016/j.chembiol.2023.10.026.
7. Wong, F., Zheng, E.J., Valeri, J.A., Donghia, N.M., Anahtar, M.N., Omori, S., Li, A., Cubillos-Ruiz, A., Krishnan, A., Jin, W., et al. (2024). Discovery of a structural class of antibiotics with explainable deep learning. Nature *626*, 177–185. https://doi.org/10.1038/s41586-023-06887-8.
8. Anahtar, M.N., Valeri, J.A., Krishnan, A., Donghia, N.M., Palace, S.G., Zheng, E.J., Gulati, A., Jorgenson, A., Junaid, A., Bandyopadhyay, P., et al. (2025) Deep learning-enabled discovery of antibiotics effective against Neisseria gonorrhoeae. In press.
9. Patel, J.S., Norambuena, J., Al-Tameemi, H., Ahn, Y.-M., Perryman, A.L., Wang, X., Daher, S.S., Occi, J., Russo, R., Park, S., et al. (2021). Bayesian Modeling and Intrabacterial Drug Metabolism Applied to Drug-Resistant Staphylococcus aureus. ACS Infect. Dis. *7*, 2508–2521. https://doi.org/10.1021/acsinfecdis.1c00265.
10. Pereira, J.C., Daher, S.S., Zorn, K.M., Sherwood, M., Russo, R., Perryman, A.L., Wang, X., Freundlich, M.J., Ekins, S., and Freundlich, J.S. (2020). Machine Learning Platform to Discover Novel Growth Inhibitors of Neisseria gonorrhoeae. Pharm. Res. *37*, 141. https://doi.org/10.1007/s11095-020-02876-y.
11. Yang, K., Swanson, K., Jin, W., Coley, C., Eiden, P., Gao, H., Guzman-Perez, A., Hopper, T., Kelley, B., Mathea, M., et al. (2019). Analyzing learned molecular representations for property prediction. J. Chem. Inf. Model. *59*, 3370–3388. https://doi.org/10.1021/acs.jcim.9b00237.
12. Wong, F., de la Fuente-Nunez, C., and Collins, J.J. (2023). Leveraging artificial intelligence in the fight against infectious diseases. Science *381*, 164–170. https://doi.org/10.1126/science.adh1114.
13. Enamine. (2023). Enamine REAL Space. https://enamine.net/compound-collections/real-compounds/real-space-navigator.
14. Tingle, B.I., Tang, K.G., Castanon, M., Gutierrez, J.J., Khurelbaatar, M., Dandarchuluun, C., Moroz, Y.S., and Irwin, J.J. (2023). ZINC-22—A Free Multi-Billion-Scale Database of Tangible Compounds for Ligand Discovery. J. Chem. Inf. Model. *63*, 1166–1176. https://doi.org/10.1021/acs.jcim.2c01253.
15. De Cao, N., and Kipf, T. (2018). MolGAN: An implicit generative model for small molecular graphs. Preprint at arXiv. https://doi.org/10.48550/arxiv.1805.11973.
16. Gómez-Bombarelli, R., Wei, J.N., Duvenaud, D., Hernández-Lobato, J.M., Sánchez-Lengeling, B., Sheberla, D., Aguilera-Iparraguirre, J., Hirzel, T.D., Adams, R.P., and Aspuru-Guzik, A. (2018). Automatic Chemical Design Using a Data-Driven Continuous Representation of Molecules. ACS Cent. Sci. *4*, 268–276. https://doi.org/10.1021/acscentsci.7b00572.
17. Jin, W., Barzilay, R., and Jaakkola, T. (2018). Junction Tree Variational Autoencoder for Molecular Graph Generation. Proceedings of the 35th International Conference on Machine Learning *80*, 2323–2332. https://doi.org/10.48550/arxiv.1802.04364.
18. Blaschke, T., Arús-Pous, J., Chen, H., Margreitter, C., Tyrchan, C., Engkvist, O., Papadopoulos, K., and Patronov, A. (2020). REINVENT 2.0: an AI tool for de novo drug design. J. Chem. Inf. Model. *60*, 5918–5922. https://doi.org/10.1021/acs.jcim.0c00915.
19. Zhou, Z., Kearnes, S., Li, L., Zare, R.N., and Riley, P. (2019). Optimization of molecules via deep reinforcement learning. Sci. Rep. *9*, 10752. https://doi.org/10.1038/s41598-019-47148-x.
20. Polishchuk, P. (2020). CReM: chemically reasonable mutations framework for structure generation. J. Cheminform. *12*, 28. https://doi.org/10.1186/s13321-020-00431-w.
21. Xu, M., Yu, L., Song, Y., Shi, C., Ermon, S., and Tang, J. (2022). GeoDiff: a Geometric Diffusion Model for Molecular Conformation Generation. Preprint at arXiv. https://doi.org/10.48550/arxiv.2203.02923.
22. Özçelik, R., Brinkmann, H., Criscuolo, E., and Grisoni, F. (2025). Generative deep learning for de novo drug design-a chemical space odyssey. J. Chem. Inf. Model. *65*, 7352–7372. https://doi.org/10.1021/acs.jcim.5c00641.
23. Cesaro, A., Bagheri, M., Torres, M., Wan, F., and de la Fuente-Nunez, C. (2023). Deep learning tools to accelerate antibiotic discovery. Expert Opin. Drug Discov. *18*, 1245–1257. https://doi.org/10.1080/17460441.2023.2250721.
24. Wan, F., Kontogiorgos-Heintz, D., and de la Fuente-Nunez, C. (2022). Deep generative models for peptide design. Digit. Discov. *1*, 195–208. https://doi.org/10.1039/d1dd00024a.
25. Wan, F., Wong, F., Collins, J.J., and de la Fuente-Nunez, C. (2024). Machine learning for antimicrobial peptide identification and design. Nat. Rev. Bioeng. *2*, 392–407. https://doi.org/10.1038/s44222-024-00152-x.
26. Chen, L., Yu, L., and Gao, L. (2023). Potent antibiotic design via guided search from antibacterial activity evaluations. Bioinformatics *39*, btad059. https://doi.org/10.1093/bioinformatics/btad059.
27. Chen, N., Yang, L., Ding, N., Li, G., Cai, J., An, X., Wang, Z., Qin, J., and Niu, Y. (2022). Recurrent neural network (RNN) model accelerates the development of antibacterial metronidazole derivatives. RSC Adv. *12*, 22893–22901. https://doi.org/10.1039/d2ra01807a.
28. Krishnan, S.R., Bung, N., Padhi, S., Bulusu, G., Misra, P., Pal, M., Oruganti, S., Srinivasan, R., and Roy, A. (2023). De novo design of anti-tuberculosis agents using a structure-based deep learning method. J. Mol. Graph. Model. *118*, 108361. https://doi.org/10.1016/j.jmgm.2022.108361.
29. Zeng, X., Wang, F., Luo, Y., Kang, S.-G., Tang, J., Lightstone, F.C., Fang, E.F., Cornell, W., Nussinov, R., and Cheng, F. (2022). Deep generative molecular design reshapes drug discovery. Cell Rep. Med. *3*, 100794. https://doi.org/10.1016/j.xcrm.2022.100794.
30. Zhavoronkov, A., Ivanenkov, Y.A., Aliper, A., Veselov, M.S., Aladinskiy, V. A., Aladinskaya, A.V., Terentiev, V.A., Polykovskiy, D.A., Kuznetsov, M.D.,

Asadulaev, A., et al. (2019). Deep learning enables rapid identification of potent DDR1 kinase inhibitors. Nat. Biotechnol. *37*, 1038–1040. https://doi.org/10.1038/s41587-019-0224-x.

31. Ren, F., Ding, X., Zheng, M., Korzinkin, M., Cai, X., Zhu, W., Mantsyzov, A., Aliper, A., Aladinskiy, V., Cao, Z., et al. (2023). AlphaFold accelerates artificial intelligence powered drug discovery: efficient discovery of a novel CDK20 small molecule inhibitor. Chem. Sci. *14*, 1443–1452. https://doi.org/10.1039/d2sc05709c.
32. Swanson, K., Liu, G., Catacutan, D.B., Arnold, A., Zou, J., and Stokes, J.M. (2024). Generative AI for designing and validating easily synthesizable and structurally novel antibiotics. Nat. Mach. Intell. *6*, 338–353. https://doi.org/10.1038/s42256-024-00809-7.
33. Erlanson, D.A., McDowell, R.S., and O'Brien, T. (2004). Fragment-based drug discovery. J. Med. Chem. *47*, 3463–3482. https://doi.org/10.1021/jm040031v.
34. Erlanson, D.A., Fesik, S.W., Hubbard, R.E., Jahnke, W., and Jhoti, H. (2016). Twenty years on: the impact of fragments on drug discovery. Nat. Rev. Drug Discov. *15*, 605–619. https://doi.org/10.1038/nrd.2016.109.
35. Babaoglu, K., and Shoichet, B.K. (2006). Deconstructing fragment-based inhibitor discovery. Nat. Chem. Biol. *2*, 720–723. https://doi.org/10.1038/nchembio831.
36. de Souza Neto, L.R., Moreira-Filho, J.T., Neves, B.J., Maidana, R.L.B.R., Guimarães, A.C.R., Furnham, N., Andrade, C.H., and Silva, F.P. (2020). In silico Strategies to Support Fragment-to-Lead Optimization in Drug Discovery. Front. Chem. *8*, 93. https://doi.org/10.3389/fchem.2020.00093.
37. Sams-Dodd, F. (2005). Target-based drug discovery: is something wrong? Drug Discov. Today *10*, 139–147. https://doi.org/10.1016/S1359-6446(04)03316-1.
38. Fink, T., Bruggesser, H., and Reymond, J.-L. (2005). Virtual exploration of the small-molecule chemical universe below 160 Daltons. Angew. Chem. Int. Ed. Engl. *44*, 1504–1508. https://doi.org/10.1002/anie.200462457.
39. Fink, T., and Reymond, J.-L. (2007). Virtual exploration of the chemical universe up to 11 atoms of C, N, O, F: assembly of 26.4 million structures (110.9 million stereoisomers) and analysis for new ring systems, stereochemistry, physicochemical properties, compound classes, and drug discovery. J. Chem. Inf. Model. *47*, 342–353. https://doi.org/10.1021/ci600423u.
40. Blum, L.C., and Reymond, J.-L. (2009). 970 million druglike small molecules for virtual screening in the chemical universe database GDB-13. J. Am. Chem. Soc. *131*, 8732–8733. https://doi.org/10.1021/ja902302h.
41. Ruddigkeit, L., van Deursen, R., Blum, L.C., and Reymond, J.-L. (2012). Enumeration of 166 billion organic small molecules in the chemical universe database GDB-17. J. Chem. Inf. Model. *52*, 2864–2875. https://doi.org/10.1021/ci300415d.
42. Grygorenko, O.O., Radchenko, D.S., Dziuba, I., Chuprina, A., Gubina, K. E., and Moroz, Y.S. (2020). Generating multibillion chemical space of readily accessible screening compounds. iScience *23*, 101681. https://doi.org/10.1016/j.isci.2020.101681.
43. Brenk, R., Schipani, A., James, D., Krasowski, A., Gilbert, I.H., Frearson, J., and Wyatt, P.G. (2008). Lessons learnt from assembling screening libraries for drug discovery for neglected diseases. ChemMedChem *3*, 435–444. https://doi.org/10.1002/cmdc.200700139.
44. Lipinski, C.A., Lombardo, F., Dominy, B.W., and Feeney, P.J. (2001). Experimental and computational approaches to estimate solubility and permeability in drug discovery and development settings. Adv. Drug Deliv. Rev. *46*, 3–26. https://doi.org/10.1016/s0169-409x(00)00129-0.
45. Wong, F., Omori, S., Donghia, N.M., Zheng, E.J., and Collins, J.J. (2023). Discovering small-molecule senolytics with deep neural networks. Nat. Aging *3*, 734–750. https://doi.org/10.1038/s43587-023-00415-z.
46. Jin, W., Barzilay, R., and Jaakkola, T. (2020). Multi-Objective Molecule Generation using Interpretable Substructures. Proceedings of the 37th International Conference on Machine Learning *119*, 4849–4859. https://doi.org/10.48550/arxiv.2002.03244.
47. Mendez, D., Gaulton, A., Bento, A.P., Chambers, J., De Veij, M., Félix, E., Magariños, M.P., Mosquera, J.F., Mutowo, P., Nowotka, M., et al. (2019). ChEMBL: towards direct deposition of bioassay data. Nucleic Acids Res. *47*, D930–D940. https://doi.org/10.1093/nar/gky1075.
48. Ertl, P., and Schuffenhauer, A. (2009). Estimation of synthetic accessibility score of drug-like molecules based on molecular complexity and fragment contributions. J. Cheminform. *1*, 8. https://doi.org/10.1186/1758-2946-1-8.
49. Thakkar, A., Chadimová, V., Bjerrum, E.J., Engkvist, O., and Reymond, J.-L. (2021). Retrosynthetic accessibility score (RAscore) - rapid machine learned synthesizability classification from AI driven retrosynthetic planning. Chem. Sci. *12*, 3339–3349. https://doi.org/10.1039/d0sc05401a.
50. Parrot, M., Tajmouati, H., da Silva, V.B.R., Atwood, B.R., Fourcade, R., Gaston-Mathé, Y., Do Huu, N., and Perron, Q. (2023). Integrating synthetic accessibility with AI-based generative drug design. J. Cheminform. *15*, 83. https://doi.org/10.1186/s13321-023-00742-8.
51. Wildman, S.A., and Crippen, G.M. (1999). Prediction of Physicochemical Parameters by Atomic Contributions. J. Chem. Inf. Comput. Sci. *39*, 868–873. https://doi.org/10.1021/ci990307l.
52. Farha, M.A., Verschoor, C.P., Bowdish, D., and Brown, E.D. (2013). Collapsing the proton motive force to identify synergistic combinations against Staphylococcus aureus. Chem. Biol. *20*, 1168–1178. https://doi.org/10.1016/j.chembiol.2013.07.006.
53. Gaetani, M., Sabatier, P., Saei, A.A., Beusch, C.M., Yang, Z., Lundström, S.L., and Zubarev, R.A. (2019). Proteome Integral Solubility Alteration: A High-Throughput Proteomics Assay for Target Deconvolution. J. Proteome Res. *18*, 4027–4037. https://doi.org/10.1021/acs.jproteome.9b00500.
54. Manioglu, S., Modaresi, S.M., Ritzmann, N., Thoma, J., Overall, S.A., Harms, A., Upert, G., Luther, A., Barnes, A.B., Obrecht, D., et al. (2022). Antibiotic polymyxin arranges lipopolysaccharide into crystalline structures to solidify the bacterial membrane. Nat. Commun. *13*, 6195. https://doi.org/10.1038/s41467-022-33838-0.
55. Vetterli, S.U., Zerbe, K., Müller, M., Urfer, M., Mondal, M., Wang, S.-Y., Moehle, K., Zerbe, O., Vitale, A., Pessi, G., et al. (2018). Thanatin targets the intermembrane protein complex required for lipopolysaccharide transport in Escherichia coli. Sci. Adv. *4*, eaau2634. https://doi.org/10.1126/sciadv.aau2634.
56. Theuretzbacher, U., Blasco, B., Duffey, M., and Piddock, L.J.V. (2023). Unrealized targets in the discovery of antibiotics for Gram-negative bacterial infections. Nat. Rev. Drug Discov. *22*, 957–975. https://doi.org/10.1038/s41573-023-00791-6.
57. Wong, F., Omori, S., Li, A., Krishnan, A., Lach, R.S., Rufo, J., Wilson, M.Z., and Collins, J.J. (2025). An explainable deep learning platform for molecular discovery. Nat. Protoc. *20*, 1020–1056. https://doi.org/10.1038/s41596-024-01084-x.
58. Tu, Z., Choure, S.J., Fong, M.H., Roh, J., Levin, I., Yu, K., Joung, J.F., Morgan, N., Li, S.-C., Sun, X., et al. (2025). ASKCOS: an open source software suite for synthesis planning. Preprint at arXiv. https://doi.org/10.48550/arxiv.2501.01835.
59. Goodfellow, I.J., Pouget-Abadie, J., Mirza, M., Xu, B., Warde-Farley, D., Ozair, S., Courville, A., and Bengio, Y. (2014). Generative Adversarial Nets. Advances in Neural Information Processing Systems. Proceedings of the 27th International Conference on Neural Information Processing Systems 2, 2672–2680.
60. Schwaller, P., Laino, T., Gaudin, T., Bolgar, P., Hunter, C.A., Bekas, C., and Lee, A.A. (2019). Molecular Transformer: A Model for Uncertainty-Calibrated Chemical Reaction Prediction. ACS Cent. Sci. *5*, 1572–1583. https://doi.org/10.1021/acscentsci.9b00576.

61. Bengio, Y., Deleu, T., Hu, E.J., Lahlou, S., Tiwari, M., and Bengio, E. (2023). GFlowNet Foundations. J. Mach. Learn Res. *24*, 1–55. https://doi.org/10.48550/arxiv.2111.09266.
62. Oestreich, M., Merdivan, E., Lee, M., Schultze, J.L., Piraud, M., and Becker, M. (2025). DrugDiff: small molecule diffusion model with flexible guidance towards molecular properties. J. Cheminform. *17*, 23. https://doi.org/10.1186/s13321-025-00965-x.
63. Alakhdar, A., Poczos, B., and Washburn, N. (2024). Diffusion models in de novo drug design. J. Chem. Inf. Model. *64*, 7238–7256. https://doi.org/10.1021/acs.jcim.4c01107.
64. Morehead, A., and Cheng, J. (2024). Geometry-complete diffusion for 3D molecule generation and optimization. Commun. Chem. *7*, 150. https://doi.org/10.1038/s42004-024-01233-z.
65. Imrie, F., Bradley, A.R., van der Schaar, M., and Deane, C.M. (2020). Deep generative models for 3D linker design. J. Chem. Inf. Model. *60*, 1983–1995. https://doi.org/10.1021/acs.jcim.9b01120.
66. Lundberg, S., and Lee, S.-I. (2017). A Unified Approach to Interpreting Model Predictions. Adv. Neural Inf. Process. Syst. *30*. https://doi.org/10.48550/arxiv.1705.07874.
67. Policar, P.G., Strazar, M., and Zupan, B. (2024). openTSNE: A Modular Python Library for t-SNE Dimensionality Reduction and Embedding. J. Stat. Softw. *109*, 1–30. https://doi.org/10.18637/jss.v109.i03.
68. Cutler, K.J., Stringer, C., Lo, T.W., Rappez, L., Stroustrup, N., Brook Peterson, S., Wiggins, P.A., and Mougous, J.D. (2022). Omnipose: a high-precision morphology-independent solution for bacterial cell segmentation. Nat. Methods *19*, 1438–1448. https://doi.org/10.1038/s41592-022-01639-4.
69. CDC. (2018). CDC and FDA Antibiotic Resistance Isolate Bank. https://www.cdc.gov/antimicrobial-resistance/php/public-health-strategy/index.html.
70. Wade, J.J., and Graver, M.A. (2007). A fully defined, clear and protein-free liquid medium permitting dense growth of Neisseria gonorrhoeae from very low inocula. FEMS Microbiol. Lett. *273*, 35–37. https://doi.org/10.1111/j.1574-6968.2007.00776.x.
71. Enamine. (2020). Enamine REAL Fragments database. https://enamine.net/compound-collections/real-compounds/real-database.
72. Ruddigkeit, L., Blum, L.C., and Reymond, J.-L. (2013). Visualization and Virtual Screening of the Chemical Universe Database GDB-17. ,J. Chem. Inf. Model. *53*, 56–65.
73. Papp, J.R., Rowlinson, M.-C., O'Connor, N.P., Wholehan, J., Razeq, J.H., Glennen, A., Ware, D., Iwen, P.C., Lee, L.V., and Hagan, C. (2018). Accuracy and reproducibility of the Etest to detect drug-resistant Neisseria gonorrhoeae to contemporary treatment. J. Med. Microbiol. *67*, 68–73. https://doi.org/10.1099/jmm.0.000651.
74. Foerster, S., Unemo, M., Hathaway, L.J., Low, N., and Althaus, C.L. (2016). Time-kill curve analysis and pharmacodynamic modelling for in vitro evaluation of antimicrobials against Neisseria gonorrhoeae. BMC Microbiol. *16*, 216. https://doi.org/10.1186/s12866-016-0838-9.
75. Ipsen, J.Ø., and Sørensen, D.M. (2022). ATP hydrolytic activity of purified Spf1p correlate with micellar lipid fluidity and is dependent on conserved residues in transmembrane helix M1. PLoS One *17*, e0274908. https://doi.org/10.1371/journal.pone.0274908.
76. Modaresi, S.M., Sugiyama, R., Tram, N.D.T., Jakob, R.P., Phan, C.-S., Saei, A.A., Morishita, Y., Mühlethaler, T., Lim, J., Ritz, D., et al. (2024). Antibiotics that Kill Gram-negative Bacteria by Restructuring the Outer Membrane Protein BamA. Preprint at bioRxiv. https://doi.org/10.1101/2024.12.16.628070.
77. Zhang, X., Lytovchenko, O., Lundström, S.L., Zubarev, R.A., and Gaetani, M. (2022). Proteome integral solubility alteration (PISA) assay in mammalian cells for deep, high-confidence, and high-throughput target deconvolution. Bio Protoc *12*, e4556. https://doi.org/10.21769/BioProtoc.4556.
78. Gaetani, M., and Zubarev, R.A. (2023). Proteome Integral Solubility Alteration (PISA) for High-Throughput Ligand Target Deconvolution with Increased Statistical Significance and Reduced Sample Amount. Methods Mol. Biol. *2554*, 91–106. https://doi.org/10.1007/978-1-0716-2624-5_7.
79. Zhang, X., Lytovchenko, O., Lundström, S.L., Zubarev, R.A., and Gaetani, M. (2022). Proteome Integral Solubility Alteration (PISA) Assay in Mammalian Cells for Deep, High-Confidence, and High-Throughput Target Deconvolution. Bio Protoc. *12*, e4556. https://doi.org/10.21769/BioProtoc.4556.
80. Raterman, E.L., and Jerse, A.E. (2019). Female Mouse Model of Neisseria gonorrhoeae Infection. Methods Mol. Biol. *1997*, 413–429. https://doi.org/10.1007/978-1-4939-9496-0_24.

Please cite this article in press as: Krishnan et al., A generative deep learning approach to *de novo* antibiotic design, Cell (2025), https://doi.org/10.1016/j.cell.2025.07.033

STAR★METHODS

KEY RESOURCES TABLE

REAGENT or RESOURCE	SOURCE	IDENTIFIER
Bacterial and virus strains		
Staphylococcus aureus RN4220 (MSSA)	DSMZ-German Collection of Microorganisms and Cell Cultures GmbH, Leibniz Institute	DSM 26309
Staphylococcus aureus FPR3757 (MRSA)	ATCC - American Type Culture Collection	BAA-1556
Neisseria gonorrhoeae F-18	ATCC	49226
Neisseria gonorrhoeae FA1090	ATCC	700825
Bacillus subtilis 168	ATCC	23857
Escherichia coli BW25113	DSMZ	DSM 27469
Escherichia coli K-12 MG1655	ATCC	700926
Escherichia coli JW5503-KanS (ΔtolC832::FRT)	EC GRC – *E coli* Genetic Resource Center	CGSC: 14206
Escherichia coli RFM795 (*lptD*4213)	EC GRC – *E coli* Genetic Resource Center	CGSC: 14179
Klebsiella pneumoniae NCTC 9633	ATCC	13883
Pseudomonas aeruginosa PAO1	ATCC	47085
Acinetobacter baumannii 5377	ATCC	17978
Mycobacterium tuberculosis H37Ra	ATCC	25177
CDC & FDA Antibiotic Resistance Bank (ARB) isolates	CDC & FDA AR Isolate Bank	https://wwwn.cdc.gov/arisolatebank/; See Table S4 for unique identifiers
Chemicals, peptides, and recombinant proteins		
De novo generated compounds and analogs	This study; synthesized by Enamine Ltd. (Kyiv, Ukraine)	See Data S2
NG1 analogs	CC4CARB (Chemistry Center for Combating Antibiotic-Resistant Bacteria)	See Data S2
Vancomycin	Fisher Scientific	AAJ6279003
Valinomycin	Thermo Fisher	V1644
Triclosan	MilliporeSigma	72779
Azithromycin	Cayman Chemical	15004
Ceftriaxone	Cayman Chemical	18866
Fosfomycin sodium	MilliporeSigma	34089
CCCP (carbonyl cyanide m-chlorophenyl hydrazone)	MedChemExpress	HY-100941
Fusidic acid	MilliporeSigma	F0881
Ciprofloxacin	MilliporeSigma	17850
Kanamycin sulfate	MilliporeSigma	60615
DMSO	MilliporeSigma	D5879
PrestoBlue Cell Viability Reagent	Invitrogen	A13261
Resazurin	MilliporeSigma	R7017
Triton X-100	MilliporeSigma	T8787
$DiSC_3(5)$	Invitrogen	D306
Laurdan	Sigma-Aldrich	40227
NPN (N-phenyl-1-naphthylamine)	Sigma-Aldrich	104043
SYTOX Green	Invitrogen	S7020
TRIzol Reagent	Thermo Fisher	15596026
Chloroform	Sigma-Aldrich	C2432

(*Continued on next page*)

Continued

REAGENT or RESOURCE	SOURCE	IDENTIFIER
FM4-64	Thermo Fisher	T13320
DAPI	Thermo Fisher	D1306
Experimental models: Cell lines		
HEK293	ATCC	CRL-1573
HepG2	ATCC	HB-8065
HSkMC	ATCC	PCS-950-010
IMR90	ATCC	CCL-186
Experimental models: Organisms/strains		
Female C57BL/6J mice	Jackson Laboratory	000664
Female BALB/cJ	Jackson Laboratory	000651
Female ovariectomized BALB/cJ mice	Jackson Laboratory	000651
Software and algorithms		
Chemprop	Yang et al.[11]	https://github.com/chemprop/chemprop
RDKit	RDKit	https://www.rdkit.org
SHAP	Lundberg and Lee[66]	https://github.com/slundberg/shap
openTSNE	Policar et al.[67]	https://opentsne.readthedocs.io
CReM	Polishchuk[20]	https://github.com/DrrDom/crem
F-VAE	Jin et al.[46]	https://github.com/wengong-jin/multiobj-rationale
JT-VAE	Jin et al.[17]	https://github.com/wengong-jin/hgraph2graph
ASKCOS	Tu et al.[58]	https://askcos.mit.edu
GraphPad Prism v10.1.0	GraphPad Software	https://www.graphpad.com
Harmony & Signal Image Artist	PerkinElmer	N/A
Omnipose	Cutler et al.[68]	https://github.com/kevinjohncutler/omnipose
Proteome Discoverer	Thermo Fisher	v3.2
edgeR v4.4.2	Bioconductor	https://bioconductor.org/packages/release/bioc/html/edgeR.html
clusterProfiler v4.10.0	Bioconductor	https://www.bioconductor.org/packages//2.13/bioc/html/clusterProfiler.html
Deposited data		
Code platform for reproducing all analyses in this work	This study	https://github.com/aartikrish/de-novo-antibiotics
Data generated from the computational pipelines (fragment based and *de novo* design)	This study	Zenodo repository: https://doi.org/10.5281/zenodo.15191826
Data generated from experimental chemical screening	Wong et al.[7]; Anahtar et al.[8]	Zenodo repository https://doi.org/10.5281/zenodo.15191826
RNA sequencing data	This study	Zenodo repository https://doi.org/10.5281/zenodo.15191826
Proteomics data	This study	PRIDE ID: PXD063107
Other		
SpectraMax M3 Multi-Mode Microplate Reader	Molecular Devices	N/A
JEM-2100F Field Emission Electron Microscope for Cryo-TEM	JEOL	N/A
Gatan Cryoplunge	Gatan	N/A

(*Continued on next page*)

Please cite this article in press as: Krishnan et al., A generative deep learning approach to *de novo* antibiotic design, Cell (2025), https://doi.org/10.1016/j.cell.2025.07.033

Continued

REAGENT or RESOURCE	SOURCE	IDENTIFIER
Opera Phenix 2 Confocal Microscope for High-Content Screening	PerkinElmer	N/A
Biometra T-GRADIENT thermocycler	Analytik Jena	8464070201
Orbitrap Exploris 480 Mass Spectrometer	Thermo Fisher Scientific	BRE725539
NovaSeq X Plus	Illumina	N/A
Labcyte Echo 555 Acoustic Dispenser	Beckman Coulter	N/A
Qubit 4 Fluorometer	Thermo Fisher	N/A
Direct-zol RNA Miniprep Plus Kit	Zymo Research	R2070
Sep-Pak C18 Column	Waters	N/A
PepMap C18 trap and RSLC nano-LC columns	Thermo Fisher	N/A

EXPERIMENTAL MODEL AND STUDY PARTICIPANT DETAILS

Cell culture

Human cell lines were obtained from ATCC: HEK293 (CRL-1573), HepG2 (HB-8065), HSkMCs (PCS-950-010) and IMR-90 (Institute for Medical Research-90 cell line; CCL-186). HEK293 and HepG2 cells were grown to log phase in high-glucose Dulbecco's Modified Eagle Medium (DMEM; Corning 10-013-CV) supplemented with 10% fetal bovine serum (FBS; ThermoFisher 16140071) and 1% penicillin-streptomycin (ThermoFisher 15070063). HSkMCs were grown in mesenchymal stem cell basal medium for adipose, umbilical and bone marrow-derived MSCs (ATCC: PCS-500-030) supplemented with ATCC's primary skeletal muscle growth kit (ATCC: PCS-950-040) and 1% penicillin-streptomycin. IMR-90 cells were grown in in Eagle's Minimum Essential Medium (EMEM; ATCC 30-2003) supplemented with 10% FBS and 1% penicillin-streptomycin. Cells were cultured at 37°C and 5% CO_2 in humidity-controlled incubators and passaged <5-10 times. All cell lines were authenticated by the supplier, ATCC, using STR profiling.

Bacterial cell culture

The main bacterial strains used in this study include methicillin-susceptible *Staphylococcus aureus* RN4220 (MSSA DSM 26309; DSMZ German Collection of Microorganisms and Cell Cultures, Leibniz Institute), methicillin-resistant *Staphylococcus aureus* FPR3757 (MRSA USA300; ATCC BAA-1556), and *Neisseria gonorrhoeae* (ATCC 49226). Other common strains include *N. gonorrhoeae* FA 1090 (ATCC 700825), *Bacillus subtilis* 168 (ATCC 23857), *Escherichia coli* BW25113 (DSMZ 27469), MG1655 (ATCC 700926), JW5503-KanS (Δ*tolC*832::FRT, CGSC 14206), and RFM795 (lptD4213) (CGSC 14179), *Klebsiella pneumoniae* (ATCC 13883), *Pseudomonas aeruginosa* PAO1 (ATCC 47085), *Acinetobacter baumannii* (ATCC 17978) and *Mycobacterium tuberculosis* MTB H37Ra (ATCC 25177). Additional bacterial isolates in Table S4 were obtained from the CDC & FDA Antibiotic Resistance (AR) Isolate Bank (Atlanta, Georgia).[69] All bacterial strains were authenticated by their respective suppliers: ATCC, DSMZ and/or CDC, using next-generation sequencing or Sanger sequencing. Unless specified, LB medium containing 1.5% Difco agar (Becton Dickinson 244520) was used to grow individual colonies. Cells were grown in liquid LB (Becton Dickinson 244620) from single colonies aerobically in 14 mL Falcon tubes using 2-3 mL working volumes without antibiotic selection. The cultures were incubated at 37 °C in a light-insulated, humidity-controlled chamber, shaking at 300 rpm. All *Neisseria* strains were passaged twice on chocolate agar plates (CAP; Hardy Diagnostics, H25). Several colonies were picked from plates to obtain a desired OD_{600} and grown in specialized Graver Wade media[70] at 37°C with 5% CO_2 in a humidity-controlled incubator.

Mouse models

All animal studies were performed at the Wyss Institute at Harvard in accordance with protocol IS00000852-6, approved by the Harvard Medical School Institutional Animal Care and Use Committee and the Committee on Microbiological Safety. All mice were all purchased from Jackson Laboratory and housed in pathogen-free facility maintained at 20-26ºC ambient temperature, 40-65% relative humidity, and a 12:12 light-dark cycle. Enrichment devices were included in the animal environments as required and changed biweekly. For **NG1**, female BALB/c mice had a 1 week acclimation period to the mouse facility prior to testing the toxicity (healthy; 6–8 weeks old, 20 ± 2 g) and efficacy (healthy; ovariectomized at Jackson Laboratory, 23 ± 3 g). None of the mice had been involved in previous procedures. For **DN1**, female C57BL/6J mice had a 48-hour acclimation period upon arrival to the mouse facility prior to testing the toxicity (healthy; 6-12 weeks old, weight of 22 ± 2 g) and efficacy (rendered neutropenic with cyclophosphamide on Day -4 and Day -1; 19 ± 2 g).

Please cite this article in press as: Krishnan et al., A generative deep learning approach to *de novo* antibiotic design, Cell (2025), https://doi.org/10.1016/j.cell.2025.07.033

METHOD DETAILS

Computational methods

Machine learning models

Chemprop[11] is a software package that implements directed message-passing neural networks (D-MPNNs). Here, these models are trained on binarized data representing the empirical growth inhibitory activity of compounds. As described previously,[11] D-MPNNs, which are a form of graph neural networks (GNNs), take as input a simplified molecular-input line-entry system (SMILES) string of a compound and convert it to a molecular graph representation. Graph convolutional operations are applied to each atom and bond, and information from local substructures of the compound are aggregated. An intermediate vector representation is generated by collapsing the information associated with each bond and atom into a single embedding. This embedding is then concatenated to a list of global biophysical features, such as molecular weight, which are used to potentially improve the predictions made, and the output is then passed to a fully-connected feed-forward neural network. The output of each trained model is a score between 0 and 1, representing the probability that the input molecule is antibacterial (0: does not inhibit bacterial growth and 1: inhibits bacterial growth). The output of an ensemble was taken as the average of all models in the ensemble.

In this work, ensembles of 20 binary classification Chemprop models for two bacterial species, *N. gonorrhoeae* and *S. aureus*, were trained on 38,765 and 39,312 compounds (as described in detail in Anahtar et al.[8] and Wong et al.[7]), respectively. Training datasets containing the experimentally-determined inhibitory activity of each compound are available in Anahtar et al.[8] and Wong et al.[7] Hyperparameter optimization was performed, and each ensemble was previously benchmarked.[7,8] Chemprop models predicting cytotoxicity against human cells were previously developed and described in Wong et al.[7]; in this work, we use these models to predict the cytotoxicity of a given fragment or compound against human hepatocellular carcinoma (HepG2), human skeletal muscle cells (HSkMCs), and human lung fibroblasts (IMR-90). The output of these models is a score between 0 and 1, describing the probability that the inputted compound is cytotoxic (0: non-toxic and 1: toxic).

SHAP analysis of molecular feature importance

Model setup and background data

A SHAP (SHapley Additive exPlanations) analysis was conducted to quantify the contribution of 2D RDKit-derived descriptors (200 features) to antibacterial activity predictions. Features were stored in .npz format, and background data comprised the first 100 compounds from the dataset. Data were split into 240 equal-sized chunks to enable parallel execution across a high-performance computing (HPC) cluster.

SHAP feature attribution for antibacterial activity models

To interpret the contribution of molecular descriptors to model predictions, we applied SHAP analysis to neural network models trained to predict antibacterial activity from RDKit-derived 2D chemical features. Separate SHAP analyses were performed for models trained on *N. gonorrhoeae* and *S. aureus*, each using the same set of 200 standardized descriptors as model input. SHAP values were computed using a model-agnostic approach with the shap.Explainer class, where predictions were generated via a custom wrapper around the Chemprop command-line interface. This wrapper accepted NumPy arrays of feature vectors, saved them to temporary files compatible with Chemprop, and invoked model inference using subprocess calls. A background set of 100 representative molecules was used to approximate conditional expectations for feature ablation. To parallelize SHAP computations, the full dataset was divided into 240 chunks and processed independently across a CPU-based HPC cluster. For each chunk, SHAP values were computed and saved as serialized objects. After completion, all chunks were aggregated into a single SHAP explanation object per species. We calculated global feature importance by taking the mean absolute SHAP value across all molecules for each descriptor. The top 10 most influential features were visualized in SHAP summary plots, annotated with short chemical descriptions and colored by feature value. All 200 features were also exported to a CSV file reporting their names, descriptive annotations, and mean SHAP contributions. These results enabled identification of key structural and physicochemical properties associated with antibacterial activity across species-specific models. SHAP analysis was performed in Python 3.10 on CPU nodes on the high performance computing cluster. Predictions were generated using the Chemprop CLI (version 1.6.1). RDKit (version 2024.3.6) was used for descriptor generation. All scripts utilized shap, matplotlib, numpy, and pandas for computation and visualization.

Species specificity of Chemprop models

To examine the species specificity of the different models for *N. gonorrhoeae* and *S. aureus*, our original training data that were empirically tested against both species were split into a training set (80%) and test set (20%). Both *N. gonorrhoeae*- and *S. aureus*-specific models were re-trained and the mean predicted scores were compared with the antibacterial activity of the test set. Compounds with high mean scores against one species demonstrated selective activity against that species, and compounds with high (or low) mean scores against both species demonstrated activity (inactivity) against both species.

Fragment and compound libraries

A fragment library comprising 45,858,026 fragments was assembled from the Generated DataBase (GDB, courtesy of Dr. Jean-Louis Reymond at the University of Bern, Switzerland) and the Readily AccessibLe (REAL) fragment database from Enamine.[71] The GDB libraries enumerate all theoretically-possible fragments up to a prespecified number of atoms following simple chemical stability and synthetic feasibility rules.[72] To compile a set of 11-atom fragments including C, N, O, F, Cl, and S atoms, we combined the entire GDB-11[39] (fragments up to 11 atoms including C, N, O, and F atoms, N = 26,434,571) and all up-to-11-atom fragments in the

GDB-13[40] (which includes C, N, O, Cl, and S atoms, *N* = 1,089,000). Enamine fragments (version October 5, 2022, *N* = 18,338,026) were obtained from the Enamine REAL database.

To experimentally assess chemically diverse compounds containing the above fragments, as well as to search for analogs, we assembled a database from two large purchasable libraries: 799,149 compounds from the Broad Institute and 6,138,200 commercially available compounds from MolPort, MayBridge, and Ambinter.

Identification and selection of fragments and compounds associated with antibiotic activity

All 45,858,026 fragments, containing readily-accessible fragments from the Enamine REAL Fragment database, were scored using the trained *N. gonorrhoeae*[8] and *S. aureus* ensemble[7] models, as described above. All 6,937,349 compounds were scored using both *N. gonorrhoeae* and *S. aureus* ensembles. For the analysis shown in Figure S1A, three fragments representative of known antibiotics were encoded using the following SMILES strings: nitrofuran: 'O=[N+](O)c1ccco1'; fluoroquinolone: 'O=C(O)c2c[nH]c1ccc(F)cc1c2=O'; and carbapenem: 'O=C(O)C1=CCC2CC(=O)N12'. Compounds containing these moieties were identified in a manually-compiled set of 559 known antibiotics and antiseptics[6] (Data S1). Compounds containing the fragments were identified using RDKit's HasSubstructMatch function, and the known antibacterial compounds were subsequently scored using either the *N. gonorrhoeae* or *S. aureus* ensembles. We found that the prediction scores for compounds correlated with the prediction scores of the fragment alone (Figure S1A), supporting the performance of an algorithm that identifies fragments with high predictive scores for the discovery and design of selective antibacterial compounds.

As detailed in the main text, our approach to fragment selection and compound testing involved the following steps. For each of *N. gonorrhoeae* and *S. aureus*, fragments with antibiotic activity prediction scores > 0.05 or > 0.1 were retained in the GDB and REAL libraries, respectively. Of these fragments, those with cytotoxicity prediction scores < 0.5 across all three human cell types (HepG2, HSkMC, and IMR90) were retained. Fragments were then tested for the presence of PAINS or Brenk substructures using RDKit's FilterCatalogParams.FilterCatalogs.PAINS and FilterCatalogParams.FilterCatalogs.BRENK built-in structure lists, respectively. To focus on structurally novel fragments, only fragments with maximum Tanimoto similarity < 0.5 with respect to the aforementioned set of 559 known antibiotics were retained. Here, Tanimoto similarity was calculated using Morgan fingerprints, with radius equal to 2 and number of bits equal to 2048. The remaining fragments were matched to compounds using RDKit's HasSubstructMatch function. Matched compounds were considered if they had an antibacterial activity prediction score > 0.1, and matched compounds were filtered in the same way for cytotoxicity and structural novelty as described for fragments above (GitHub repository, see data and code availability).

De novo design of compounds with generative models

CReM: chemically reasonable mutations framework

For the genetic algorithm based on F-CReM described in this work, a modified version of CReM[20] was implemented. For each run of the algorithm, the SMILES string of a fragment and molecule containing the fragment was provided as input; the former was provided in order to ensure that all generated compounds possessed the fragment using RDKit's HasSubstructMatch() function, and the latter was provided as a seed. For *de novo* design of molecules based on CReM, the SMILES string of either ammonia, methane, or water was provided as input.

By default, CReM provides two methods: 'grow' and 'mutate' (as implemented in the CReM Python package). Ranges for parameter combinations were provided as additional input. Parameter combinations for grow algorithms included max_atom (4, 6, 8, and 10 were used), min_atom (0 was used), and radius (2 and 3 were used), while the parameter combinations for mutate algorithms included the max_size (4, 6, 8, and 10 were used), min_size (0 was used), radius (2 and 3 were used), min_inc (-2 was used), and max_inc (2 was used). All possible combinations of these parameters were considered using a full grid search. For a given parameter set, the algorithm proceeded as follows:

(i) The original molecule was used to generate *de novo* molecules with either the grow or mutate function from CReM, and molecules that did not contain the original fragment were discarded.
(ii) Compounds containing PAINS and Brenk substructures were excluded.
(iii) Chemprop scores for the resulting molecules were calculated using either the *S. aureus* or *N. gonorrhoeae* ensemble.
(iv) If the user-defined scoring method was set to 'regular score', then the compounds were ranked according to the Chemprop models (*chempropsco*). If not, modified scores that incorporate additional criteria were calculated. The additional criteria included the following variables: *SAScore* (predicted synthesizability score), *tansim* (Tanimoto similarity to known antibiotics), *hepg2* (predicted toxicity score for HepG2 cells), and *prim* (predicted toxicity score for HSkMC cells). To improve speed, prediction scores from the IMR-90 cytotoxicity ensemble were not considered as additional variables here, but all generated compounds were eventually filtered based on cytotoxicity prediction scores from all three cytotoxicity ensembles (as described in *Down-selection of generated compounds for synthesis and testing* below). Modified scores (*adj_score*) were calculated based on the original score (*chempropsco*) and the additional variables according to the formula:

$adj\_score = (2.0 * chempropsco) - ((sascore / 10.0) + tansim + hepg2 + prim)$.

(v) Finally, to seed the next iteration of the algorithm, we calculated the number of compounds generated and scored in steps (i)-(iv) above (N_{gen}) and compared it to the sum of two prespecified numbers, N_{top} and N_{rand}. If max_atom_range ≥ 8, then $N_{top} = 2$ and $N_{rand} = 1$; else $N_{top} = 5$ and $N_{rand} = 5$. If $N_{gen} \leq N_{top} + N_{rand}$, then all N_{gen} compounds were used to seed the next iteration.

Otherwise, the N_{top} highest-scoring compounds among the N_{gen} generated compounds, as well as N_{rand} other randomly chosen compounds among the N_{gen} generated compounds were used to seed the next iteration.

Fragment-based Variational Autoencoder (F-VAE)

The F-VAE described in the main text was inspired by fragment-based drug discovery strategies often used by medicinal chemists. The algorithm starts with fragments associated with specific properties of interest (e.g., antibacterial activity) and expands these fragments into molecules. In particular, our rationale-conditioned molecular graph generator is a variational autoencoder which completes a full molecule, G, given a fragment, S. Since each fragment (S) may be realized into many different molecules, we introduce a latent variable, z, to generate diverse outputs:

$$P(G|S) = \int_z P(G|S,z)P(z)dz,$$

where $P(z)$ is the prior distribution. The F-VAE model consists of a graph encoder and a graph decoder. In this case, the encoder is a message passing neural network (MPNN) which learns the approximate posterior for variational inference. In the graphical representation of each molecule, each atom or bond is represented by a one-hot encoding of its atom or bond type. The encoder then uses three message-passing layers, followed by an average pooling operation, to transform the initial graph representation into a 20-dimensional latent vector, z_G.

The decoder then generates a molecule (a molecular graph) according to its breadth-first order. In each step, the model generates a new atom and all its connecting edges. During generation, we maintained a queue that contained frontier nodes in the graph with neighbors to be generated. Let G_t be the partial graph generated by step t. To ensure that the full molecule, G, contains S as a subgraph, we set the initial state of $G_0 = S$ and put all the leaf atoms (atoms with degree = 1 in the graph) in the queue. In each generation step, the decoder first runs an MPNN over the current graph to compute an atom representation, h_v, for each atom, v. Suppose that the first atom in the queue is v. The decoder then expands the current molecule using three decision steps:

1. Predict whether there will be a new atom attached to v. The probability of this expansion step is predicted based on the latent vector, z_G, and atom representation of v: $p_v = \mathrm{sigmoid}(\mathrm{MLP}(\mathrm{h_v}, \mathrm{z_G}))$.
2. If $p_v > 0.5$, discard v and move on to the next node in the queue. Otherwise, create a new atom, u, predict its atom type, and append it to the queue.
3. Predict the bond type between u and other leaf nodes in the queue. Since atoms are generated in breadth-first order, there are no bonds between u and atoms not in the queue. To fully capture edge dependencies, we predict the bonds between u and atoms in the queue sequentially, and we update the representation of u when new bonds are added to the molecule.

The F-VAE was pre-trained on 1,686,695 molecules from ChEMBL (version 22) to enable the model to generate realistic molecules. Each training example was a pair, (S, G), where S is a random connected subgraph of a molecule G with up to 15 atoms. We trained the generative model to maximize the likelihood of the ground truth molecule G given fragment S, using the following hyperparameters: hidden_size = 400, batch_size = 16, MPNN depth = 3, learning rate = 1e-3, optimizer = Adam, and epoch = 20.

Junction Tree Variational Autoencoder (JT-VAE)

The JT-VAE described in the main text is a deep generative model designed to generate a molecule without a starting fragment. It represents a molecule at two different levels: an atom graph that represents how atoms are connected to each other and a junction tree that captures how chemical motifs are connected to each other. The model consists of an encoder that maps a molecular graph and a junction tree to a latent representation and a decoder that reconstructs a molecule by sequentially assembling chemical substructures based on the learned junction tree structure. The encoder of JT-VAE is a hierarchical MPNN with three layers.

1. Motif layer: This layer represents how the motifs are coarsely connected in the graph. This layer provides essential information for the motif prediction in the decoding process.
2. Attachment layer: This layer encodes the connectivity between motifs at a fine-grained level, highlighting the attachment points between two chemical motifs.
3. Atom layer: The atom layer is a molecular graph representing how its atoms are connected, where each node represents an atom, and each edge represents a bond.

The decoder generates a molecule motif by motif according to their depth-first order, using the information encoded by the latent representation. In each generation step, the decoder expands the current molecule based on two predictions:

1. Motif Prediction: The model predicts the next motif to be attached to the current graph.
2. Attachment Prediction: Next, the model needs to predict the attachment configuration between the newly selected motif and the current graph.

The above three predictions together give an autoregressive factorization of the distribution over the next motif and its attachment. We trained JT-VAE on 1,686,695 drug-like compounds from the ChEMBL database, the same training set as F-VAE. We trained the

Please cite this article in press as: Krishnan et al., A generative deep learning approach to *de novo* antibiotic design, Cell (2025), https://doi.org/10.1016/j.cell.2025.07.033

generative model to maximize the likelihood of the molecules in the training set. The model hyperparameters are as follows: hidden_size = 400, batch_size = 16, MPNN depth = 3, learning rate = 1e-3, optimizer = Adam, and epoch = 20. By sampling from JT-VAE latent space 40 million times, we generated 28,534,490 unique molecules and ranked them based on their predicted antibacterial properties.

Down-selection of generated compounds for synthesis and testing

All compounds were down-selected based on (i) de-duplication of SMILES, (ii) predicted antibacterial score, (iii) maximum Tanimoto similarity with respect to the set of known antibiotics as well as all active antibacterial compounds in the respective training set, (iv) synthesizability score (SAscore[48] or RAscore[49]), and (v) predicted HepG2 and/or HSkMC cytotoxicity score. Both SAscore and RAscore were used only to sample different synthetic accessibility scoring approaches.

For fragments F1, F2 and F2', F-CReM compounds were down selected using predicted antibacterial score > 0.7, SAScore < 3, Tanimoto similarity < 0.5, and HepG2 and HSkMC cytotoxicity score < 0.2. Compounds that contained a β-lactam motif, as defined by those returning True using HasSubstructMatch() with the molecule described by 'O=C1CCN1', were additionally filtered out to preserve structural novelty. For fragments F1, F2 and F2', F-VAE generated-compounds were filtered using predicted antibacterial score > 0.3, RAScore > 0.8, Tanimoto similarity < 0.4, and HepG2 cytotoxicity score < 0.2.

Visualization with t-SNE

t-SNE plots were generated using openTSNE's TSNE() function with perplexity 45, Euclidean distance as the metric, and PCA initialization. Molecules were represented as RDKit fingerprints with min_path=1, max_path=7, n_bits=2048.

ASKCOS retrosynthesis planning tool

The Monte Carlo tree search retrosynthesis model in ASKCOS[58] was used to generate retrosynthetic pathways to each compound. The retrosynthetic search was run on nodes with four CPUs with an expansion time of 60 seconds, a branching factor of 25, and a maximum depth of 6. All other search parameters were set to ASKCOS defaults. We consider the search successful if ASKCOS identified at least one retrosynthetic path from the target compound to purchasable compounds.

Experimental methods

Chemical compounds

Compounds with high purity (>90%) were procured either from the Broad Institute Center for the Development of Therapeutics (CDoT) or from commercial chemical vendors including BIONET-Key Organics Ltd.(Cornwall, UK), ChemBridge (San Diego, CA), ChemDiv (San Diego, CA), Maybridge (Altrincham, UK), MedChemExpress (Monmouth Junction, NJ), TargetMol (Boston, MA), Vitas-M (Hong Kong, China), and Enamine (Kyiv, Ukraine). Stock solutions and serial dilutions of all compounds were freshly prepared in dimethyl sulfoxide (DMSO; MilliporeSigma D5879), unless stated otherwise. Known antibiotics were obtained as follows: vancomycin (Fisher Scientific AAJ6279003), valinomycin (Thermo Fisher, V1644), triclosan (MilliporeSigma, 72779), azithromycin (Cayman Chemical, 15004), ceftriaxone (sodium salt hydrate, Cayman Chemical, 18866), fosfomycin sodium (MilliporeSigma, 34089), CCCP (carbonyl cyanide m-chlorophenyl hydrazone; MedChemExpress, HY-100941), and fusidic acid (Millipore Sigma F0881), all dissolved in DMSO. Kanamycin sulfate (MilliporeSigma, 60615) was dissolved in ultrapure MilliQ-water and ciprofloxacin powder (MilliporeSigma 17850) was dissolved in dilute acid (0.1 M HCl). *De novo* generated compounds, and their respective analogs were synthesized and procured from Enamine (Kyiv, Ukraine). Analogs of compounds containing fragment F1 (**NG1 analogs**) were designed and synthesized by CC4CARB (Chemistry Center for Combating Antibiotic-Resistant Bacteria), an NIAID-led (National Institute of Allergy and Infectious Diseases) partnership with RTI (Research Triangle Institute).

MIC, MBC, and bacterial growth inhibition assays

For *S. aureus*, a bacterial suspension of $\sim 10^5$ CFU/mL was obtained either by performing a 1:10,000 dilution of an overnight culture, picked from a single colony, or a 1:500 dilution of an OD_{600} 0.08 suspension in fresh LB (Becton Dickinson 244620). Cells were seeded in a 96-well plate, with 99 μL of bacteria and one μL of two-fold serially diluted compound in DMSO. Plates were sealed with breathable membranes (Millipore Sigma Z763624) and incubated for 18-24 hours at 37°C with 5% CO_2. The MIC was determined as the minimum concentration for which $OD_{600} < 0.1$, as measured using a SpectraMax M3 plate reader. For initial screening experiments, active compounds were determined as those for which $OD_{600} < 0.15$. For calculating the MBC (maximum bactericidal concentration), overnight treated cells were removed from incubation and serially diluted 10-fold in room temperature LB. Five μL was spotted on LB agar plates and allowed to dry at room temperature before stationary incubation at 37 °C overnight for 16 to 24 h. CFUs were determined by manual counting, and all measurements are based on counts containing at least six colonies.

For *N. gonorrhoeae*, MICs were determined via broth microdilution when screening compounds, via agar dilution when confirming values for a given candidate small molecule (e.g., **NG1**), or via ETEST when testing a standard-of-care antibiotic, per CLSI M100 and M07 guidelines. Prior to MIC testing, frozen stocks were passaged twice on chocolate agar plates (CAP; Hardy Diagnostics, H25). *N. gonorrhoeae* broth microdilution was performed by first preparing the bacterial inoculum by picking individual colonies from an overnight CAP, suspending in PBS to OD_{600} 0.08, and diluting the suspension 1:200 in Graver Wade media.[70] Within 15 minutes of inoculum preparation, each well of a 96- or 384-well plate was inoculated with bacteria and compound (serially diluted in DMSO) such that the final DMSO concentration in each well was $\leq 1\%$ and bacterial concentration was $\sim 5 \times 10^5$ CFU/mL. Plates were incubated at 36-37°C with 5% CO_2 for 20-24 hours. The MIC was determined as the concentration of compound resulting in complete inhibition of growth both visually and as measured by PrestoBlue HS Cell Viability Reagent (Invitrogen) after 1-2 hours of incubation. *N. gonorrhoeae* agar dilution was performed for candidate small molecules by first preparing agar dilution plates following CLSI M07 guidelines. Briefly, serial dilutions of 100× compound stock solutions were made in DMSO and added to molten agar, made of gonococcal (GC) medium base (BD Difco 228950) with 1% IsovitaleX Enrichment (BD 211876), which had been equilibrated to 45-50°C in a water bath. The agar and compound solution were mixed thoroughly and poured into a 6-well plate and allowed to solidify at room temperature. A DMSO-only growth control was included with every dilution series. Plates were used immediately or stored in sealed plastic bags at 4°C for up to a week and allowed to equilibrate to room temperature before use. The bacterial inoculum was prepared by making a 1:10 dilution of a 0.5 McFarland standardized inoculum of each bacterial strain in sterile saline and inoculating 2 μL of the suspension onto each marked location of a plate. The inoculated plates were allowed to dry and incubated at 36-37°C with 5% CO_2 for 16-20 hours while inverted. MICs were read on a dark surface, with growth on the growth control plate required for validity. *Neisseria gonorrhoeae* ETESTs (bioMérieux) were performed as described previously.[73] Briefly, a sterile swab was soaked in a 0.5 McFarland standard bacterial suspension, excess fluid was removed, and the swab was used to evenly cover the entire surface of a plate of GC agar base with 1% IsoVitaleX. The plate was allowed to completely dry before placing an ETEST with sterile forceps, incubating for 18-24 hours at 37°C with 5% CO_2, and reading the MIC as the lowest antibiotic concentration that inhibited growth.

For *M. tuberculosis*, 100 μL of exponentially growing bacteria was seeded at a density of 5×10^4 cells per well in 7H9 supplemented with ADS (albumin dextrose saline), incubated with drug for 5 days at 37°C, then incubated for another 24 hours with 15 μL of 0.02% resazurin (w/v), and fluorescence was read with a SpectraMax M3 plate reader (Ex = 530 nm, Em = 590 nm).

For other species not previously specified, an OD_{600} 0.08 suspension was made in PBS and diluted 1:500 in fresh LB or Haemophilus Test Medium Broth (Remel) for *Haemophilus*. Each well of a 96-well plate received 99 μL of the bacterial suspension and 1 μL of compound. Plates were incubated at 37°C in ambient conditions, except for *Haemophilus* (5% CO_2), for 18-24 hours and MICs were read visually and confirmed by measuring OD_{600} values. All assays were performed in biological duplicates.

Bacterial time-kill assays

For MSSA RN4220, cells were diluted 1:10,000 from an overnight culture into fresh LB and plated into 96-well flat-bottom clear plates using 99 μL working volumes. Plates were then sealed with breathable membranes, and cells were grown to early exponential phase, $OD_{600} \sim 0.01$ (corresponding to $\sim 10^6$ CFU/mL) in a 37°C incubator with shaking at 300 rpm. One μL of compound in two-fold serial dilutions in DMSO was then added to each well to the final concentrations indicated, and bacterial cell cultures were sealed and re-incubated at 37°C with shaking at 300 rpm. At indicated times, cells were removed from incubation, serially diluted in room-temperature LB, and spotted on LB agar (Becton Dickinson 244520) in rectangular plates. Plated cells on LB agar were allowed to dry at room temperature before stationary incubation at 37°C overnight (18-24 hours). CFUs counts were manually determined. For *N. gonorrhoeae*, time-kill assays were performed as previously described.[74] Specifically, a 0.5 McFarland suspension was prepared in sterile PBS using individual colonies picked from chocolate agar plates that had been grown for 18-20 hours at 37°C in a humid 5% CO_2-enriched atmosphere. The suspension was diluted 1:500 in pre-warmed (37°C) GW media and 90 μL was added to each well in a round-bottom 96-well plate. The plate was pre-incubated for 4 hours with shaking at 150 rpm in a 35°C, 5% CO_2-enriched incubator. At time 0, 10 μL of PBS (growth control) or antimicrobial (to achieve a final concentration of 0.5×, 1×, 2×, or 4× MIC, where the MIC of **NG1** was 0.5 μg/mL and azithromycin MIC was 0.25 μg/mL) was added to each well of pre-incubated bacteria in duplicate, with a separate row for each time point. At indicated times, the corresponding row of cells was removed from incubation, serially diluted in PBS, and spotted on GC agar in rectangular plates. After drying at room temperature, plates were incubated overnight (18-24 hours) without shaking and CFU counts were manually determined.

Cytotoxicity assay and CC_{50} determination

A resazurin-based assay, which quantifies the number of live cells in a sample, was used to monitor human cell viability in the presence of a compound. For CC_{50} determination, 99 μL cells were plated into 96-well clear flat-bottom black tissue-culture-treated plates (Corning 3603) at a density of 10^4 cells/well and incubated at 37°C with 5% CO_2. Twenty-four hours after plating, each well received 1 μL of two-fold serially-diluted test compound. Additional wells were treated with 1 μL of DMSO as a negative control and Triton X-100 (0.1% final concentration) as a positive control. Cells treated with the compound were re-incubated for 24 hours, after which 0.15 mM resazurin (Millipore Sigma R7017) was added to each well. After an additional 24 hours of incubation, the fluorescence was read at excitation/emission at 550/590 nm using a SpectraMax M3 plate reader. CC_{50} values were calculated by normalizing the fluorescence values based on the positive and negative controls and performing a nonlinear fit with the [Inhibitor] vs. response – Variable slope function in GraphPad Prism (v.10.1.0). HepG2 and HEK293 CC_{50} values for BRD1 and BRD2 were determined as above, except in 384-well plates seeded with 4500 viable cells/well, where cells were treated with 1 μL (for HepG2) or 500 nL (for HEK293) of compound that were transferred using an acoustic dispenser (Labcyte Echo 555). All experiments were performed in biological duplicate.

Spontaneous mutant generation and frequency of resistance experiments

N. gonorrhoeae. Isolated colonies of *N. gonorrhoeae* ATCC 49226 were picked from an overnight plate to make a heavy suspension in PBS. The suspension was serially diluted and plated on chocolate agar to determine the initial inoculum, and 500 μL of the suspension was added to each GC agar plate containing 0, 1×, 2×, 4×, or 8× MIC of **NG1**. The suspension was spread and allowed to dry before stationary incubation at 37°C in a 5% CO_2 incubator for 3 days. Colonies that emerged on each plate were individually picked and the elevated **NG1** MIC was confirmed using both agar dilution and broth microdilution methods in parallel with the parental strain for comparison. The frequency of resistance was calculated as the total number of colonies counted divided by the total number of bacteria inoculated on each plate.

Please cite this article in press as: Krishnan et al., A generative deep learning approach to *de novo* antibiotic design, Cell (2025), https://doi.org/10.1016/j.cell.2025.07.033

S. aureus. MSSA RN4220 was picked from single colonies and grown overnight in 2 mL of fresh LB. OD_{600} was measured and the suspension was serially diluted and plated on solid agar (with no compound) to determine the initial inoculum. One mL of the same overnight culture (~10^9 CFU) was aliquoted and centrifuged at 3700 × *g* for 5 min. The cell pellet was resuspended to a final volume of 500 μL in fresh LB, then pipetted onto the surface of LB agar plates containing 1×, 2×, 4× or 8× agar MIC of **DN1** (4 μg/mL). Cells were then spread using a bent, sterile inoculating loop, and plates were dried and inverted before stationary overnight incubation at 37°C. The next day, plates were removed from incubation, and colonies that grew on each plate were counted to calculate the frequency of resistance as above.

DiSC$_3$(5) fluorescence

Individual colonies of *S. aureus* RN4220 were picked and grown in 2 mL liquid LB overnight at 37°C with shaking at 300 rpm. Cells were diluted 1:100 from the overnight cultures into liquid LB and grown to mid-log phase, OD_{600} ~0.5, at 37°C with shaking at 300 rpm. For *N. gonorrhoeae*, multiple colonies from the overnight CAP were resuspended in prewarmed Graver Wade media to achieve OD_{600} ~0.5. DiSC$_3$(5) (Invitrogen D306) was dissolved in DMSO and added to liquid cultures at a final concentration of 1 μM. After additional incubation in the presence of DiSC$_3$(5) for 1 to 2 h, cells were plated in 200 μL working volumes in black, opaque flat-bottom 96-well plates, after which fluorescence was measured every 30 seconds for 5 minutes at an excitation/emission of 622/670 nm using a SpectraMax M3 plate reader. Cells were either untreated or treated with DMSO (1%), **NG1**, **DN1**, and **DN1 analogs** at a final concentration of 10 μg/mL (10× MIC). Other control antibiotics were also tested at 10× MIC. Fluorescence was measured immediately following treatment according to the same specifications as above.

Laurdan membrane fluidity assay

An OD_{600} of 0.5 cell suspension of either *N. gonorrhoeae* ATCC 49226 in Graver Wade media or *S. aureus* RN4220 in LB was prepared. As previously described,[6] a solution of 1 mM Laurdan (Sigma-Aldrich 40227) was prepared in 100% DMF (Sigma-Aldrich PHR1553) and stored in the dark at -20°C. Then, 100 μL of the 1 mM Laurdan stock was added to the cell suspension and incubated for 10 minutes at 37°C with shaking at 300 rpm while covered with aluminum foil. The cells were then centrifuged at 4,000 rpm for 5 minutes and washed three times in 10 mL of PBS with 0.2% (w/v) glucose. Cells were then resuspended in 10 mL of the same solution and distributed into a single 96-well opaque flat-bottom plate (Costar Black Polystyrene Plate, 266) with 100 μL per well and 198 μL in column 1. Two μL of **NG1**, **NG1 analog,** or **DN1**, starting at 128 μg/mL, was added to column 1, and serially diluted across columns 2-12 to obtain a final total volume of 100 μL in each well. To the control wells, Tween-20 (Sigma-Aldrich 655204), a known membrane fluidizer[75] starting at a concentration of 0.5% was added. Untreated or DMSO treated (1%) cells served as the negative control and triclosan (starting at 62.5 μg/mL) and azithromycin (starting at 250 μg/mL) were included as positive or neutral antibiotic controls. A kinetic read was taken every 45 seconds at 37°C using a SpectraMax M3 plate reader, exciting the plate at 330 nm and taking two emission readings at 460 nm and 500 nm. The Laurdan generalized polarization (GP) was calculated with the formula: $GP = (I_{460} - I_{500})/(I_{460} + I_{500})$, where I_{460} indicates the fluorescence intensity at 460 nm and I_{500} indicates the fluorescence intensity at 500 nm. All fluidity measurements were performed in biological duplicate.

NPN assay

Ten mL of an OD_{600} of 1 cell suspension of *N. gonorrhoeae* ATCC 49226 was prepared in Graver Wade media. As previously described,[6] the cell suspension was spun at 4,000 rpm, 4°C for 15 minutes, washed twice in 5 mM HEPES buffer (Sigma-Aldrich SRE0065) with 20 mM glucose, and resuspended in an equal volume of the 20 μM NPN (Sigma-Aldrich 104043) in HEPES buffer. A 96-well opaque flat-bottom plate (Costar Black Polystyrene Plate, 266) was prepared with 100 μL of cells in 20 μM NPN in HEPES buffer added to columns 2-12. In column 1, 198 μL of 20 μM NPN in HEPES buffer was added, followed by 2 μL of **NG1** or **NG1 analog** (starting concentration of 128 μg/mL). One hundred μL from column 1 was serially diluted across columns 2-12 to obtain a final total volume of 100 μL in each well. DMSO (1%) treated cells served as the negative control. Plates were then incubated at room temperature for 1 hour with no shaking and the fluorescence at 355/420 nm (excitation/emission) was read using a SpectraMax M3 plate reader with readings taken from the top. All measurements were normalized to corresponding values from the untreated control and performed in biological duplicates.

SYTOX Green assay

Ten mL of an OD_{600} of 0.5 cell suspension of *N. gonorrhoeae* ATCC 49226 was prepared in Graver Wade media. Ninety eight μL of cell suspension was added to a 96-well opaque flat-bottom plate (Costar Black Polystyrene Plate, 266), with 198 μL of cells to column 1. Two μL of **NG1** or **NG1 analog** (starting concentration of 128 μg/mL) was added to column 1 and 100 μL from column 1 was serially diluted across columns 2-12 to obtain a final total volume of 100 μL in each well. One μL of SYTOX Green Nucleic Acid Stain (5mM, S7020, Invitrogen, Carlsbad, CA), a DNA intercalating dye, was then added to each well at a final concentration of 5 μM. DMSO (1%) treated cells served as the negative control, and Triton X-100 served as positive control, resulting in fully compromised membranes. At selected time points (0, 2 and 4 hours post-treatment), fluorescence at 504/523 nm (excitation/emission) was read with a SpectraMax M3 plate reader. All measurements were normalized to the untreated control and performed in biological duplicate.

Proteomics-based target identification with PISA

Sample preparation

Colonies from an overnight plate culture of *N. gonorrhoeae* FA 1090 (ATCC 700825) were resuspended in 650 mL of GC medium (Proteose Peptone No. 3, corn starch, dipotassium phosphate, monopotassium phosphate and sodium chloride; pH adjusted at 7.2 and autoclaved). The medium was supplemented with IsoVitalex 1% v/V final (BD 211876). The bacteria were cultured

Please cite this article in press as: Krishnan et al., A generative deep learning approach to *de novo* antibiotic design, Cell (2025), https://doi.org/10.1016/j.cell.2025.07.033

at 37 °C with 5% CO_2 and grown to an OD_{600} of approximately 0.3. Both bacterial cultures and lysates were treated in four replicates with 10 μM of each antibiotics for 20 min at 37°C.

The protocols for preparing bacterial cultures and lysates were adapted from Modaresi et al.[76] For each condition, 20 mL of bacterial culture was used (4 conditions × 4 replicates × 2 antibiotics). The bacteria cells were washed with 37°C PBS. To prepare the native cell lysate, pelleted bacteria were resuspended in 2 mL lysis buffer (PBS + Halt protease inhibitor) in Eppendorf tubes. The bacteria were subjected to five freeze-thaw cycles in liquid nitrogen to extract proteins. Then the samples were centrifuged at 7000*g* for 5 min at RT to remove debris. The supernatant was then collected and treated with the antibiotic or DMSO for 20 min at 37°C. Each replicate was then aliquoted into 12-wells in a 96-well PCR plate (40 μL per well). The samples were then exposed to a temperature gradient from 46-70°C in the Biometra T-GRADIENT thermocycler for 3 min followed by an additional 3 min at RT and then snap frozen. The 12 samples for each replicate were then pooled into a single tube, transferred to polypropylene ultracentrifuge tubes and centrifuged at 100,000*g* for 20 min at 4°C. The supernatant was collected for proteomics analysis.

Briefly, as previously published,[77–79] 30 μg of each sample was reduced with 10 mM DTT, alkylated with 50 mM IAA in the dark and subjected to methanol chloroform precipitation. Samples were resuspended in 20 mM EPPS buffer, 8 M urea, pH 8.0, and then diluted down to 1.6 M urea and digested with trypsin (1:60 trypsin:protein). Each digest was labeled using TMTpro 16-plex reagents (Thermo Fischer), and the samples were pooled and cleaned using a Sep-Pack C18 column (Waters).

NanoLC-MS/MS analysis

The pooled sample was fractionated off-line by capillary reversed phase chromatography at pH 10 into 12 fractions and dried. NanoLC-MS/MS analyses were performed on an Orbitrap Exploris 480 mass spectrometer (Thermo Fisher Scientific). The instrument was equipped with an EASY ElectroSpray source and connected online to an Ultimate 3000 nanoflow UPLC system. The samples were pre-concentrated and desalted online using a PepMap C18 nano-trap column (length - 2 cm; inner diameter - 75 μm; particle size - 3 μm; pore size - 100 Å; Thermo Fisher Scientific) with a flow rate of 3 μL/min for 5 min. Peptide separation was performed on an EASY-Spray C18 reversed- phase nano-LC column (Acclaim PepMap RSLC; length - 50 cm; inner diameter - 2 μm; particle size - 2 μm; pore size – 100 Å; Thermo Scientific) at 55°C and a flow rate of 300 nL/min. Peptides were separated using a binary solvent system consisting of 0.1% (v/v) FA, 2% (v/v) ACN (solvent A) and 98% ACN (v/v), 0.1% (v/v) FA (solvent B). They were eluted with a gradient of 3–26% B in 97 min, and 26–95% B in 9 min. Subsequently, the analytical column was washed with 95% B for 5 min before re-equilibration with 3% B. The mass spectrometer was operated in a data-dependent acquisition mode. A survey mass spectrum (from *m/z* 375 to 1500) was acquired in the Orbitrap analyzer at a nominal resolution of 120,000. The automatic gain control (AGC) target was set as 100% standard, with the maximum injection time of 50 ms. The most abundant ions in charge states 2^+ to 7^+ were isolated in a 3-second cycle, fragmented using HCD MS/MS with 33% normalized collision energy, and detected in the Orbitrap analyzer at a nominal mass resolution of 50,000. The AGC target for MS/MS was set as 250% standard with a maximum injection time of 120 ms, whereas dynamic exclusion was set to 45 seconds with a 10-ppm mass window.

Data processing

Proteome Discoverer 3.2 software (Thermo Scientific) was utilized for the database search and quantification against the UniProt *N. gonorrhoeae* (UP000000535; 2106 entries) protein database, downloaded on 28 February 2025. Cysteine carbamidomethylation was set as a fixed modification, along with TMT-related modifications, methionine oxidation, deamidation of arginine and asparagine as variable modifications. Enzyme specificity was defined as trypsin with a maximum of two missed cleavages. A 1% false discovery rate was employed as a filter at both the protein and peptide levels. Contaminants were removed, and proteins with missing values were eliminated. The quantified abundance of each protein in each sample (labeled with a different TMT) was normalized to the total intensity of all proteins in that sample. For each protein, the average normalized protein abundance in the antibiotic-treated replicates was divided by the average normalized abundance of that protein in the vehicle-treated replicates. The average ratio across replicates of each compound compared to the vehicle control was calculated, and the Log2 values of these ratios were determined. A two-tailed student's *t*-test was employed to calculate the p-value.

Checkerboard assays

The broth microdilution MICs of **NG1**, ceftriaxone, fosfomycin, CCCP, and PMB were determined to be 0.5, 0.008, 31.25, and 1 μg/mL, respectively, for ATCC 49226. The broth dilution MICs for **NG1** and polymyxin B were found to be 8 and 187.5 μg/mL, respectively, for CDC-FDA ARB #0187. Two-fold serial dilutions of each compound were made to achieve 10× to 0.156× MIC final concentrations. The bacterial inoculum was made with a 1:200 dilution of an *N. gonorrhoeae* OD_{600} 0.08 suspension in Graver Wade media. Each well of a 96-well round-bottom clear plate (Corning 3799) received 98 μL of the bacterial suspension and 1 μL each of two-fold serially diluted compound at 100× final concentration, keeping the final DMSO concentration ≤1%. The plates were incubated overnight at 37°C with 5% CO_2 in a humidity-controlled incubator without shaking. After overnight incubation, OD_{600} was measured and then 10 μL of PrestoBlue™ Cell Viability Reagent (Invitrogen, A13261) was added to each well to obtain quantitative cell viability measurements. Four hours post-incubation at 37°C, fluorescence was read at an excitation/emission of 550/590 nm using a SpectraMax M3 plate reader. MICs were determined as the minimum inhibitory concentration that leads to at least 50% growth inhibition (compared to the untreated control), and the fractional inhibitory concentration index (FICi) for drug combinations was determined. FICi was calculated as follows:

$$FICi = \frac{MIC_{AB}}{MIC_A} + \frac{MIC_{BA}}{MIC_B}$$

Please cite this article in press as: Krishnan et al., A generative deep learning approach to *de novo* antibiotic design, Cell (2025), https://doi.org/10.1016/j.cell.2025.07.033

where MIC_A and MIC_B are the MIC of each antibiotic when administered individually. MIC_{AB} is the MIC of antibiotic A in combination with antibiotic B, and MIC_{BA} is the MIC of antibiotic B in combination with antibiotic A. FICi of <0.5 indicates synergy, values between 0.5-4 indicate indifference, and >4 indicates antagonism.

RNAseq

N. gonorrhoeae FA1090 (ATCC 700825) was grown to mid-log phase in Graver Wade medium (OD_{600} ~0.3). Compounds were added at 4× final MIC, and an equivalent volume of DMSO was added to control cultures. Following treatment, cultures were returned to the incubator and 1 mL aliquots were collected at specified time points: 0, 15, 30, and 60 minutes. Each condition was tested in triplicate. All samples were immediately centrifuged after collection at 15,000 × g for 1 minute to pellet cells. Supernatants were removed and pellets were resuspended in pre-warmed TRIzol reagent (65 °C; ThermoFisher, Cat# 15596026), vortexed, and placed on wet ice for 5 minutes. To all samples, chloroform (Sigma-Aldrich, Cat# C2432) was added, mixed, and centrifuged at 12,000 × *g* for 15 minutes at 4 °C. The aqueous layer was mixed with 100% ethanol, incubated at room temperature for 5 minutes, and the RNA was purified using the Direct-zol RNA Miniprep Plus Kit (Zymo Research, Cat# R2070) according to the manufacturer's protocol. RNA was eluted in 100 μL nuclease-free water following a 5-minute incubation. RNA concentration was measured using a Qubit 4 Fluorometer (ThermoFisher) per manufacturer guidelines.

Library preparation was carried out using the *Illumina® Stranded Total RNA Prep, Ligation with Ribo-Zero Plus* kit with 10 bp unique dual indices. Prepared libraries were sequenced on a NovaSeq X Plus platform (Illumina), generating paired-end 150 bp reads. FASTQ files were generated using Illumina's BCL Convert (v4.2.4). Reads were aligned to the *N. gonorrhoeae* FA1090 reference genome (NCBI: GCF_000006845.1). Gene-level annotations were used to quantify expression levels. Gene read counts were analyzed using the edgeR package in R (verson 4.4.2). Differential expression was calculated using a generalized linear model (GLM) approach. Genes with a false discovery rate (FDR) < 0.05 were considered significantly differentially expressed. KEGG pathway analysis was performed using gene set enrichment analysis in the clusterProfiler R package (v4.10.0).

Bacterial cytological profiling

Bacterial strain and culture conditions

All cytological profiling experiments were performed using *Bacillus subtilis* strain 168 in biological duplicates. Cultures were grown overnight in tryptic soy broth (TSB) at 37°C with shaking at 220 rpm. Overnight cultures were diluted from an OD_{600} of 0.7 into fresh TSB and seeded into poly-D-lysine–coated black-wall, clear-bottom 96-well plates (Millipore Sigma, CLS3842) for imaging.

Drug treatment and fixation

Cells were incubated at 37°C with orbital shaking (50 rpm) for 30 minutes post-seeding before treatment with either vehicle control or antibiotics. Drug exposure was carried out for 1.5 hours. Following treatment, cells were fixed with 4% paraformaldehyde (PFA) in phosphate-buffered saline (PBS) for 15 minutes at room temperature and washed twice with PBS prior to staining.

Staining and imaging

Fixed cells were stained using FM4-64 (membrane; Thermo Fisher, T13320) and DAPI (nuclei; Thermo Fisher, D1306) according to the manufacturer's instructions. Imaging was performed using an Opera Phenix 2 high-content confocal microscope (PerkinElmer) equipped with a 63× water-immersion objective. Confocal z-stacks were acquired with five planes spaced 1 μm apart. Brightfield images were acquired in parallel.

Image analysis and feature extraction

Raw images were processed using Harmony (PerkinElmer) and Signal Image Artist. Bacterial segmentation and morphometric feature extraction were performed using Omnipose. Objects were filtered to remove background and artifacts using built-in heuristics, and single cell areas (in μm^2) were extracted. Feature distributions were aggregated across fields of view and exported for downstream analysis. Summary statistics were computed using custom Python scripts. Group comparisons were evaluated using nonparametric Mann-Whitney U tests.

Cryo-TEM analysis of bacterial morphology

Sampling

Neisseria gonorrhoeae (ATCC 49226) and *Staphylococcus aureus* (RN4220) was grown overnight in stationary cultures. Cells were harvested by transferring the culture to a 5 mL tube and centrifuging at 2000 rpm for 1 minutes. The supernatant was discarded, and the cell pellets were washed twice by resuspending in 3 mL of phosphate-buffered saline (PBS; Sigma-Aldrich) and centrifuging under the same conditions. After the final wash, the cells were resuspended in 99 μL of LB and 1 μL of the drug (**NG1** or **DN1** at 4× MIC). The samples were incubated at 37°C for 2 hours. The final cell suspension was centrifuged again, adjusted to an optical density at 600 nm (OD_{600}) of 0.3 and fixed in 2.5% glutaraldehyde at 4 °C for 1 hour. Following fixation, the cells were washed three times with deionized water. 3 μL of the cell suspension was applied to glow-discharged carbon-coated grids. The grids were vitrified in liquid ethane using a Gatan Cryoplunge system and the imaging was carried out using a JEOL 2100F transmission electron microscope.

Image processing and segmentation

Raw cryo-TEM images of *S. aureus* and *N. gonorrhoeae* were manually segmented to delineate the cell boundary and, when visible, the cytosolic region. Segmented binary masks of cryo-TEM images were analyzed using a custom Python pipeline built with OpenCV, scikit-image, and SciPy. For each object, region properties including area, perimeter, major and minor axis lengths were extracted. Elongation was defined as the ratio of major to minor axis length, and roundness as its inverse. Objects with an area less than 50 pixels were excluded. Image-specific scale factors (μm/pixel), retrieved from a CSV calibration file, were applied to convert all measurements to physical units. When inner membrane masks were available, membrane thickness was estimated by computing the Euclidean distance transform between outer and inner membrane masks. The average distance was doubled to approximate membrane thickness.

Per-cell measurements were aggregated across images and saved as.csv files. Summary statistics (mean ± standard deviation) were computed for each group. Group comparisons (e.g., **DN1**-treated vs. untreated) were evaluated using two-sided Mann-Whitney U tests (ranksum), appropriate for non-normally distributed data.

Toxicity studies

Hemolysis and modified Ames genotoxicity studies were performed as described previously.[7] To test the systemic toxicity of **DN1**, healthy female C57BL/6J mice were given a single 100 mg/kg dose of **DN1**, which three out of three mice tolerated. An additional three mice were given four doses of 50 mg/kg every 6 hours, which they all also tolerated. To test the systemic toxicity of **NG1**, healthy female BALB/c mice were given increasing doses of **NG1**, up to 100 mg/kg. Both compounds were formulated in a 10% compound in DMSO:45% PEG300:45% water solution and administered as a 200 μL intraperitoneal injection. Mice were observed for at least 24 hours for typical signs of toxicity, including impaired movement, lethality, and irritation. Results were representative of at least three mice per dose of each compound.

Mouse S. aureus *topical wound infection model*

Female C57BL/6J mice were given over a week to acclimate and then rendered neutropenic with cyclophosphamide (Cytoxan) on Day -4 (150 mg/kg, I.P.) and Day -1 (100 mg/kg I.P.). On Day 0, a fresh suspension of *S. aureus* BAA1556 was prepared in tryptic soy broth and titered via serial dilution and plating. Mice were given buprenorphine for anesthesia and kept sedated under isoflurane vapors (3%) during the infection procedure. A ~1.5 cm^2 patch of skin was prepared on each mouse's dorsal surface by shaving the fur, sterilizing the underlying skin with iodine and ethanol swabs thrice, allowing the skin to dry completely, and abrading the skin until visibly damaged (reddening and glistening) but not bleeding. Five μL of the *S. aureus* suspension, corresponding to an inoculum of 1.5×10^5 CFU, was pipetted onto the skin to initiate the bacterial infection. Treatments were administered at 1, 4, 8, 16, 21, and 24 hours post-infection by pipetting 40 μL of formulation topically onto the infected skin and allowing to dry. Treatments groups consisted of *n* = 6 mice receiving **DN1** (1% final concentration, prepared as described above), *n* = 6 mice receiving vehicle control (DMSO:PEG300:water at 10%:45%:45%), and *n* = 6 mice receiving the fusidic acid positive control (0.25% final concentration in DMSO:PEG300:water at 10%:45%:45%) At 25 hours post-infection (~1 hour following the last topical treatment), all mice were euthanized by CO_2 asphyxiation, and wounds were wiped with an alcohol pad, excised, weighed, and homogenized in 2 mL of sterile PBS using a Polytron PT10-35 with a 12 mm aggregate that was cleaned with ethanol and water between samples. Homogenized wounds were serially diluted and plated onto BHI agar to determine bacterial titers (CFU/g tissue).

Mouse N. gonorrhoeae *vaginal infection model*

Female ovariectomized BALB/cJ mice were given over a week to acclimate prior to handling. As described previously,[80] two days prior to infection (Day -2), vaginal lavage was performed for estrous staging and monitoring of the vaginal microbiota via culture on MacConkey and Brain Heart Infusion agar plates. To increase susceptibility to infection, each mouse received a dose of 17B-estradiol (0.23 mg, I.P.) on Day -2 and Day 0. To reduce the overgrowth of commensal bacteria that occurs with estradiol treatment, mice were given streptomycin (1.2 mg, I.P.) and vancomycin (0.6 mg, I.P.) (1 dose on Day -2, two doses at least 5 hours apart on Day -1, and one dose Day 0) as well as trimethoprim (0.4 g/L) in the drinking water (refreshed on Day 0). On Day 0, the inoculum was prepared by collecting isolated colonies of *N. gonorrhoeae* ATCC 49226 from an overnight chocolate agar plate in sterile PBS to achieve an OD_{600} 0.2. Within one hour of preparation, the vagina was first rinsed with 30 μL of 50 mM HEPES (pH 7.4) and then 20 μL of the bacterial suspension (~3×10^6 CFU per mouse) was pipetted intravaginally while the mouse was held by the tail with paws grasping the wire cage for at least 1 minute. Serial dilutions of the bacterial suspension were plated onto chocolate agar to determine the initial inoculum. Treatments were administered at 2, 6, 10, 18, and 24 hours after infection by pipetting 20 μL of test compound **NG1** (1% final concentration in 10% DMSO, 45% PEG300, 45% water), ceftriaxone (0.1% w/v in water), or vehicle control (10% DMSO, 45% PEG300, 45% water) intravaginally; mice were suspended by the tail for 1 minute before being released into the cage. At 24 hours after infection, mice were euthanized by CO_2 asphyxiation and vaginal lavage was performed using 50 μL of Graver Wade media with 0.05% saponin. *N. gonorrhoeae* burden was determined by plating 30 μL of neat lavage and 10-fold serial dilutions in PBS onto Thayer Martin Agar Improved (Thermo Fisher); colonies were counted after 18-24 hours of incubation at 37°C with 5% CO_2.

QUANTIFICATION AND STATISTICAL ANALYSIS

All statistical analyses were performed using Python scripts and/or GraphPad Prism (version 10.1.0). Details of the statistical tests used, the exact value of *n*, what *n* represents, as well as measures of central tendency (mean or median) and dispersion (e.g.,

Please cite this article in press as: Krishnan et al., A generative deep learning approach to *de novo* antibiotic design, Cell (2025), https://doi.org/10.1016/j.cell.2025.07.033

standard deviation) are provided in the figure legends and STAR Methods section. For each analysis, the choice of statistical test (e.g., student's *t*-test or non-parametric tests, such as the Mann-Whitney U or Kolmogorov-Smirnov test) was based on the data type and experimental design. For mouse experiments, sample sizes were determined by power calculations in GraphPad Prism to detect a 1-2 log-fold change in effect size and mouse availability. Group allocation was determined by cage, where each cage contained 3-5 mice that all received the same treatment. No data were excluded from the analyses in the study. The data were assumed to be non-normal; thus, a two-sided Mann-Whitney test was performed using GraphPad Prism. Statistical details can be found in the figure legends.

Supplemental figures

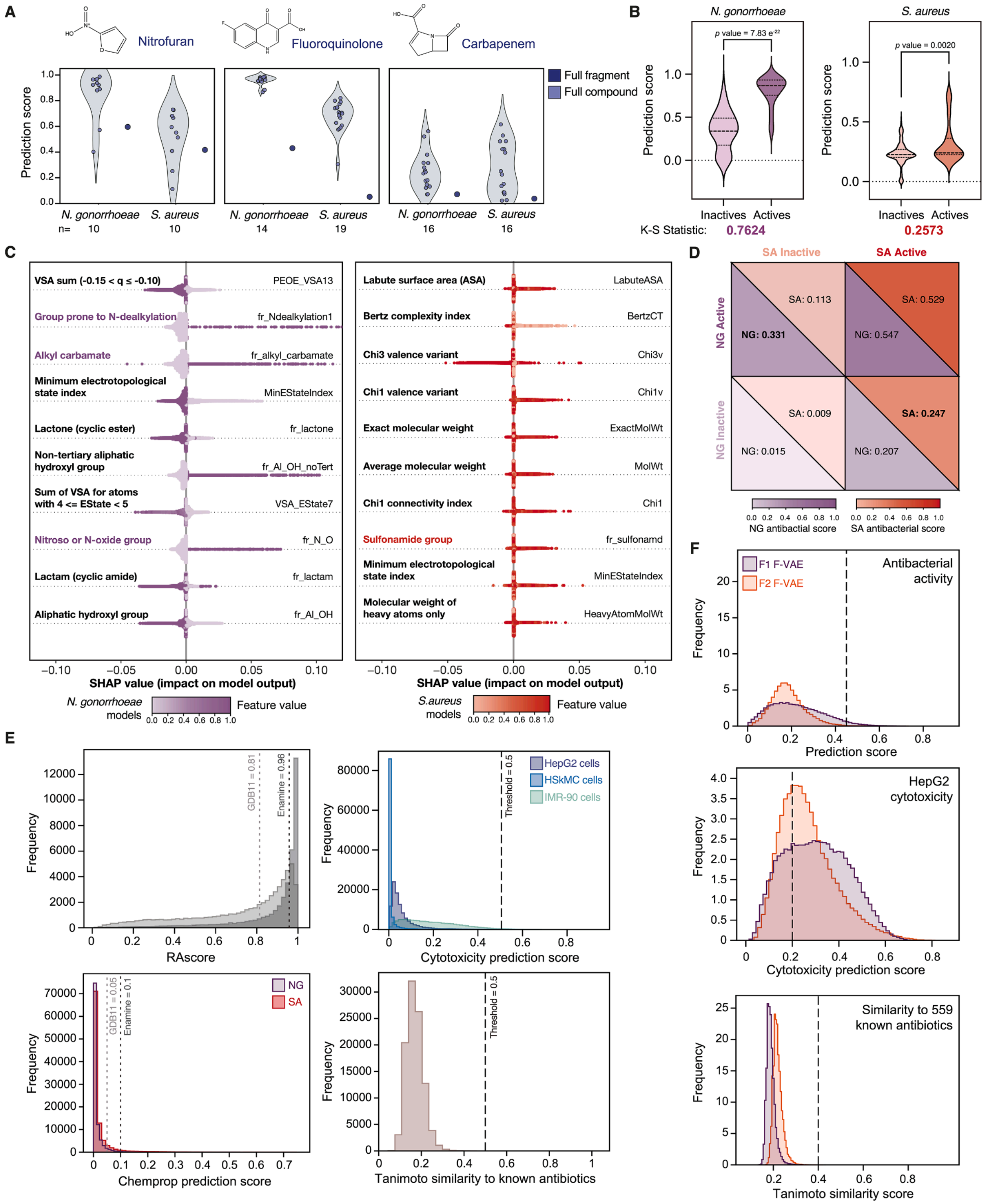

(legend on next page)

Figure S1. Computational analyses of the predictive capabilities of Chemprop models, related to Figure 1

(A) Known fragments (pictured above) were scored and compared with known antibiotics containing these fragments (*n*, number of antibiotics scored). Scores were generated by separate *N. gonorrhoeae* and *S. aureus* growth inhibitory activity-predicting ensembles of Chemprop models.

(B) Kolmogorov-Smirnov (K-S) statistic showing the predictive capabilities of the Chemprop models for both *N. gonorrhoeae* and *S. aureus*. It is a non-parametric test and quantifies the maximum distance between their cumulative distribution functions, capturing where the two distributions (“active” and “inactive” predictions) diverge the most. K-S statistic of 0 indicates perfect agreement, while values closer to 1 reflect greater divergence. Smaller *p* values (typically below 0.05) suggest that the data are likely coming from different distributions.

(C) Shapley additive explanations (SHAP) analysis to assess feature importance from both *N. gonorrhoeae* and *S. aureus* Chemprop models. Shown are the top 10 features that modestly contribute to the models’ performance.

(D) Species specificity of the *N. gonorrhoeae* and *S. aureus* models by comparing the mean predicted scores generated by each model for compounds that were empirically tested against both bacterial species.

(E) Histograms showing the different thresholds used for the down selection of the fragments: RAscore, antibacterial prediction scores by *N. gonorrhoeae* and *S. aureus* Chemprop models, cytotoxicity prediction scores against hepatocellular carcinoma (HepG2), human skeletal muscle cells (HSkMCs), and human lung fibroblasts (IMR-90), and Tanimoto similarity to known antibiotics.

(F) Histograms showing the different thresholds used for the down selection of fragment-based (F1 and F2) generated compounds: antibacterial prediction scores by *N. gonorrhoeae* and *S. aureus* Chemprop models, cytotoxicity prediction scores against hepatocellular carcinoma (HepG2), and Tanimoto similarity to known antibiotics.

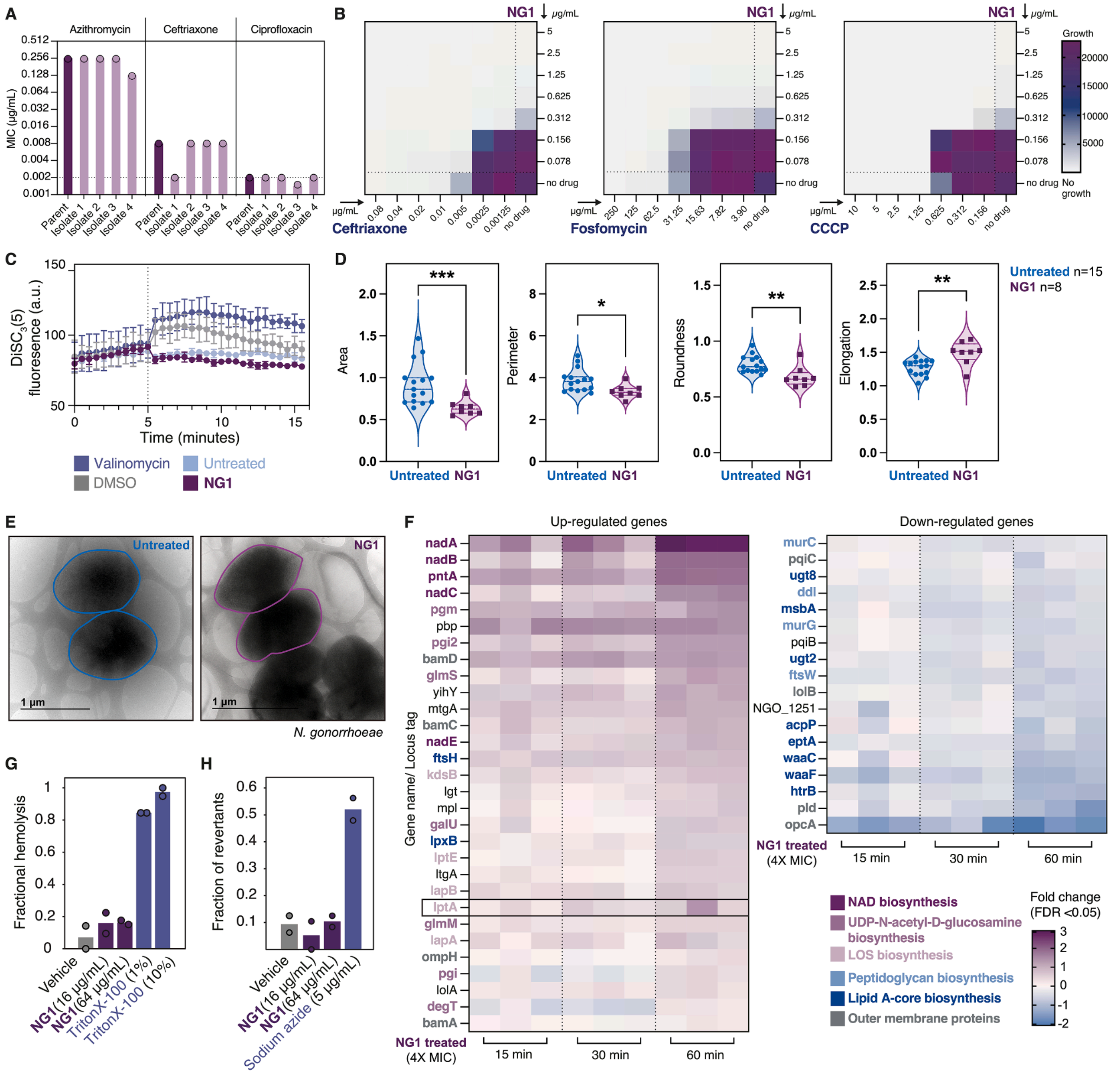

Figure S2. Mechanistic insights and toxicological properties of NG1, related to Figures 2 and 3

(A) MICs of **NG1**-resistant isolates from spontaneous generation experiments to known antibiotics: azithromycin, ceftriaxone, and ciprofloxacin.

(B) Checkerboard assays to assess synergistic or antagonistic effects of **NG1** with cell-wall-targeting antibiotics (ceftriaxone and fosfomycin) and a membrane PMF-targeting compound (CCCP), indicating indifference to each combination.

(C) DiSC$_3$(5) traces of *N. gonorrhoeae* cells treated with **NG1**, indicating a lack of effect on either component of the PMF. Results are representative of two biological replicates.

(D) Quantification of morphological changes observed in the area, perimeter, roundness, and elongation of **NG1**-treated *N. gonorrhoeae* from cryo-TEM images.

(E) Representative image of an elongated cell (treated with **NG1**) compared with the wild-type untreated condition.

(F) Gene expression analysis showing LOS biosynthesis-related genes that are significantly differentially expressed in **NG1**-treated conditions relative to the untreated control.

(G) Fractional hemolysis measurements of human red blood cells (RBCs) treated with **NG1** at the indicated final concentrations. Vehicle (1% DMSO) was used as a negative control, and Triton X-100, a detergent, was used as a positive control. Points represent values from two biological replicates.

(H) Ames mutagenesis test measurements of the fractions of revertant *S. typhimurium* TA100 cultures treated with **NG1** at the indicated final concentrations. Vehicle (1% DMSO) was used as a negative control, and 5 µg/mL sodium azide was used as a positive control. Points represent values from two biological replicates.

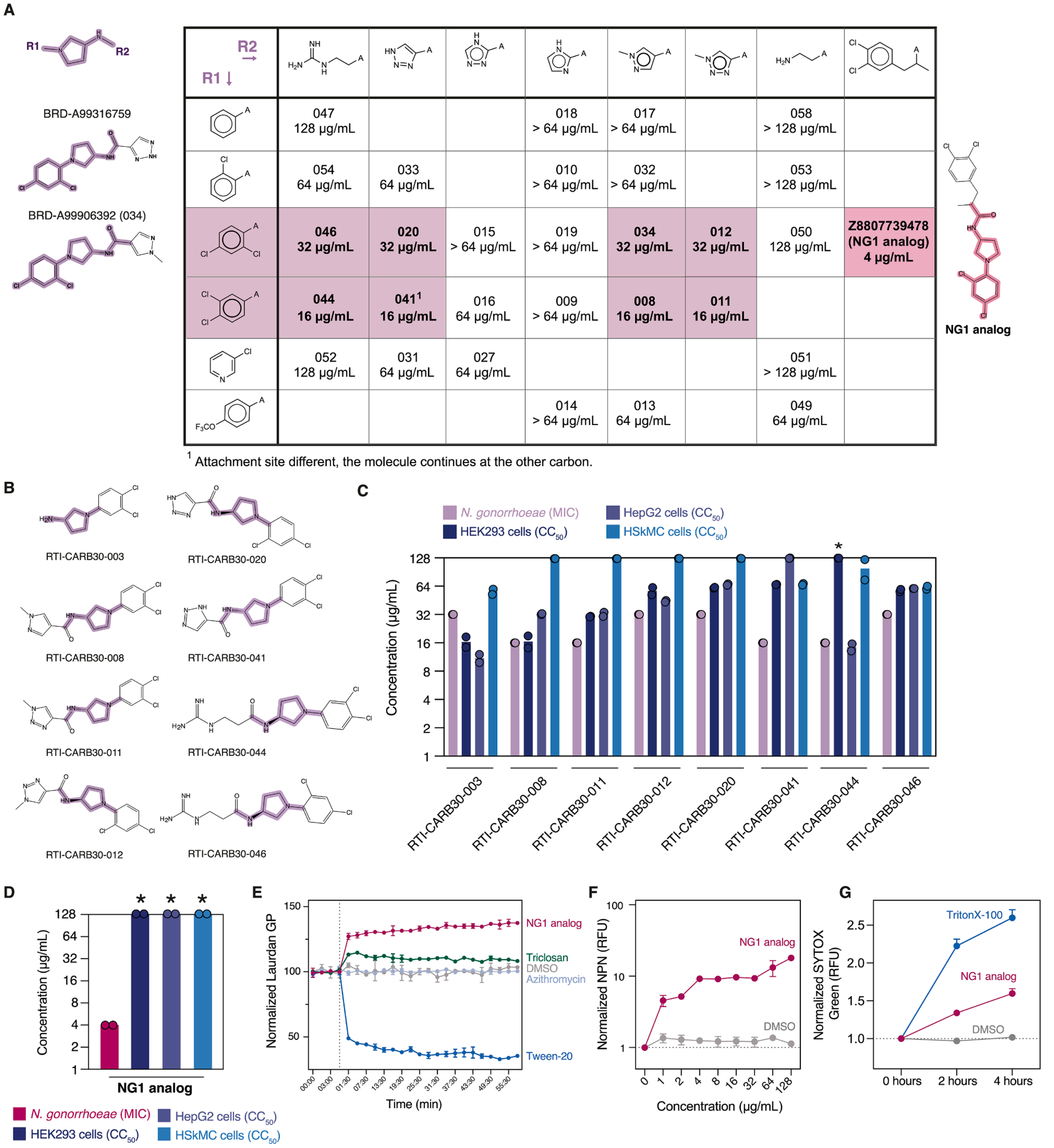

R2 → / R1 ↓								
	047 128 µg/mL			018 > 64 µg/mL	017 > 64 µg/mL		058 > 128 µg/mL	
	054 64 µg/mL	033 64 µg/mL		010 > 64 µg/mL	032 > 64 µg/mL		053 > 128 µg/mL	
	046 **32 µg/mL**	**020** **32 µg/mL**	015 > 64 µg/mL	019 > 64 µg/mL	**034** **32 µg/mL**	**012** **32 µg/mL**	050 128 µg/mL	**Z8807739478** **(NG1 analog)** **4 µg/mL**
	044 **16 µg/mL**	**041**[1] **16 µg/mL**	016 64 µg/mL	009 > 64 µg/mL	**008** **16 µg/mL**	**011** **16 µg/mL**		
	052 128 µg/mL	031 64 µg/mL	027 64 µg/mL				051 > 128 µg/mL	
				014 > 64 µg/mL	013 64 µg/mL		049 64 µg/mL	

[1] Attachment site different, the molecule continues at the other carbon.

Figure S3. Designed and tested analogs of NG1 and mechanistic characterization of NG1 analog, related to Figure 3

(A) Hits from 74 analogs of fragment F1 tested with modifications in functional groups R1 and R2.

(B) Structures of the eight active analogs with MIC $\leq$ 32 µg/mL. All other analogs were inactive with MICs > 64 µg/mL.

(C) MIC and CC_{50} values of human cells treated with the active analogs.

(D) MIC and CC_{50} values of **NG1 analog**, the most potent active analog of **NG1**. Points represent two biological replicates.

(E) Membrane rigidification of *N. gonorrhoeae* cells treated with **NG1 analog** (at 64 µg/mL) and Tween 20 (membrane fluidizer) with the Laurdan membrane fluidity assay. Shown is the generalized polarization (GP) observed in two biological replicates.

(legend continued on next page)

(F) Loss of membrane integrity of *N. gonorrhoeae* cells treated with **NG1 analog** (at 64 μg/mL), as measured by the uptake of the hydrophobic fluorescent probe, 1-N-phenylnaphthylamine (NPN). Shown is the fluorescence measurement, normalized to the untreated control, observed in two biological replicates.

(G) Lysis of *N. gonorrhoeae* cells treated with **NG1 analog** or Triton X-100 (positive control), as seen by an increase in SYTOX green fluorescence signal with time, measured at 0, 2, and 4 h post-treatment. Data represent the fluorescence, normalized to the untreated control, observed in two biological replicates.

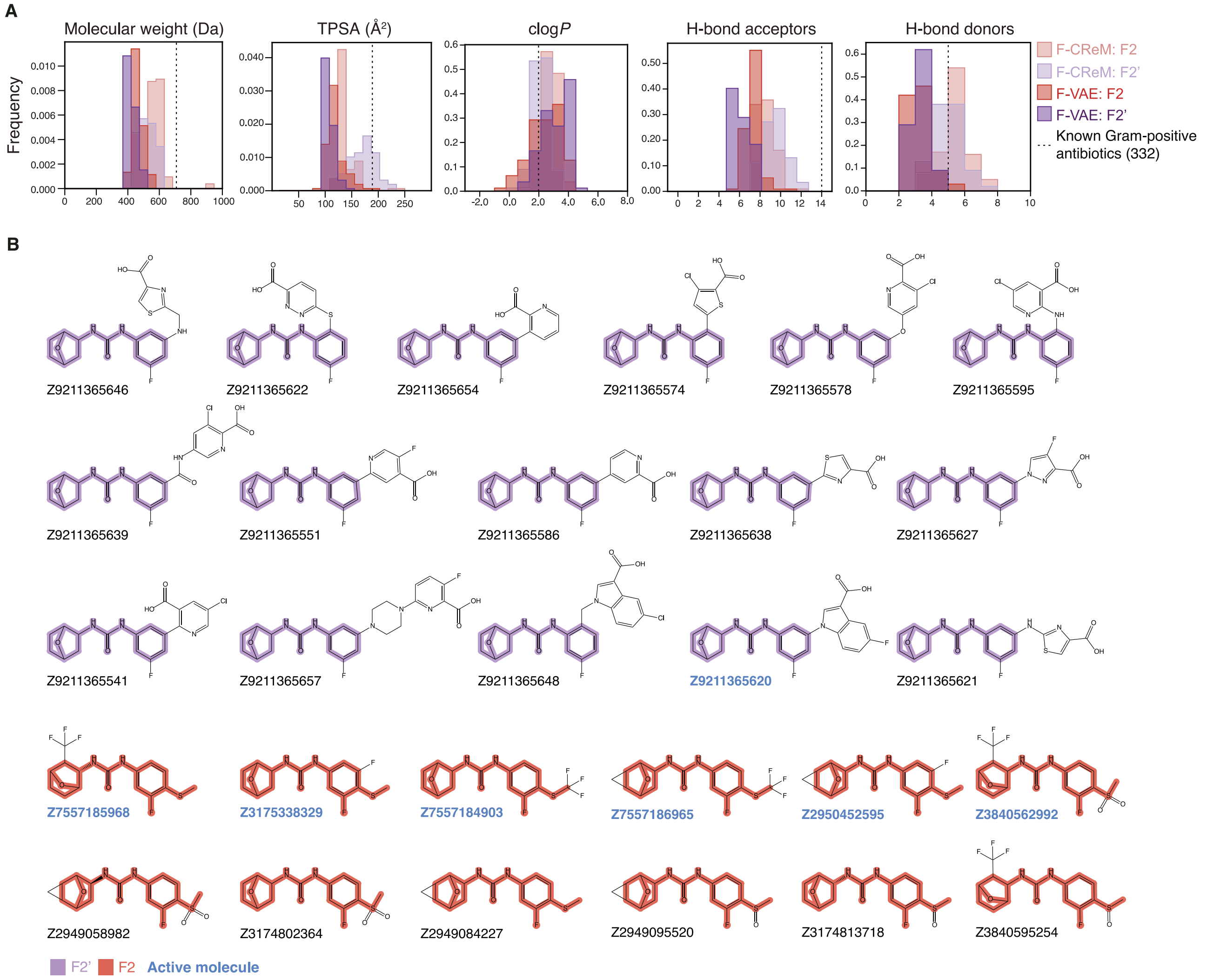

Figure S4. Structures and properties of molecules related to EN1, related to Figure 4

(A) Physiochemical properties of F2 and F2′ molecules generated by F-CReM and F-VAE.

(B) Structures of all tested compounds containing F2 and F2′. Active molecules with MIC ≤ 128 μg/mL are highlighted in blue, indicating that preservation of the fragment is important for antibacterial activity.

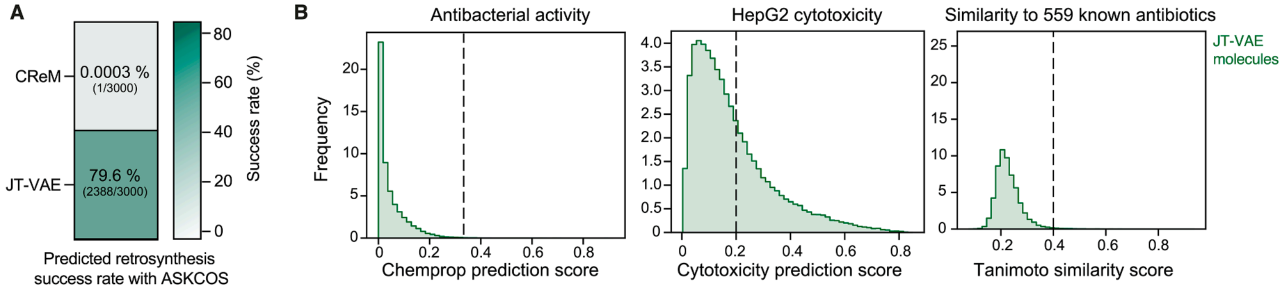

Figure S5. Thresholds used to down-select JT-VAE molecules and their predicted synthesizability via ASKCOS, related to Figure 5

(A) Predicted retrosynthesis success rate as determined by ASKCOS for *de novo* molecules generated by both CReM and JT-VAE.

(B) Histograms showing the different thresholds used for the down selection of *de novo*-generated compounds by JT-VAE: antibacterial prediction scores by *N. gonorrhoeae* and *S. aureus* Chemprop models, cytotoxicity prediction scores against hepatocellular carcinoma (HepG2), and Tanimoto similarity to known antibiotics.

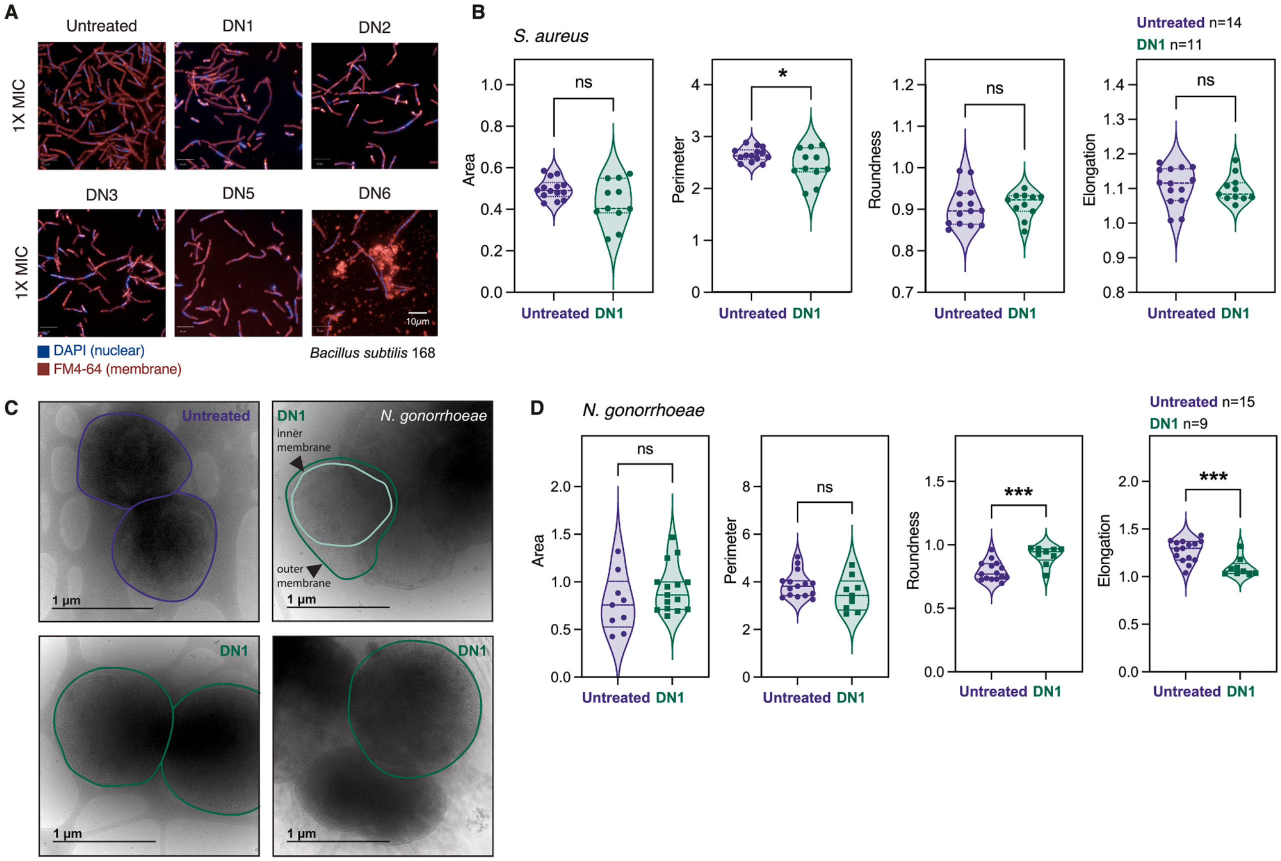

Figure S6. Bacterial morphological changes induced by DN1–DN6 treatment, related to Figure 6

(A) Morphological changes observed in *B. subtilis* 168 treated for 2 h with **DN1–DN6** entirely *de novo* molecules at 1× MIC.

(B) Quantification of different parameters from cryo-TEM images of *S. aureus* RN4220 untreated or treated with **DN1**. "*n*" indicates the number of cells used for the quantification, and comparisons were evaluated using a two-sided Mann-Whitney U test. Each data point represents a single cell. Related to Figure 6G.

(C) Representative cryo-TEM images of *N. gonorrhoeae* ATCC 49226 untreated or treated with **DN1**, showing membrane dislodgement and swelling of the cells.

(D) Quantification of the different parameters based on several cryo-TEM images of *N. gonorrhoeae* ATCC 49226 untreated or treated with **DN1**. "*n*" indicates the number of cells used for the quantification, and comparisons were evaluated using a two-sided Mann-Whitney U test. Each data point represents a single cell.

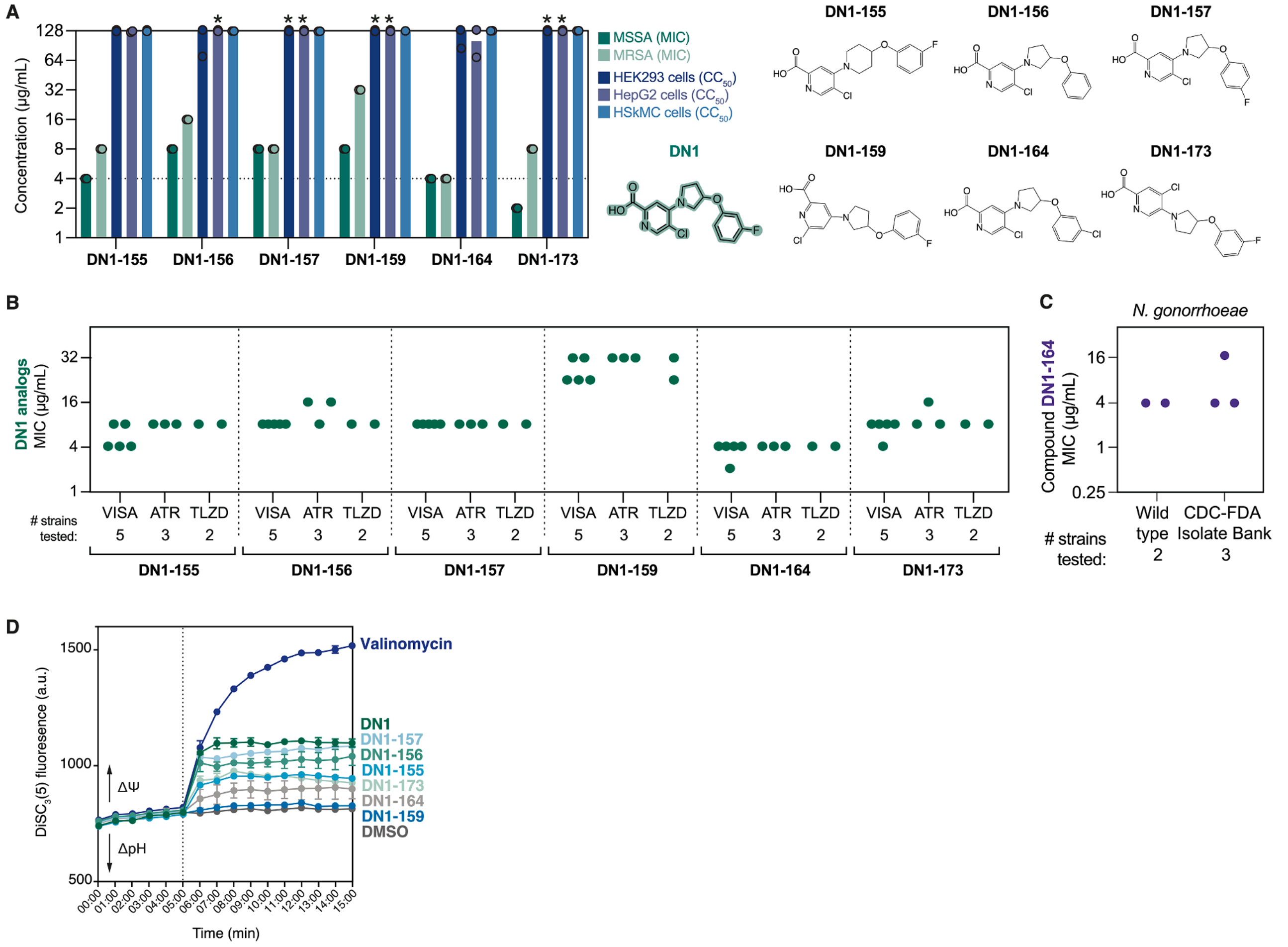

Figure S7. Designed and tested analogs of DN1 and their mechanistic characterization, related to Figure 7

(A) Six active analogs of **DN1** with MICs ≤ 32 µg/mL. MIC and CC_{50} values of the compounds tested against MSSA RN4220 and three different human cell lines are shown, along with their chemical structures. Details of all analogs tested are in Data S2.

(B) MICs of the **DN1 analogs** against drug-resistant *S. aureus* isolates with vancomycin-intermediate (VISA) resistance, aminoglycoside/tetracycline resistance (ATR), and tedizolid/linezolid (oxazolidinone) resistance (TLZD) from the CDC-FDA ARB.

(C) MIC of **DN1–164** against antibiotic-resistant strains of *N. gonorrhoeae*.

(D) $DiSC_3(5)$ of *S. aureus* cells treated with **DN1 analogs**. Results are representative of two biological replicates.